UCLouvain

École polytechnique de Louvain

Synthetic Aperture Radar at Small Scale

Design of a short range synthetic aperture radar system for imaging

Authors: **Adrien Delhaye, Marie-Pierre van Oldeneel**
Supervisors: **Laurent Jacques, Luc Vandendorpe**
Reader: **Christophe Craeye**
Academic year 2018–2019
Master [120] in Electrical Engineering & Master [120] in Electro-mechanical Engineering

Acknowledgments

First of all, we would like to master thesis supervisors, Prof. Laurent Jacques and Prof. Luc Vandendorpe. All along the year, they were available and offered us relevant advises and suggestions to bring this master thesis further.

We would also like to thank Mr Pascal Simon that provided the equipment to perform our experiments, as well as an access to the *Welcom Lab*.

Finally, we would like to emphasise the support that Thomas Feuillen provided to our work. He was always interested in the progression of the master thesis and motivated to provide new ideas of setups and environments to measure. He was also the person which found the radar we used for our experiments. This accomplishment would not have been possible without him and therefore, we would to thank him.

Abstract

Radar systems have proven to be more adapted than cameras systems for many applications. Their main advantage is that they do not suffer of atmospheric conditions such as brightness, weather and others. However, classical radar systems are limited in resolution. To overcome this shortcoming, Synthetic Aperture Radars (SARs) have been developed. This widely spread imaging technique consists in moving a radar on a platform. By using the radar displacement, the resolution of the recovered image can be enhanced with regards to classical radar systems.

Most SAR systems are used at large scale to perform cartography, echo-location and others. In this master thesis we develop and validate a model and a physical system to perform SAR imaging at small scale using Frequency Modulated Continuous Waves (FMCW).

We first develop a mathematical model to describe the problem, starting from the expression of the emitted FMCW signal and the Fraunhofer assumption. We then extract the required constraints and limits of this model, in order to design the small scale SAR system in practice. Finally, we empirically validate the model based on different measurements that we have deeply analysed.

This master thesis offers a robust model and relevant associated experiments in order to provide a complete toolbox to perform SAR at small scale.

Contents

Chapter 1

Introduction

For many applications, radar imaging has proven to be more adapted than classical camera imaging. Radar systems have long been used for military and non military purposes in a wide variety of applications such as imaging, remote sensing and global positioning, but their original function, "echo-location", remains the principal application of modern radar systems. The main advantage of radar systems is that radars do not suffer of atmospheric conditions as much as classical systems as cameras. That is, they do not require brightness to operate at long range and they are thus able to operate in all weather conditions, day or night, as long their wavelengths pass through clouds, smoke, sand and others. Radar systems detect and track moving objects with high achievable imaging resolution.

Classical radar systems use antennas to create a beam illuminating the scene of interest. Then they use the delay between the emitted and received signals to recover information from the targets. Those systems, denoted Real Aperture Radar (RAR), are efficient but limited in resolution. Since 1951 [1], a technique called Synthetic Aperture Radar (SAR) has been developed to enhance radar imaging resolution. The main idea is to synthesise an array of antennas using only one antenna, moving along an axis. The image can thus be recovered from the phase differences of signals received by the antenna at different locations. The main advantage of this technique is that, contrarily to RAR systems, their resolution is not fixed by the physical length of the antenna, but by the antenna path length. [2] Multiple improvements have been made since the first SAR system such as the use of frequency modulated signals [3] or the consideration of the Doppler effect [4]. Those improvements led to higher resolution in SAR imaging.

Most SAR systems are used for military or spatial applications and are thus used at large scales to perform cartography, *echo-location* and others. Such kinds of systems are expensive, hard to manage and to access for the common user.

In this master thesis, we develop a model for small scale SAR processing. The main idea is to provide tools to describe, design and experiment a *cheap* SAR system that

could be used for more common applications. In today's world, technologies like drones, robots or 3D-printers are becoming more and more accessible to companies and individuals at work or at home. Today nearly everyone can buy or build a drone by themselves, without depending on a teacher or on an organisation. In this context, we want to facilitate the access to radar technologies as it could be used as an additional sensor on existing machines or even be used improve the imaging capabilities of drones.
The contributions of this master thesis can be described in the following points:

- Developing a model for *small range SAR imaging* and quantifying its range of validity.
- Extracting the sizing constraints and limits of the developed model and the available technology, while highlighting the impact of this technology on the possible applications.
- Describing, simulating and comparing the two main algorithms that we will use to process our SAR data.
- Performing measurements in order to test the limits of the developed model and to discuss its validity.

To do so, we first briefly describe the existing models and techniques for SAR imaging. Second, we present the Far Field assumption from Fraunhofer as it will be our *starting point* to develop the model. Third we present and simulate both algorithms that we will use to process SAR data obtained with our model : the *Fourier Transform* algorithm and the *Matching Pursuit* algorithm. Fourth we present the sizing process that we have developed to design the physical system and setups used to perform measurements. Finally, we present and discuss the relevant results that we have obtained from our experiments.

Chapter 2

State of the art

Radars are radio waves based sensors used to determine the range, angle or velocity of targets. The name of those sensors is an acronym for Radio Detecting And Ranging, that describes their main function : echo-location. In fact, most of radars are used to detect targets and measure their distances from the device. Radars systems are also widely used with satellites and airplanes to produce maps and pictures of landscapes.
In this section, we present the basis of the functioning of those sensors and overview the existing techniques to enhance their precision. In addition to this, a description of antenna arrays is provided.

2.1 Electromagnetic waves

An electromagnetic wave is characterised by an amplitude, a wavelength, a frequency and a velocity. Radio waves are travelling at the speed of light ($c \simeq 3 \cdot 10^8$) in free space. When an electromagnetic wave reaches a target, a part of the energy is absorbed and the other part is reflected as a new wave with different characteristics (amplitude, phase and polarisation). In addition to the signal echoed from the target, the returned wave also contains noise.
The capability of an object to reflect an incident EM wave in direction to the antenna of the receiver described by its *radar cross-section.* This is a characteristic of a particular target that measure its section as seen by the radar. [5]
In this master thesis we will only focus on the power reflected aspect and not on the change in polarisation that the reflected wave can have.

2.2 Radar systems

Radar systems are divided into two main configuration types : Synthetic Aperture Radars (SAR) and Inverse Synthetic Aperture Radars (ISAR). Each configuration can be used either continuous wave (CW) mode or in pulsed mode. [1]
As presented in Figure 2.1, radar systems are usually composed of a transmitter, that amplifies a modulated electromagnetic wave of a particular waveform, and a receiver, that detects the signal returned from the target. The returned signal has first to be amplified, down-converted and processed before useful information can be extracted from it. [5] The received wave is a delayed and attenuated version of the transmitted wave. By measuring the delay, the distance between the target and the radar (range distance) can be recovered.

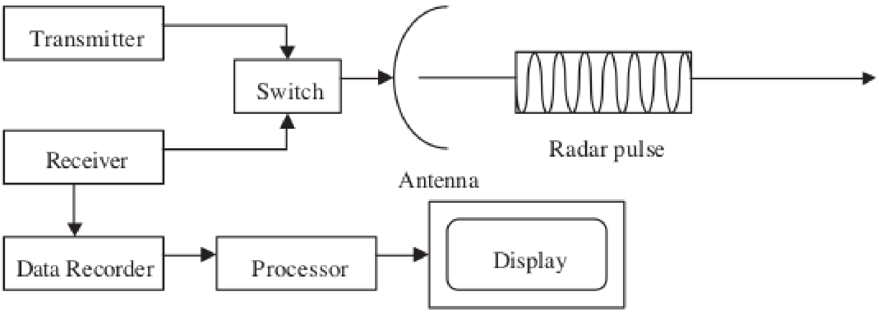

Figure 2.1: Block diagram for a typical pulsed radar system, from [6]

2.2.1 Detection and ranging

The basic idea of echo-location can be detailed by considering an ideal radar system that emits, at time $t = 0$, a short pulse that travels at the speed of light in free space c. This wave will reflect from an object at a range distance R and returns to the radar. In an ideal environment, the pulse returned to the radar will be detected with a time delay τ. As the speed of the wave c is known and its delay τ is measured, we can recover the range distance between the radar and the target with relation 2.1.

$$R = \frac{c\tau}{2}, \tag{2.1}$$

where the division by two is due to the fact that the waves come back to the radar and thus, travels twice the range distance R. [1]

2.2.2 Radar equation

In order to properly perform radar detection or imaging, a fundamental consideration for the quality of the result is the Signal to Noise Ration (SNR). As a reminder, SNR compares power of a signal with the power of the background noise. In radar applications, the equation that evaluates the SNR with respect to additive thermal noise is commonly called the *Radar Equation.* [7] This equation relates the achievable range of the radar (R) to the characteristics of its system such as the transmitter, the receiver, the antenna, the target or the environment.
To obtain the radar equation, we first develop the expression of the power of a signal transmitted from one antenna to another, following the signal path and considering every loss factor that has to be applied on the initial power. Then we will compute the SNR by dividing this power by the noise power. This way, we will obtain the expression of the SNR for a general radar system.
The development, notations and parameter descriptions have been inspired from [7], [8] and [9].

Directive transmit antenna - $\mathbf{T_X}$ We assume that a power P_t is delivered to a directive antenna. If this antenna is *lossless* and *isotropic* (it radiates power uniformly in all directions), the radiated power density at a distance R from the transmit antenna can be expressed as

$$P_{A,iso} = \frac{P_t}{4\pi R^2}. \tag{2.2}$$

In fact, the power P_t is uniformly distributed over the surface area of a sphere of radius R. However, in most radar applications, it is wasteful to radiate energy in all directions. We thus prefer using *directive antennas* to radiate the power in a particular direction. The radiated power density is thus increased by a factor G_A that represents the antenna gain. [8] We have

$$P_{A,dir} = P_{A,iso} \cdot G_A = \frac{P_t G_A}{4\pi R^2} \tag{2.3}$$

for a directive antenna fed with a power P_t.

Radar cross-section of the target (RCS) Once the power has been radiated in a specific direction by the transmit antenna, the target that we suppose to be located at a distance R from the antenna intercepts a portion of the power and reflects it in various directions. [8] The amount of power intercepted by the target is characterised by its *Radar Cross-Section (RCS).* It is denoted σ and is specific to each target. RCS can be interpreted as the size of the target from the radar point of view or the target size seen by the radar. The power intercepted by the target expressed in terms of the power supplied to the transmit antenna can thus be written as

$$P_{\text{target}} = P_{A,dir} \cdot \sigma = \frac{P_t G_A \sigma}{4\pi R^2}, \tag{2.4}$$

where σ is the RCS of the target expressed in $[m^2]$.
In addition to the amount of power intercepted by the target, we have to consider that it is not directive. In fact, we assume the target to be isotropic and the power reflected by the target is spread in all directions, giving

$$P^r_{\text{target}} = \frac{P_{\text{target}}}{4\pi R^2} = \frac{P_t G_A \sigma}{(4\pi R^2)^2}. \tag{2.5}$$

Receiving antenna - $\mathbf{R_X}$ As presented above, a power P^r_{target} comes back to the receiving antenna. The fraction of this power that will be intercepted by the receiving antenna depends on its *effective area* or *effective aperture*. It is denoted A_e and is expressed in $[m^2]$. We have

$$\hat{P}_r = P^r_{\text{target}} \cdot A_e = \frac{P_t G_A \sigma A_e}{(4\pi R^2)^2}. \tag{2.6}$$

Atmospheric and radar losses Finally, we have to consider losses due to the propagating wave in the atmosphere L_{atmos} and due to the radar L_{radar}. Those factors are adimensional. [7] We can thus write the complete expression of the power received back to the radar antenna :

$$P_r = \hat{P}_r \cdot \frac{1}{L_{\text{atmos}} L_{\text{radar}}} = \frac{P_t G_A A_e \sigma}{(4\pi)^2 R^4 L_{\text{atmos}} L_{\text{radar}}}, \tag{2.7}$$

with

P_r = signal power at the receiving antenna after having reached a target in $[W]$.
P_t = power transmitted to the transmit antenna $[W]$.
G_A = Gain factor of the transmit antenna in the preferred direction.
σ = target Radar Cross Section in $[m^2]$.
R = range distance between the antenna and the target in $[m]$.
L_{atmos} = atmospheric loss factor due to the propagating wave.
L_{radar} = microwave transmission loss factor due to the miscellaneous sources.

Noise power In order to obtain the general expression of the *Signal to Noise Ratio* in radar systems, we have to divide equation 2.7 by the noise power. For thermal noise, power density can be approximated as follows, from [7].

$$N_r = kTF_N B_N \tag{2.8}$$

with

N = the received noise power in $[W]$.
k = the Boltzmann's constant $= 1.38 \times 10^{-23} \left[\frac{J}{K}\right]$.
T = the nominal scene noise temperature $\simeq 290\,[K]$.
F_N = the system noise factor for the receiver.
B_N = the noise bandwidth at the antenna port in [Hz].

Consequently, the SNR at the receiving antenna can be written.

$$SNR_r = \frac{P_r}{N_r} = \frac{P_t G_A A_e \sigma}{(4\pi)^2 R^4 L_{\text{radar}} L_{\text{atmos}} (kTF_n) B_N} \tag{2.9}$$

Equation 2.9 is the *Radar Equation* in its most general form, as commonly presented in the literature.

2.3 Radar imaging

In a general way, radar imaging is an application of radar system that consists in creating 2D-pictures of landscapes in order to produce maps. A radar is thus moved along a flight path at a certain height H and illuminates a ground area that is called the *footprint*. A picture created through radar imaging presents two main directions : the *range* direction, perpendicular to the flight direction, and the azimuth direction that refers to the flight direction.
The geometry of a general imaging radar system is presented in Figures 2.3 and 2.3.

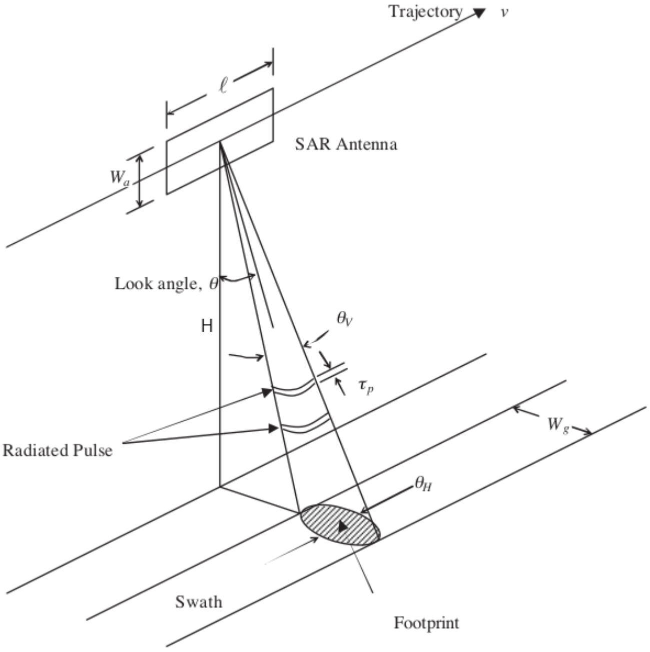

Figure 2.2: 3D-view of a general imaging system geometry, from [6].

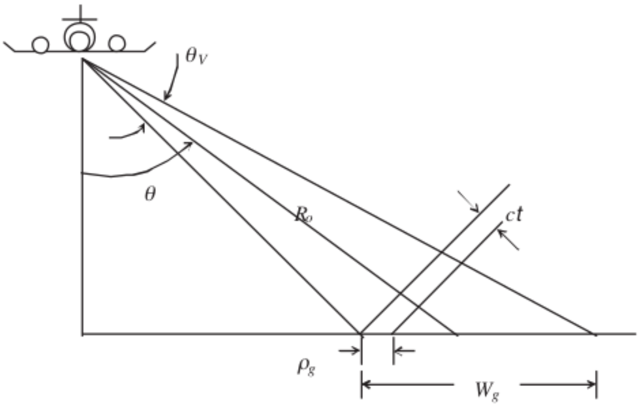

Figure 2.3: 2D-front view of a general imaging system geometry, from [6].

The physical antenna of the radar has a width W_a and a length l. θ_V and θ_H represents the angular across and along-track 3dB beamwidth of the antenna, respectively. From antenna properties defined in [10] we have

$$\theta_H = \frac{\lambda}{l} \tag{2.10}$$

with λ the wavelength of the signal sent by the antenna.

The *radar resolution* is a characteristic of radars describing the ability of a radar to distinguish between targets that are very close. Range resolution is fixed by the bandwidth of the signal transmitted by the radar while the azimuth resolution depends on the antenna length. [2]
We will develop below the advantages of Synthetic Aperture Radar with regards to Real Aperture Radar and briefly overview the main characteristics of both.

2.3.1 Real Aperture Radar (RAR)

Real aperture imaging consists in using an antenna that forms a narrow beam and scan the beam over the region to be imaged. [1] The antenna is thus a *real* physical aperture that receives a delayed signal at each location. For each pulse delay, the system plots the received intensity. Reflections from a larger range arrive back at the radar after a proportionally larger delay, which becomes the range direction of the radar. The radar moves a small distance forward before transmitting the next pulse and a slightly different strip of ground will thus be imaged. [11]

Range resolution

In a general way, ground range resolution ρ_g is the minimal range distance between two targets before they cannot be distinguished anymore. If we use a simple bus of pulses of duration τ_p, this resolution will correspond to the minimal range distance such that the last echoed signal from the first target reached the radar before the first signal returned from the second target.
From Figure 2.3, we can express this distance as a function of the pulse duration τ_p, the wave speed c and the incidence angle of the beam θ_{tilt}.

$$\rho_g = \frac{c\tau_p}{2\sin\theta_{\text{tilt}}} \tag{2.11}$$

where the factor two represents the fact that the waves travels two times the distance between the target and the radar during the time τ_p. We observe that the range resolution is not dependent on the height of the radar, but in its incidence angle.

Azimuth resolution

In a general way, ground azimuth resolution ρ_a is the minimal azimuth distance between two targets before they cannot be distinguished anymore. For a Real Aperture Radar with one antenna, azimuth resolution will depend on the along-track 3dB beamwidth of the antenna as [5]

$$\rho_a = \theta_H \cdot R = \frac{\lambda}{l} \cdot R. \tag{2.12}$$

We observe that the azimuth resolution is dependent on the antenna length and will thus be limited by the available hardware. This is the principal disadvantage of RAR system : it is difficult to reach to enhance azimuth resolution.

2.3.2 Synthetic Aperture Radar (SAR)

Synthetic Aperture Radar (SAR) is a more efficient way to produce radar images. It uses an antenna mounted on a satellite or an airplane that we call *platform* that moves along a flight path. It uses the motion of the radar antenna over the target region to create a large synthetic antenna aperture and thus, to increase the effective antenna length l. Figure 2.4 displays the antenna beam for one SAR acquisition process.

Without adapted post-processing method or specific processing techniques, range and azimuth of SAR systems are equivalent to those of RAR systems presented in equations 2.11 and 2.12, respectively. The only difference is the length of the antenna that will now be defined by the radar path length L_{radar}.

$$\rho_a = \frac{\lambda}{L_{\text{radar}}} \tag{2.13}$$

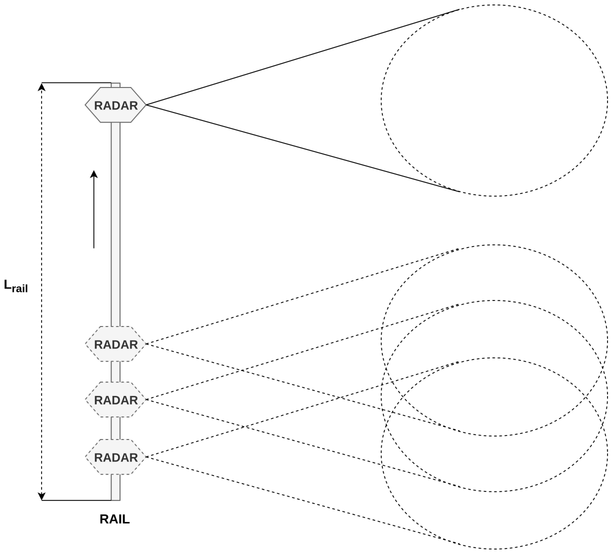

Figure 2.4: Scheme of the antenna beam of a SAR system along the radar path.

Doppler effect

A finer azimuth resolution can be obtained using the *Doppler effect*. It uses the information about the speed of the radar to enhance azimuth resolution.

As a reminder, the Doppler effect defines the increase (or decrease) in the wave frequency that happens when the source and the observer are moving relative to each other. In SAR applications, the radar is the source and it moves relative to the target, that is the observer and that we assume to be motionless. The relative velocity of the radar with regards to the target is v_r. This speed in target (range) direction is given by

$$v_r = \frac{y}{R}v. \tag{2.14}$$

where v is the speed of the radar, and (R, y) the target coordinates. If the signal pulse is sent with a frequency f_0, due to the Doppler effect the frequency received by the target will be expressed as follows, from [4] :

$$f_r = \sqrt{\frac{1 + (v_r/c)}{1 - (v_r/c)}}f_0 = \sqrt{\frac{(1 + (v_r/c))^2}{1 - (v_r/c)^2}}f_0, \tag{2.15}$$

with v_r the relative velocity of the radar, f_0 the initial emitted frequency and c the speed of light. We can assume that $v_r \ll c$ such that $(v_r/c)^2 \simeq 0$ and then :

$$f_r \simeq f_0 \left(1 + \left(\frac{v_r}{c}\right)\right). \tag{2.16}$$

The Doppler shift, denoted f_D and expression the frequency variation due to the Doppler Effect, can be written as

$$f_D = f_r - f_0 \simeq \frac{v_r}{c}f_0 \tag{2.17}$$

Given that the wave travels twice the distance between the source and the radar, the total Doppler shift is, using equation 2.14,

$$f_D = \frac{2v_r}{c}f_0 = \frac{2v \cdot y}{\lambda R}. \tag{2.18}$$

If we isolate y, the azimuth position of the target, in equation 2.18 we find

$$y = \frac{f_D \lambda R}{2v}. \tag{2.19}$$

This new equation allows us to find the increased azimuth resolution for SAR with Doppler effect. The azimuth resolution ρ_a will then depend of the resolution on the Doppler shift ρ_{f_D} which is given as the inverse of the time during which the target is illuminated, t_{ill}, from [12]:

$$\rho_{f_D} = \frac{1}{t_{\text{ill}}} = \frac{v}{\theta_H R} = \frac{vL_{\text{radar}}}{\lambda R} \tag{2.20}$$

Equation 2.20 comes from the fact that the beam width around a target at range R is $\theta_H R$ ((see Figure 2.3). The time during which the target will stay in this beam depends of the speed of the platform v. The resolution is thus :

$$\rho_a = \left(\frac{\lambda R}{2v}\right)\rho_{f_D} = \left(\frac{\lambda R}{2v}\right)\left(\frac{vL_{\text{radar}}}{R\lambda}\right) = \frac{L_{\text{radar}}}{2}. \tag{2.21}$$

Most of the SAR systems presented in the literature use this technique to increase their azimuth resolution.

2.3.3 Pulse Compression

In section 2.3.1, we observed that the range resolution is strongly dependent in the pulse duration τ_p, that has to be very small to optimise the value (see equation 2.11). As a smaller pulse duration leads to a smaller transmitted power, we are not allowed to reduce τ_p without suffering a decreasing image quality due to this loss of power.

To overcome this problem, a technique called *Pulse Compression* [13] is widely used in radar imaging applications.

Instead of sending a pulse with single frequency, pulse compression technique consists in generating a signal with a long chirp duration τ_p and modulates it in frequency. This way, the power is not decreased as τ_p seems to be decreased and thus, the range resolution is optimised without loss of power.

An usual modulation is the linear frequency modulation which leads to an increase of the pulse frequency from f_0 to $f_0 + B$ during τ_p, where B is the bandwidth.

Transmitted signal Without loss of generality the transmitted signal will be :

$$s_t(t) = \operatorname{rect}\left[\frac{t}{\tau_p}\right] A \exp\left[j2\pi\left(f_0 t + \alpha t^2\right)\right] \tag{2.22}$$

where f_0 is the carrier frequency, τ_p the pulse duration, α the frequency rate of the chirp :

$$\alpha = \frac{B}{\tau_p} \tag{2.23}$$

and rect the rectangular function :

$$\operatorname{rect}\left[\frac{t}{T}\right] = \begin{cases} 1 & \text{if } t < T. \\ 0 & \text{elsewhere.} \end{cases} \tag{2.24}$$

Received signal If we receive an echo of the signal from a distance R, we will receive the signal with a delay $\tau = \frac{2R}{c}$. The received signal can thus be written as

$$s_r(t) = \text{rect}\left[\frac{t-\tau}{\tau_p}\right] A\sigma \exp\left[j2\pi\left(f_0(t-\tau) + \alpha(t-\tau)^2\right)\right], \tag{2.25}$$

where the factor σ is the cross section of the target [14] and will simply attenuate the received signal.

Matched filter The next step consists in performing a matched filtering between the received and the transmitted signal. Matched filtering is defined as follows [15]:

$$s_{IF}(t) = \int_{-\infty}^{+\infty} s_r(u) s_t^*(u-t) du \tag{2.26}$$

where $s_t^*(t)$ is the complex conjugate of the emitted signal. Substituting Equations 2.22 and 2.25 in 2.26 gives :

$$\begin{aligned} s_{IF}(t) = \int_{-\infty}^{+\infty} & \text{rect}\left[\frac{u-\tau}{\tau_p}\right] A\sigma \exp\left[j2\pi\left(f_0(u-\tau) + \alpha(u-\tau)^2\right)\right] \\ & \cdot\text{rect}\left[\frac{u-t}{\tau_p}\right] A \exp\left[j2\pi\left(f_0(u-t) + \alpha((u-t)^2\right)\right] du. \end{aligned}$$

This Equation simplifies in :

$$s_{IF}(t) = A^2\sigma\tau_p \exp\left[j2\pi f_0(t-\tau)\right] \text{sinc}\left[\alpha\tau_p(t-\tau)\right], \tag{2.27}$$

with $\text{sinc}(t) = \frac{\sin(t)}{t}$. We see that the result is a cardinal sine function located at the position of the exponential term. This means that a target is represented in temporal domain by a sinc after matched filter.

Increased range resolution We are able to distinguish between two targets if their respective *sinc functions* do not overlap. The width of a cardinal sine is given by the inverse of its frequency, thus we see in Equation 2.27 that :

$$W_{\text{sinc}} = \frac{1}{\alpha\tau_p} = \frac{1}{B} \tag{2.28}$$

where $\alpha\tau_p$ corresponds to the bandwidth B.
The resolution in range when performing pulse compression will thus be equivalent to twice the width of the cardinal sine in Equation 2.27. We finally find the improved range resolution.

$$\rho_g = \frac{c}{2B \sin \theta_{\text{tilt}}} \tag{2.29}$$

Example Figure 2.5 shows an example of the standard pulse emission with regards to the pulse compression technique. We see that with the pulse compression, even when two chirps are overlapping each other we can recover their positions. With the standard pulse emission the close targets cannot be distinguished anymore.

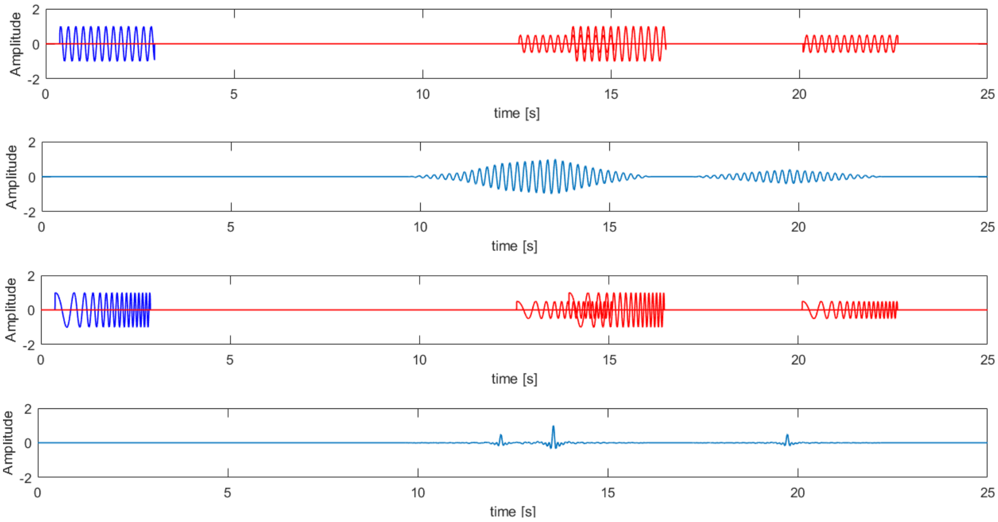

Figure 2.5: Pulse compression technique simulation for three targets (from top to bottom) : signals send (blue) and received (red) for standard pulses, result of the matched filter, signals send (blue) and received (red) for compressed pulses, result of the matched filter.

The result of Equation 2.29 shows that the potential resolution we can achieve using FMCW is much higher than the range resolution we get with standard pulses. In addition this, range resolution only depends on the bandwidth so we do not suffer power limitations anymore.

2.4 Phased Antenna Array

In section 2.3.1, we have seen that the azimuth resolution of an imaging radar system is proportional to the beamwidth of the antenna (when we do not consider the Doppler effect), as presented in equation 2.12. In order to avoid bad azimuth resolution, we thus have to use an antenna with a beam sufficiently narrow.

In this section, we will introduce the concept of antenna array which consists in a technique to narrow the original antenna beam and then increase the azimuth resolution of the system. This technique is applied by the radar we used in this master thesis, as it will be presented in section 6.

Simple antenna Usual antennas have a wide radiation pattern with a low directivity which will lead to a bad angular resolution but also a lower gain. In fact, for the same amount of transmitted power, a more spread beam will have a smaller power density. A way to a achieve narrower beam and then better resolution with only one antenna is, for example, using an antenna with a large radiating aperture (large parabola, or others). [16] However, those antennas lead to the apparition of side lobes and they are more difficult to fabricate or expensive.

Antenna array Another way to get a beam with a good directivity is a combination of simple radiating elements (like wire dipoles that get low directivity) dispatched in a specific configuration to construct a so called antenna array. The idea is to create a field that will result in constructive interference of all the elements of the array in one direction and in destructive interference in other directions. This is known as beamforming. To manage this, we can play on d, the spacing between the array elements, A the amplitude of the field produced by each of them , ϕ the phase between those elements or N, the number of elements itself .
Figure 2.6 shows a schematic view of an antenna array where we consider that the incoming wavefronts are planar (see Section 3).

Mathematical description The initial electric field produce by the i^{th} element (a_i) is $E_{i,0}$. It presents a polarisation and an amplitude [17] such that the field emitted by the element a_i arriving at the target position can be written as in equation 2.30, the Euclidean distance between the array element a_i and the target P being R_i.

$$\mathbf{E}_i(P) = E_{i,0}(\theta, \gamma)\frac{e^{-j(kR_i+\phi)}}{R_i} \approx E_i(\theta, \gamma)\frac{e^{-j(k(R+d\cos\theta)+\phi)}}{R}. \tag{2.30}$$

where k is the wave number $k = \frac{2\pi}{\lambda}$, θ and γ the elevation and azimuths angle of the antenna element radiating patterns, respectively. We will consider that the radiating pattern of an element is omnidirectional such that $E_{i,0}$ is independent of θ or γ. The phase ϕ is a phase that can be artificially introduced to the emitted (and then received) wave. We can simplify equation **??** if we suppose that the target is far enough such that the amplitude attenuation is the same for all the

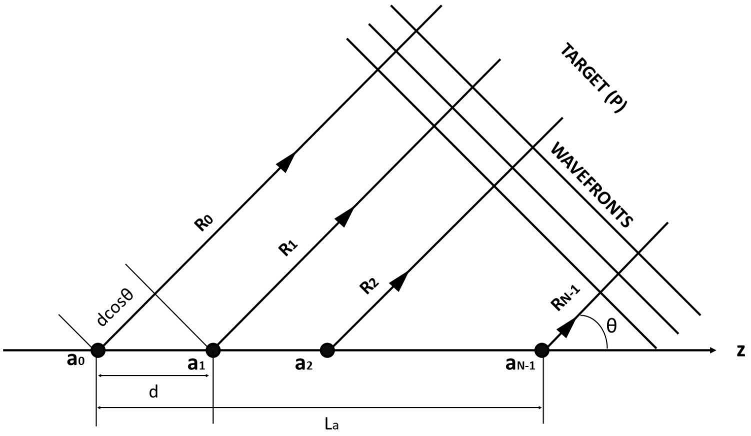

Figure 2.6: Schema of an antenna array made of N elements (a_i). The wavefronts are planar and come from a target P to the antenna elements that are spaced by a distance d. The total length of the array is $N \cdot d = L_a$ and the angle at which the target is located with regards to the center of the array axis is θ.

emitted fields. This means that the term R_i on the numerator can be replaced by a term R, common to all the elements.
Using simple trigonometric relations, we can see that the distance between the point a_i and the target (R_i) is the same as the distance between the point A_{i+1} added to the small distance $d\cos\theta$ (see Figure 2.6) : $R_i = R_{i+1} + d\cos\theta$. The total received field at the target position will thus be the sum of all incoming waves. If we suppose that the phase ϕ is the same between all the elements ($\phi_i - \phi_{i+1} = \phi$) and that all elements radiate the same initial field ($E_{i,0} = E_0$), we get :

$$E(P) = E_0 \cdot \underbrace{\sum_{n=0}^{N-1} e^{jn(d\cos\theta+\phi))}}_{A_f}. \tag{2.31}$$

The first term only depends of the radiating pattern of the array element while the second term in Equation 2.31 is called the Array Factor A_f and depends in d, ϕ and θ. We can develop the sum of exponential functions using :

$$\sum_{n=0}^{N-1} e^{Nx} = \frac{e^{Nx} - 1}{e^{x} - 1}. \tag{2.32}$$

And after some mathematical developments [18] and denoting $\Psi = d\cos\theta + \phi$, we find :

$$A_f = e^{j\left(\frac{N-1}{2}\right)\Psi} \cdot \frac{\sin\left(\frac{N\Psi}{2}\right)}{\sin\left(\frac{\Psi}{2}\right)}. \tag{2.33}$$

The factor $e^{j\left(\frac{N-1}{2}\right)\Psi}$ is a phase shift of the array's phase center relative to the origin and it would be equal to one if the origin coincides with the array center [19]. We will then neglect this term from now. The Array Factor defines the shape of the radar beam given the quantities d, ϕ or N. Now, we thus need to find the characteristics of the main lobe of A_f from Equation 2.33.

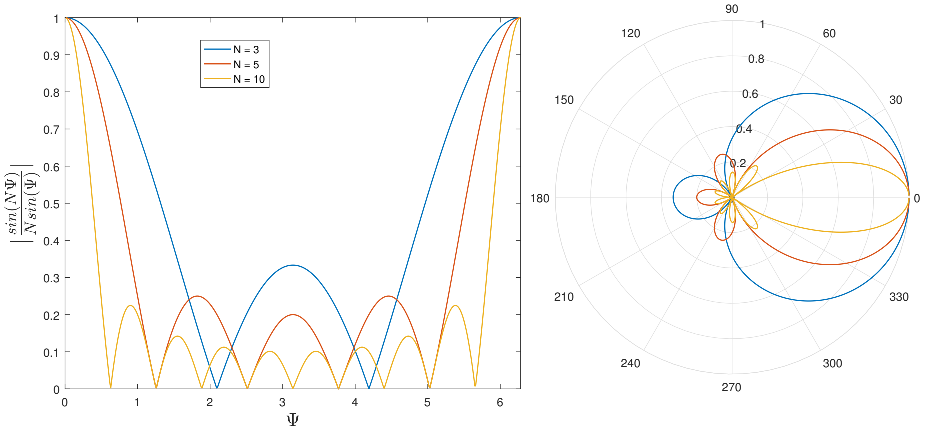

Figure 2.7: Normalised array factor for multiple numbers of elements N in Cartesian plot (left) and polar plot (right). We see that as the number of elements increase, the peak becomes narrower.

We first want to find the width of the main lobes which corresponds to the distance between the first two zeros :

$$\sin\left(\frac{N\Psi}{2}\right) = 0 \Rightarrow \Psi = \pm\frac{2n\pi}{N} \quad , \text{n} = 1{,}2{,}3{,}.... \tag{2.34}$$

Given that $\Psi = kdcos\theta + \phi$ we can write :

$$\theta_0 = \cos^{-1}\left[\frac{1}{kd}\left(\pm\frac{2n\pi}{N} - \phi\right)\right] = \cos^{-1}\left[\frac{\lambda}{2\pi d}\left(\pm\frac{2n\pi}{N} - \phi\right)\right]. \tag{2.35}$$

We see that if the distance d between the elements increases (for the same N and ϕ) the distance between the zeros decreases and then the peak becomes narrower. The

same behaviour appends when we increase the number of elements N. Changing ϕ will shift the positions of the zeros and then will move the main lobe.
The Figure 2.7, 2.8 and 2.9 shows the behaviour of the radiation pattern of the array when we change those values.

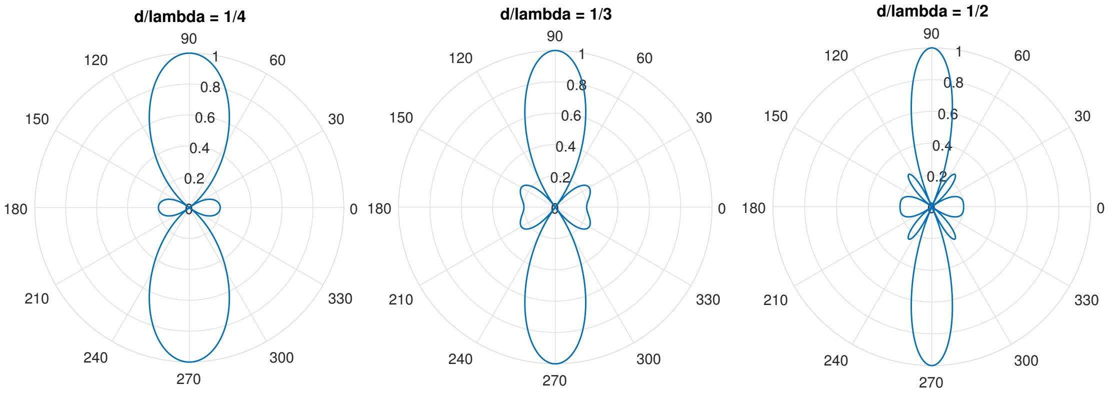

Figure 2.8: Pattern of the array antenna for $\frac{d}{\lambda} = \frac{1}{4}, \frac{1}{3}$ and $\frac{1}{2}$ with 5 array elements. We see that reducing the distance between the antenna array elements reduces the number of lobes but increases their sizes.

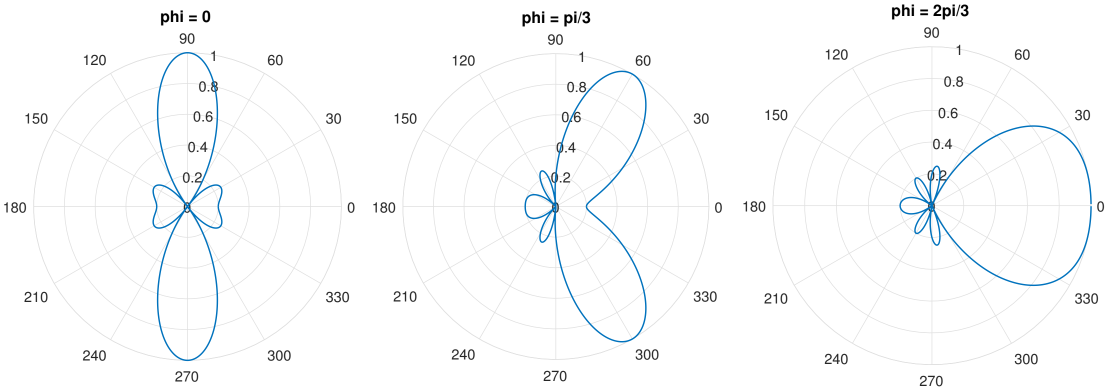

Figure 2.9: Array factor for multiple values of $\phi = 0$, $\frac{\pi}{3}$ and $\frac{2\pi}{3}$ for N = 5 and $\frac{d}{\lambda} = \frac{1}{3}$. We see that when we change the phase ϕ the lobe positions move.

We will see in section 6.2 that the radar we use is based on this principle to generate a beam focused in a particular direction, improving the range resolution of our SAR system.

2.5 What about us ?

In this master thesis, we are working at small scale with a radar that is moved along a rail. The main objective is to develop a model that allows us to understand the impact of the small range on the applications and the precision of the system. Based on this model, we aim at extracting the equations and constraints necessary to properly design physical setups and perform adapted measurements.

As presented in section 6.2, we are working with a radar that implements an antenna array of nine elements in order to increase its azimuth resolution. This radar sends Frequency Modulated Continuous Waves (FMCW) and the range resolution thus depends on its bandwidth.

As we do not have a motorised rail, we have to move the radar manually and we cannot perform a continuous acquisition. We are thus forced to discretise the radar path without considering any speed for the radar, only displacement.

We have performed multiple experiments that allowed us to test and verify the validity of our model, such as the assumption that we have made to develop it.

Chapter 3

Far Field Approximation

In section 2.4 we have supposed that the wavefronts of the emitted and received waves were planar, which allowed us to simplify the mathematical developments. However, this assumption is valid only if the target is sufficiently far from the radar with regards to his aperture Ω. The SAR model that we develop in section 4 also requires this assumption. Thus, we need to develop the condition that has to be fulfilled to properly apply the assumption and adapt it to our model. The condition that has to be fulfilled is called the *Fraunhofer Approximation*. In this chapter, we first develop the general expression (for any aperture shape) of this approximation and then we will apply it to SAR geometry.

3.1 Mathematical developments

If we suppose a general aperture of random shape for our radar (Figure 3.1), the Fraunhofer approximation tells us that if the aperture is small enough compared to the distance of the illuminated target, the amplitude and phase error made when we approximate the incoming wave as planar is small enough to neglect the curvature of the wave.

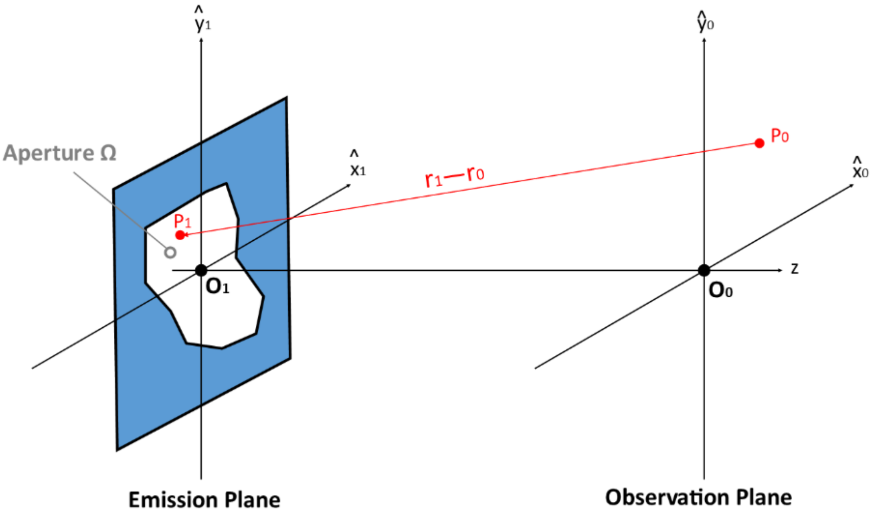

Figure 3.1: [20] Schema of the transmission of a EM wave through an aperture. The radar aperture is placed in the plane $\{O_1, \hat{x}_1, \hat{y}_1\}$ while the illuminated object is placed in plane $\{O_0, \hat{x}_0, \hat{y}_0\}$.

Given the Figure 3.1, we assume that the aperture $\Omega \in \mathbb{R}^3$ lies in the plane $\{O_1, \hat{x_1}, \hat{y_1}\}$ and the monochromatic wave U comes from this aperture, propagates to the right of the figure and goes to the plane of observation $\{O_0, \hat{x_0}, \hat{y_0}\}$ placed at a distance z from the aperture plane $\{O_1, \hat{x}_1, \hat{y}_1\}$. From the Huygens principle, we know that at point $P_0 = (x_0, y_0)$ in the observation plane, the field is given by the integration over the aperture of all the points seen as emitters $U(x_1, y_1)$. This field is modified in phase and amplitude depending in the Euclidean distance between those points and P_0. If we write the distance between a point in the observation field $r_1 = (x_1, y_1, z_1)$ and a point in the aperture $r_0 = (x_0, y_0, z_0)$ as $\|r_1 - r_0\|$, the Fraunhofer Approximation lies on the principle that the change in phase and in amplitude of the emitted wave can be neglected when r_1 changes in the aperture. We express this field as [21] :

$$U(x_0, y_0) = \int\int_{\sigma} h(x_0, y_0, x_1, y_1) U(x_1, y_1) dx_1 dy_1. \tag{3.1}$$

with h the propagation function of the wave given by :

$$h(x_0, y_0, x_1, y_1) = \frac{-1}{j\lambda} \frac{e^{-jk\|r_1 - r_0\|}}{\|r_1 - r_0\|}. \tag{3.2}$$

and the distance between a point in the observation plane and P_0 is :

$$\|r_1 - r_0\| = \sqrt{z^2 + (x_0 - x_1)^2 + (y_0 - y_1)^2} \tag{3.3}$$

$$= z\sqrt{1 + \left(\frac{x_0 - x_1}{z}\right)^2 + \left(\frac{y_0 - y_1}{z}\right)^2}. \tag{3.4}$$

If the distance z is much larger than the dimensions x and y of the problem, a variation of $\|r_1\|$ does not change so much the distance $\|r_1 - r_0\|$ and then the amplitude variation in the integral. This is easily valid for the amplitude variation but we must be careful with the fact that we cannot simplify the phase argument with the same facility. In fact, the phase can vary much faster than the amplitude, even for small variation of $\|r_1 - r_2\|$. We can simplify the Equation 3.2 as :

$$h(x_0, y_0, x_1, y_1) \approx \frac{-1}{j\lambda z} e^{-jk\|r_1 - r_0\|}. \tag{3.5}$$

This approximation only add a small additive error which means that the amplitude of the signal will be modified but this does not cause any problematic concerns in our model.

As $z > (x_0 - x_1)$ and $(z > (y_0 - y_1)$, we can develop the distance using the first order Taylor expansion (i.e. $\hat{f}(\alpha) = f(0) + f'(0)(\alpha - 0)$ $\sqrt{1+\alpha} \approx 1 + \frac{1}{2}\alpha$ [22]) and retain only the first two terms. We get :

$$\|r_1 - r_0\| \approx z\left[1 + \frac{1}{2}\left(\frac{x_0 - x_1}{z}\right)^2 + \frac{1}{2}\left(\frac{y_0 - y_1}{z}\right)^2\right]. \tag{3.6}$$

Which gives for h :

$$h(x_0, y_0, x_1, y_1) \approx \frac{-1}{j\lambda z} e^{-jkz\left[\frac{1}{2}\left(\frac{x_0 - x_1}{z}\right)^2 + \frac{1}{2}\left(\frac{y_0 - y_1}{z}\right)^2\right]}. \tag{3.7}$$

The Taylor expansion introduces an error in the phase $\mathcal{O}\left(\alpha^2\right)$ with $\alpha = \left(\frac{x_0 - x_1}{z}\right)^2 + \left(\frac{y_0 - y_1}{z}\right)^2$.
If we substitute Equation 3.7 in Equation 3.1 we finally obtain

$$U(x_0, y_0) = \frac{-e^{-jkz}}{j\lambda z} \int\int_\sigma U(x_1, y_1) e^{-\frac{jk}{2z}\left[1 + (x_0 - x_1)^2 + (y_0 - y_1)^2\right]} dx_1 dy_1. \tag{3.8}$$

If we only keep the term depending of x_1, y_1 inside the integral we have

$$U(x_0, y_0) = \frac{-e^{-jkz}}{j\lambda z} e^{-\frac{jk}{2z}\left[x_0^2 + y_0^2\right]} \int\int_\sigma U(x_1, y_1) e^{-\frac{jk}{2z}\left[x_1^2 + y_1^2\right]} e^{\frac{jk}{2z}\left[x_0 x_1 + y_0 y_1\right]} dx_1 dy_1. \tag{3.9}$$

The Equation 3.9 is usually called the *Fresnel Diffraction Integral* [23]. This result is interesting because if we observe it carefully, we can recognize a 2-D Fourier transform of the field inside :

$$U(x_1, y_1)e^{-\frac{jk}{2z}\left[x_1^2+y_1^2\right]}. \tag{3.10}$$

with the spatial frequencies :

$$f_x = -\frac{x_0}{\lambda z} \quad \text{and} \quad f_y = -\frac{y_0}{\lambda z},$$

$\lambda = \frac{c}{f_0}$ being the wavelength.
All the approximations made here are valid if we are not too close from the aperture. One sufficient but not necessary condition is that the higher order term in the binomial expansion is small enough. In fact, we just need that it does not change too much the result of the integral which is often respected.
The Fraunhofer approximation supposes that the distance between the two planes is large enough such that the exponential term in Equation 3.10 is close enough to 1 and becomes negligible:

$$z \gg \frac{k\left[x_1^2+y_1^2\right]}{2}. \tag{3.11}$$

and this for the maximum value of x_1 and y_1 in the aperture.
The Equation 3.9 finally becomes :

$$U(x_0, y_0) = \frac{-e^{-jkz}}{j\lambda z}e^{-\frac{jk}{2z}\left[x_0^2+y_0^2\right]}\int\int_\sigma U(x_1, y_1)e^{\frac{jk}{2z}\left[x_0x_1+y_0y_1\right]}dx_1dy_1. \tag{3.12}$$

This means that the field in the observation plane is the Fourier transform of the field in the aperture plane with the two frequencies $f_x = -\frac{x_0}{\lambda z}$ and $f_y = -\frac{y_0}{\lambda z}$. The condition described by Equation 3.11 is called the *far-field* region while the model of the *Fresnel Diffraction Integral* is called the *near-field* region.

3.2 Application to our small range SAR

In the case of a SAR system, the aperture is reduced to a line segment because we the emitting source $U(x_1, y_1)$ is moved on a line of size L. Figure 3.2 shows a schematic view of the problem. The aperture is a straight line from y = $-\frac{L}{2}$ to $\frac{L}{2}$ and the observation point is P at a distance R from a point in the aperture. We

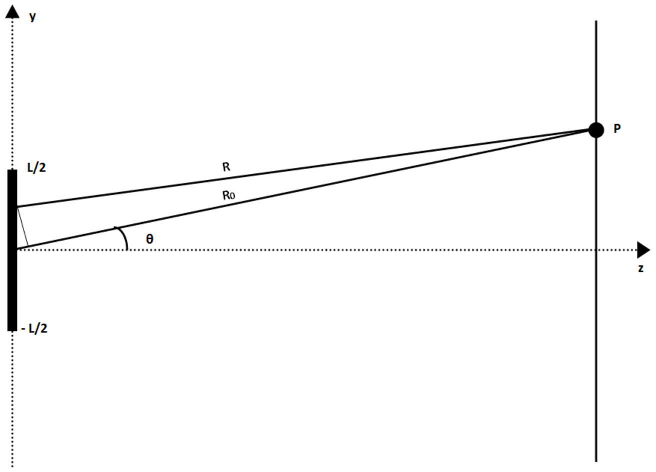

Figure 3.2: Schema of the aperture set-up for our SAR system. The length of the aperture is L and and is in the y-plane, a target point P is at a distance R_0 from the center and the angle between the axic of the aperture and the point is θ.

assume that all the source points have the same amplitude and initial phase.

From Equation 3.11 we can find the condition for the validity of the Fraunhofer approximation by considering that the maximum distance in the aperture is the length of the rail (L), and is thus $[x_1^2 + y_2^2] \to L^2$. The condition becomes :

$$z \gg \frac{kL^2}{2} = \frac{\pi L^2}{\lambda}. \tag{3.13}$$

This Equation shows we must constraint the length of the rail of our small scale SAR application to a very low value with regards to the usual flight path of airborne SAR, that performs at high altitude. We must also notice that the Fraunhofer condition is not precisely defined and thus, there remains a degree of freedom in the verification of the condition.
If the Fraunhofer condition is respected, the point P is far enough with regards to the aperture such that the distances R and R_0 can be considered as parallel. The distance from P to a point in the aperture at y and from P to the center of the aperture are then slightly different. This differences can be written as

$$\Delta R = -y \sin\theta. \tag{3.14}$$

This mean that the phase difference between them will be $-\frac{2\pi y \sin\theta}{\lambda} = -ky\sin\theta$ and then, we can write the field at point P assuming $U(P) = U(\theta)$, as presented below.

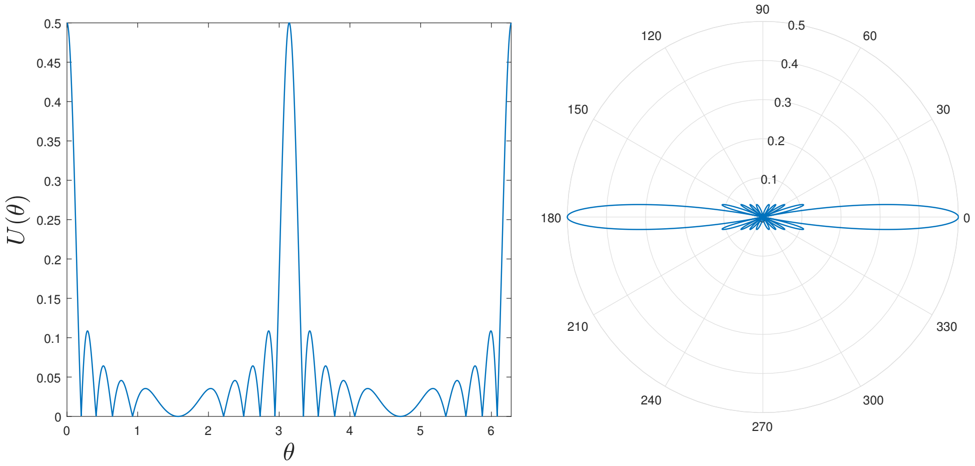

Figure 3.3: Radiation pattern of the SAR aperture for $\lambda = 0.5$ m, L = 0.5 m and no phase shift.

$$U(\theta) = \frac{-e^{-jkR_0}}{j\lambda R_0} \int_{-\frac{L}{2}}^{\frac{L}{2}} U(y) e^{-jkysin\theta} dy. \tag{3.15}$$

The radiated field is here expressed using the angle θ in order to simplify the notations. In fact, we assume that the radiated field along the aperture is uniform and normalized so the observed field only depends of the angle at which the point is seen and then, $U(y) = 1$. To simplify the integral, we define : $\tau = k \sin \theta$. The Fraunhofer integral becomes

$$P(\tau) = \int_{-\frac{L}{2}}^{\frac{L}{2}} e^{-j\tau y} dy = \frac{e^{j\tau\frac{L}{2}} - e^{-j\tau\frac{L}{2}}}{j\tau} = Lsinc\left(\frac{\tau L}{2}\right). \tag{3.16}$$

Substituting $\tau = k \sin \theta$ we find

$$U(\theta) = L\text{sinc}\left(\frac{kL\sin\theta}{2}\right). \tag{3.17}$$

We see in Figure 3.3 that the resulting beam of the SAR aperture is similar to that of an antenna array. The longer the aperture, the better the resolution because the main lobe becomes narrower. If we introduce a phase shift between successive radiating points in the aperture, we can orient the beam in a desired direction. This is the case for the *Spotlight SAR* where the radar beam is permanently oriented to a target area during the travelling of the antenna [24]. We see here the link between SAR system and antenna arrays that we developed in section 2.4.

3.3 Discussion

We see that the Far Field Approximation must be used carefully for our small range application, using a small rail. This will lead to a trade-off between a higher azimuth resolution that increase with the length of the rail and the amount of distortion introduced by the Fraunhofer approximation. Those effects will be discussed in section 7.

Chapter 4

Model Development

In this chapter, we develop a model for the emitted and received signals in a general system. We start from a basic configuration where a radar is moved along a path in a certain direction, sending a chirp and waiting it to come back at each position. By expressing the signals in a simplified form, we aim at performing radar imaging with the tools presented in section 5.

4.1 Notations

This section overviews all the parameters that are used for the model development.

Carrier frequency	f_0
Bandwidth	B
Light speed	c
Radar speed	v
Radar height	H
Range distance	$R(x, y, t)$
Range distance for $y = 0$	R_x
Delay between the emitted and received signals	τ
Chirp duration - slow time sampling period	T_c
Fast time sampling period	T_s
"Fast" time	t
"Slow" time	t'
Fast time sampling frequency	f_s
Slow time sampling frequency	f_c
Number of samples in range direction (fast time sampling)	M
Number of samples in azimuth direction (slow time sampling)	N
Aperture angle of the radar	θ
Rail length (radar path length)	L_{rail}

Wavelength	λ
Distance between the radar and the target	L_{target}
Sinus of the aperture angle of the radar	α

4.2 Geometrical description

The geometry that we are considering for SAR applications studied in this master thesis is presented in Figure 4.1. We are working in a 3D coordinate system $\{O, \hat{x}, \hat{y}, \hat{z}\}$. A radar is moved in y-direction ("azimuth") at a speed v, at constant height H. The target is located in $(x, y, -H)$ and is observed by the radar under constant x.

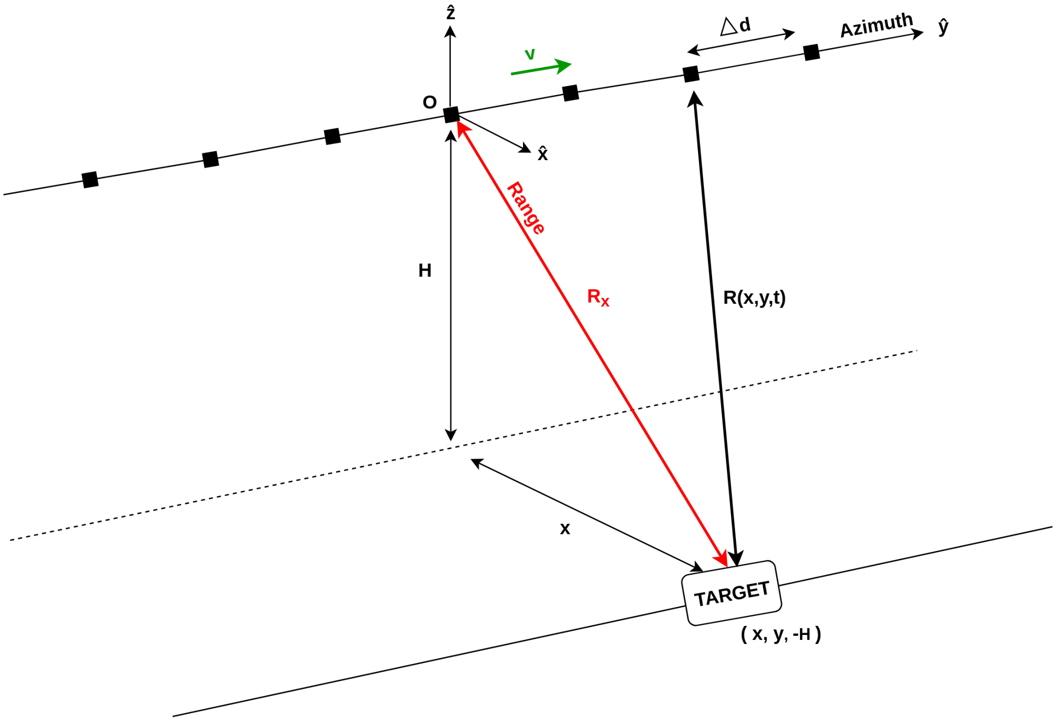

Figure 4.1: Geometrical definition of the problem. v is the speed of the antenna along the y-axis. x_t is the distance along the x-axis between the target and the radar, $R(x, y, t)$ is the distance between the target and the radar ("range"), Δd is the step of displacement performed by the radar after a time T_c (time of a chirp).

Slow and fast time In order to properly model the problem, we will consider two different time dimensions. First we have the *azimuth time* that characterises the displacement of the radar. Second we have the *range time*, that describes the radar signal sampling and that is thus much faster than the first. We will denote

- t' - the *fast time*, in range direction.
- t - the *slow time*, in azimuth direction.

Chapter content In this chapter, we will develop the model that will be used to build a real version of the system presented in Figure 4.1. More precisely, we will be interested in recovering the range and the azimuth distances between the radar and the targets. More precisely, we will discretise a 2D domain $\{(x_i, y_j) \ 1 \leq i \leq M, 1 \leq j \leq N\}$ in order to reconstruct a function $f(x_i, y_j)$ with $f(x_i, y_j) \neq 0$ if there is a target t in (x_i, y_j). First we will develop a complete model of the signal recovered by the radar as a function of the parameters of interest. Second we will simplify this model in order to obtain an expression of the form

$$f(x, y) = f_x(x, t) \cdot f_y(y, t'), \tag{4.1}$$

where t' and t symbolises fast and slow time dimensions and x and y space coordinates.

4.3 Hypotheses

Start and stop As presented in Figure 4.1, we are considering a radar moving at a speed v along the y-axis. For the sake of simplicity and to be closer to our real problem, we will work with a "Start and Go" setup, meaning that the radar performs acquisition at fixed points on its path and does nothing while it is moving to the next point. This can be seen as a sampling in the azimuth direction.

Far field To describe the problem further, we need to use the far field approximation explained in section 3. We will consider that the distance travelled by the radar is much lower than the distance between the radar and the target. The implications of this approximation and its validity will be discussed in Chapter 7.

Range distance We define $R(x, y, t)$ as the range distance between the radar in $(0, vt, 0)$ and the target in $(x, y, -H)$, as presented in Figure 4.1. We have

$$\begin{aligned} R(x, y, t) &= \left|\left|(x, y, -H)^T - (0, vt, 0)^T\right|\right| && (4.2) \\ &= \sqrt{x^2 + H^2 + (y - vt)^2}. && (4.3) \end{aligned}$$

In order to simplify this expression and remove y of the square root, we consider the situation presented in Figure 4.1, where the target is located right in front of the radar in $y = vt$. We then perform a Taylor expansion around $(y - vt)^2 = 0$.

Physically, we thus approximate the distance around the point where the aircraft is right in front of the target, and thus we use the fact that we do not move a lot in regards with the target. This is consistent with the **far field** consideration presented above.

$$
\begin{aligned}
R(x,y,t) = & \quad \sqrt{H^2 + x^2 + (y - vt)^2} && (4.4)\\
\overset{\text{Taylor}}{\simeq} & \quad \sqrt{H^2 + x^2} + \frac{(y - vt)^2}{2\sqrt{H^2 + x^2}} && (4.5)\\
= & \quad R_x + \frac{(y - vt)^2}{2R_x}, && (4.6)
\end{aligned}
$$

with R_x the distance between the radar and the target when the radar is right in front of the target ($y = vt$).

4.4 Continuous signal model

To develop the continuous model, we consider that the radar moves continuously along the y-axis. As we are working with pulses, we have to constrain the fast time to a chirp duration, as this temporal dimension is defined for each chirp. We express that condition on the fast time as

$$t'_{\text{chirp}} = (t' \mod T_c), \tag{4.7}$$

where T_c is the duration of a chirp in $[s]$.

Transmitted signal The transmitted signal is a Frequency Modulated Continuous Wave (FMCW) at a carrier frequency f_0 and with a chirp duration T_c. For the sake of readability, we have made the integral dimensionless by integrating over $\frac{t'_{\text{chirp}}}{T_c} = \left(\frac{\theta}{T_c} \mod 1\right) d\theta$ instead of $t'_{\text{chirp}} = (\theta \mod T_c)\, d\theta$.

$$s_t(t) = \exp\left[2\pi j \left(f_0 t + \int_0^{t'_{\text{chirp}}} \left(\frac{\theta}{T_c} \mod 1\right) B d\theta\right)\right], \tag{4.8}$$

where f_0 is the carrier frequency and B the bandwidth, both expressed in [Hz].

Received signal The received signal is a delayed version of the transmitted one. As we will evolve to a "Start and Stop" configuration for the discretisation, we can consider that $v \ll c$ and thus express the delay as follows.

$$\tau \overset{v \ll c}{\simeq} \frac{2R(x,y,t)}{c} \qquad [s]\,. \tag{4.9}$$

In fact, neglecting the speed of the radar during an acquisition corresponds to considering that the radar does not move during acquisition, which is consistent with our "Start and Stop" configuration. The received signal at radio frequency is described by equation 4.12.

$$\begin{aligned}
s_r^{RF}(t) &= s(t-\tau) && (4.10)\\
&= s\left(t - \frac{2R(x,y,t)}{c}\right) && (4.11)\\
&= \exp\left[2\pi j\left(f_0(t-\tau) + \int_0^{t'_{\text{chirp}}-\tau}\left(\frac{\theta}{T_c} \mod 1\right)Bd\theta\right)\right]. && (4.12)
\end{aligned}$$

Coherent demodulation In order to bring the received signal back in base band, we perform a coherent demodulation. This is achieved by multiplying the signal presented in equation 4.12 with the conjugate of the emitted signal, both at radio frequency.

$$\begin{aligned}
s_r^{BB}(t) &= s_r^{RF}(t)\cdot s_t^{RF,*}(t) && (4.13)\\
&= s_t^{RF}(t-\tau)\cdot s_t^{RF,*}(t). && (4.14)
\end{aligned}$$

By replacing the signals with their expressions, we obtain :

$$\begin{aligned}
s_r^{BB}(t) &= \exp\left[2\pi j\left(f_0(t-\tau) + \int_0^{t'_{\text{chirp}}-\tau}\left(\frac{\theta}{T_c} \mod 1\right)Bd\theta\right)\right]\\
&\quad\cdot\exp\left[-2\pi j\left(f_0 t + \int_0^{t'_{\text{chirp}}}\left(\frac{\theta}{T_c} \mod 1\right)Bd\theta\right)\right] && (4.15)\\
&= \exp\left[2\pi j\left(-f_0\tau - \int_{t'_{\text{chirp}}}^{t'_{\text{chirp}}-\tau}\left(\frac{\theta}{T_c} \mod 1\right)Bd\theta\right)\right] && (4.16)\\
&= \exp\left[2\pi j\left(-f_0\tau + \int_{t'_{\text{chirp}}-\tau}^{t'_{\text{chirp}}}\left(\frac{\theta}{T_c} \mod 1\right)Bd\theta\right)\right]. && (4.17)
\end{aligned}$$

The next step is the integration in equation 4.17. The purpose of this integral is to compare the emitted to the received chirp in order to obtain the corresponding delay. The modulo operator prevents comparison between two chirps that are not in the same pulse period. Non-integrable zones avoided with the modulo are presented in red in Figure 4.2. To simplify the integration we remove the modulo operator and replace it by a range for t, that have to stay in the blue zone of Figure 4.2.

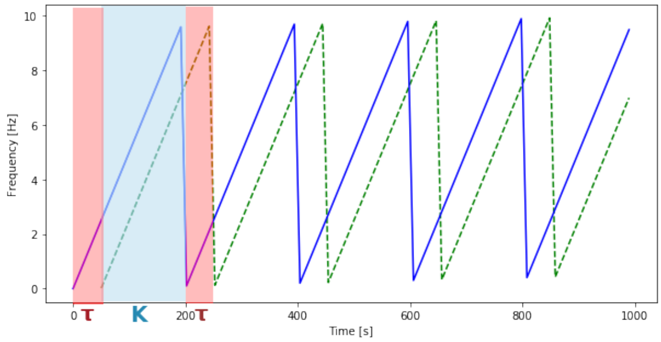

Figure 4.2: Frequency Modulation of the signal emitted and received, with integrable zone in blue and non-integrable zone in red.

The **coherence and non-overlap** condition presented in equation 4.18 allow us to remove the modulo operator and to perform the integration properly. For a sake of readability, we will denote t' the fast time corresponding to a chirp, instead of t'_{chirp}.

$$t'_{\text{chirp}} = t' \quad \in \quad [nT_c + \tau_{max} \quad (n+1)T_c - \tau_{max}] \tag{4.18}$$

n corresponds to the radar step number and τ_{max} the maximal observable delay in $[s]$. We observe that equation 4.18 implies $\tau_{max} < T_c$, which is intuitively consistent with our "Start and Stop" configuration. In fact, the delay between the transmitted and received signals will always be lower than the chirp duration, as T_c corresponds to one position of the radar and the radar won't move without having received the signal back.

Integration With the acceptable range 4.18 for t in mind, we can now compute the integral in signal 4.17.

$$\begin{aligned}
s_r^{BB}(t) &= \exp\left[2\pi j\left(-f_0\tau + \int_{t-\tau}^{t}\left(\frac{\theta}{T_c} \mod 1\right)Bd\theta\right)\right] && (4.19)\\
&= \exp\left[2\pi j\left(-f_0\tau + \int_{(t-\tau) \mod T_c}^{t \mod T_c}\frac{\theta}{T_c}Bd\theta\right)\right] && (4.20)\\
&= \exp\left[2\pi j\left(-f_0\tau + \left[\frac{\theta^2}{2\cdot T_c}B\right]_{(t-\tau) \mod T_c}^{t \mod T_c}\right)\right] && (4.21)\\
&= \exp\left[2\pi j\left(-f_0\tau + \frac{(t \mod T_c)^2}{2\cdot T_c}B - \frac{(t \mod T_c)^2}{2\cdot T_c}B\right)\right]\\
&\quad \cdot \exp\left[2\pi j\left(\frac{2(\tau \mod T_c)(t \mod T_c)}{2\cdot T_c}B + \frac{(\tau \mod T_c)^2}{2\cdot T_c}B\right)\right] && (4.22)
\end{aligned}$$

As we are working in a "Start and Stop" configuration, we can assume that the delay τ will never exceed the time of a chirp and thus replace $(\tau \mod T_c)$ by τ, as explained above.

$$s_r^{BB}(t)\exp\left[2\pi j\left(-f_0\tau+\left[\frac{2\tau(t \mod T_c)}{2\cdot T_c}B-\frac{\tau^2}{2\cdot T_c}B\right]\right)\right] \tag{4.23}$$

$$\tag{4.24}$$

Furthermore, we define $t'=(t \mod T_c)$ as the fast time, in azimuth direction.

$$s_r^{BB}(t,t')=\exp\left[2\pi j\left(-f_0\tau+\frac{2\tau t'}{2\cdot T_c}B-\frac{\tau^2}{2\cdot T_c}B\right)\right] \tag{4.25}$$

Delay expression As we are interested in range and azimuth target's coordinates, we inject the delay expression 4.9 in equation 4.25 and develop the terms to obtain a complete expression of the received signal, in function of R_x and y. We use the Taylor expansion of the range in 4.6 for τ and the exact expression in 4.2 for τ^2.

$$\tau=\frac{2R(x,y,t)}{c}\simeq\frac{2}{c}\left(R_x+\frac{(y-vt)^2}{2R_x}\right) \tag{4.26}$$

$$\tau^2=\frac{4R^2(x,y,t)}{c^2}=\frac{4}{c^2}\left(R_x+(y-vt)^2\right) \tag{4.27}$$

with $R_x=\sqrt{H^2+x^2}$ the range distance between the radar and the target when the radar is right in front of the target. We obtain

$$\begin{aligned}s_r^{BB}(t,t')=&\exp\left[-2\pi jf_0\frac{2}{c}\left(R_x+\frac{(y-vt)^2}{2R_x}\right)\right]\cdot\exp\left[2\pi j\frac{B}{cT_c}\frac{2}{c}\left(R_x+\frac{(y-vt)^2}{2R_x}\right)t'\right]\\&\cdot\exp\left[-2\pi j\frac{B}{cT_c}\frac{4}{c^2}\left(R_x^2+(y-vt)^2\right)\right].\end{aligned} \tag{4.28}$$

By developing and sorting terms we obtain equation 4.29.

$$\begin{aligned} s_r^{BB}(t,t') = {} & \underbrace{\exp\left[-4\pi j\left(\frac{R_x}{c}f_0+\frac{B}{c^2T_c}R_x^2+\frac{f_0}{c}\frac{y^2}{2R_x}-\frac{B}{c^2T_c}y^2\right)\right]}_{\text{Constant phase}} \\ & \underbrace{\cdot\exp\left[4\pi j\left(\frac{B}{cT_c}R_x+\frac{B}{cT_c}\frac{y^2}{2R_x}\right)t'\right]}_{\text{Fast time dependent}} \\ & \underbrace{\cdot\exp\left[4\pi j\left(\frac{f_0}{c}\frac{y}{R_x}+2\frac{B}{c^2T_c}y\right)vt\right]\cdot\exp\left[-4\pi j\left(\frac{f_0}{c}+\frac{B}{c^2T_c}\right)(vt)^2\right]}_{\text{Slow time dependent}} \\ & \underbrace{\cdot\exp\left[-4\pi j\frac{B}{cT_c}\frac{y}{R_x}t't\right]\cdot\exp\left[4\pi j\frac{B}{cT_c}\frac{v^2}{R_x}t't^2\right]}_{\text{Slow and fast time dependent}} \end{aligned} \tag{4.29}$$

As a reminder, we have obtained this expression of the received signal by developing a model based on the configuration of Figure 4.1 and using Frequency Modulated Continuous Waves (FMCW). Three hypotheses have been made :

1. We are considering our configuration as a "Far Field" problem.
2. The range distance $R(x,y,t)$ has been approximated with a Taylor expansion of order 1 around
$$(y-vt)^2 = 0. \tag{4.30}$$
3. We are working with a "Start and Stop" configuration. It is not an approximation in our case, but still constraints applications of our model.

4.5 Discretisation

As we model our problem by considering two temporal dimensions, we also have to consider two temporal samplings :

- $t' = mT_s\ \ [s]$ – the *fast time* sampling, in range direction.
- $t = nT_c\ \ [s]$ – the *slow time* sampling, in azimuth direction.

With $m \in \{0,...,M-1\}\ \ [\backslash]$ and $n \in \{0,...,N-1\}\ \ [\backslash]$, M and N being the number of samples in range and azimuth directions respectively. T_s and T_c are the sampling periods in both temporal dimensions, in $[s]$. It is important to note that T_c also represents the chirp duration in our model. This is a consequence of the start and stop configuration. In fact, we are sending a chirp for each radar position and thus, it is acceptable to consider the chirp duration as the slow time sampling period.

Start and Stop To model properly the Start and Stop configuration, we will remove the dependency in the radar speed v in equation 4.29 by introducing Δd, the radar distance step, as follows.

$$\Delta d = v \cdot T_c \tag{4.31}$$

Furthermore, the time of a chirp is equal to the signal sampling period times the number of samples, and thus also the slow time sampling period. This can be written as

$$T_c = M \cdot T_s. \tag{4.32}$$

Discrete version of the signal Based on the elements introduced above, we can discretise the complete version of the received signal presented in equation 4.29.

$$\begin{aligned}
S_r^{BB}[m,n] = {} & \underbrace{\exp\left[-4\pi j\left(\frac{R_x}{c}f_0 + \frac{B}{c^2T_c}R_x^2 + \frac{f_0}{c}\frac{y^2}{2R_x} - \frac{B}{c^2T_c}y^2\right)\right]}_{\text{Constant phase}} \\
& \underbrace{\cdot \exp\left[4\pi j\left(\frac{B}{cM}R_x + \frac{B}{cM}\frac{y^2}{2R_x}\right)m\right]}_{\text{Fast time dependent}} \\
& \underbrace{\cdot \exp\left[4\pi j\left(\frac{f_0}{c}\frac{y}{R_x} + 2\frac{B}{c^2T_c}y\right)(n\Delta d)\right] \cdot \exp\left[-4\pi j\left(\frac{f_0}{c} + \frac{B}{c^2T_c}\right)(n\Delta d)^2\right]}_{\text{Slow time dependent}} \\
& \underbrace{\cdot \exp\left[-4\pi j\frac{B}{cM}\frac{y}{R_x}(n\Delta d)m\right] \cdot \exp\left[4\pi j\frac{B}{cM}\frac{1}{R_x}(n\Delta d)^2 m\right]}_{\text{Slow and fast time dependent}}
\end{aligned} \tag{4.33}$$

We observe that equation 4.33 is complex in regards to the simplified model expressed in equation 4.1. Next section discusses the impact of each term in the model in order to neglect some of them and obtain the simplified equation we seek along with an acceptable range of settings.

4.6 Simplifications

In this section, we will discuss for each term the hypothesis that can be made and their impact on the model. Based on the order of magnitude presented in Table 4.1, we will identify which term can be neglected with regards to the others in order to obtain a simplified model of the form of equation 4.1 and a range of validity of each assumption. During the discussion presented below, we will keep in mind the objectives of the considered system. In fact, we will work with basic shapes and targets. Therefore, we do not have to recover shades and background details, but only binary contrasts. Simulations are performed here on a very simple image composed of three white points on a black background in order assess the validity of our assumptions. We have computed the 2D-FFT of this image and assumed that the obtained result was a perfect and complete version of the received signal. To observe the effects of the neglected terms, we have compensated the opposite of those terms to the *perfect* version of the signal obtained from the image. This way, we obtained a signal *as we had neglected those terms*.

Parameter	**Symbol**	**Order of magnitude**
Carrier frequency	f_0	$\sim 10^{10}$
Bandwidth	B	$\sim 10^{8}$
Light speed	c	$\sim 10^{8}$
Range distance	R_x	~ 10
	R_x^2	$\sim 10^{2}$
Azimuth dimension	y	~ 10
	y^2	~ 10
	y^3	$\sim 10^{2}$
Rail length	L_{rail}	$\sim 10^{-1}$
	$n\Delta d$	$\in [10^{-2} \quad 10^{-1}] \sim 10^{-1}$
	$(n\Delta d)^2$	$\sim 10^{-2}$
	$(n\Delta d)^3$	$\sim 10^{-2}$
	$(n\Delta d)^4$	$\sim 10^{-3}$
Slow time sampling	f_c	$\leq 10^{3}$

Table 4.1: Order of magnitude of setup parameters for a radar with $f_0 = 2.4$ [GHz] and $B = 500$ [MHz]. Orders have been obtained by applying some hypotheses, such as $y \sim 5$ thus if we write that $y \sim 10$, y^2 is not $\sim 10^2$.

Constant phase terms

As we are interested in frequency variations, it is acceptable to not consider constant phase terms and compensate them after processing. We observe that there are constant phase terms depending on space (R_x, y), that would be more difficult to compensate. In fact, this implies a first estimation of space coordinates to apply the effective compensation. Finally, some terms will be very small due to the $\frac{1}{c^2}$

factor, it would thus be interesting to analyse the effect of neglecting them.

$$S_r^{BB}\Big|_{\text{Constant phase}}[m,n] = \exp\underbrace{\left[-4\pi j\frac{R_x}{c}f_0\right]}_{\sim 10^3}\cdot\exp\underbrace{\left[-4\pi j\frac{B}{c^2T_c}R_x^2\right]}_{\sim 10^{-6}\cdot f_c}\cdot\exp\underbrace{\left[-2\pi j\frac{f_0}{cR_x}y^2\right]}_{\sim 10^2}\cdot\exp\underbrace{\left[-4\pi j\frac{B}{c^2T_c}y^2\right]}_{\sim 10^{-7}\cdot f_c} \tag{4.34}$$

From equation 4.34, we observe two dominant terms.

$$S_r^{BB}|_{\text{Constant phase}}[m,n] \simeq \exp\left[-4\pi j\frac{R_x}{c}f_0\right]\cdot\exp\left[-2\pi j\frac{f_0}{cR_x}y^2\right] \tag{4.35}$$

Intuitively, this equation 4.35 could be acceptable if slow time sampling frequency f_c does not exceed 1 [kHz]. We observe that the remaining terms are not independent in space, as the first is depending on R_x and the second on y. Ideally, we would like to keep only the former, but this assumption risks to have consequences on the precision of our system. We have performed several simulations to quantify the effects of this hypothesis.

1. **We consider only terms presented in equation 4.35.** We performed simulations to quantify the impact of the red terms in equation 4.36, that can be considered as "much smaller" than the others due to the $\frac{1}{c^2}$ coefficient, as presented in equation 4.34. The validity of this assumption being strongly dependent on the *slow time* sampling frequency that we will choose, we have performed simulations with different values of f_c in order to obtain a range of validity for this parameter.

$$s_r^{BB}\Big|_{\text{Constant phase}}[m,n] = \exp\left[-4\pi j\frac{R_x}{c}f_0\right]\cdot\exp\left[-4\pi j\frac{B}{c^2T_c}R_x^2\right]\cdot\exp\left[-2\pi j\frac{f_0}{cR_x}y^2\right]\cdot\exp\left[-4\pi j\frac{B}{c^2T_c}y^2\right] \tag{4.36}$$

   Simulation results are presented in Figure 4.3. We observe that the assumption has no visible impact until f_c exceeds 1 [kHz]. Then, we observe a reasonable shift of the targets for $f_c \in [10\text{kHz} \quad 100\text{kHz}]$. This induces imprecision on both range and azimuth position of the recovered targets, but stays acceptable. Finally, we observe that we lost large amount of information on the range position of targets for $f_c \geq 1$ [MHz].

   From those results, we can reasonably neglect "red terms" of equation 4.36 if we are working with a *slow time* sampling frequency f_c smaller than 10 [kHz].

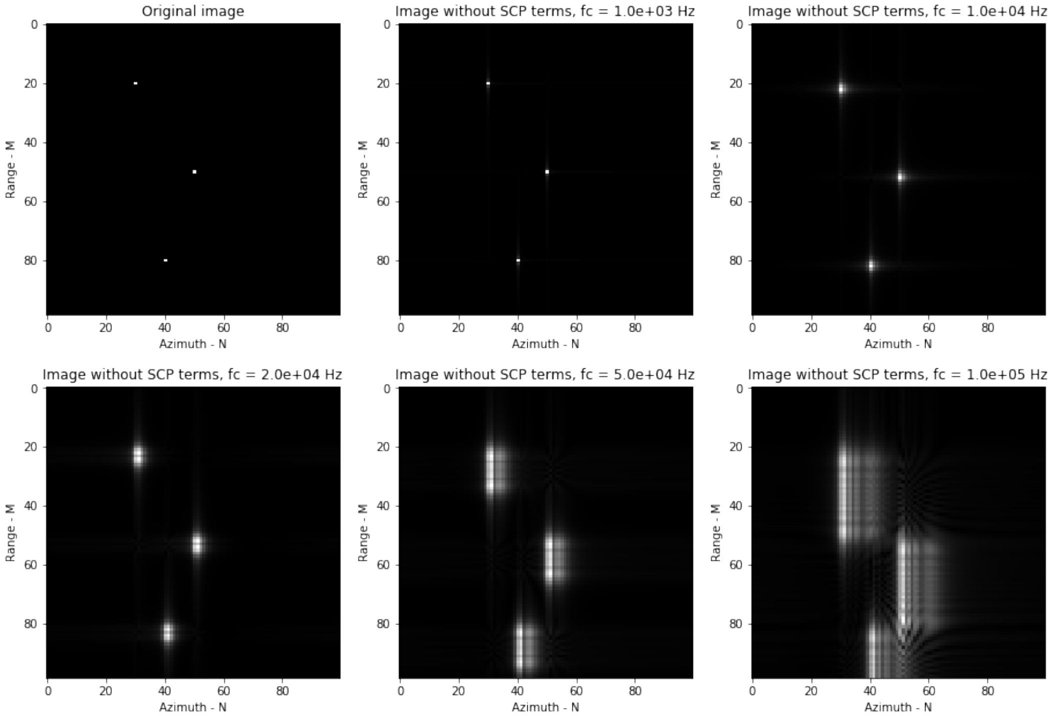

Figure 4.3: Simulation of the impact of the "Small Constant Phase" (SCP) terms on the recovered image for a *slow time* sampling period T_c varying for 10^{-4} to 10^{-6} $[s]$.

2. **We only consider the term of equation 4.35 that depends on $\mathbf{R_x}$.** The simulation will thus highlight the impact of the term depending on y, in red in equation 4.37.

$$S_r^{BB}|_{\text{Constant phase}}\,[m,n] \simeq \exp\left[-4\pi j \frac{R_x}{c} f_0\right] \cdot \exp\left[-2\pi j \frac{f_0}{cR_x} y^2\right] \qquad (4.37)$$

As the value of this term is dependent on H (through $R_x = \sqrt{H^2 + x^2}$) we have observed the evolution of its impact for different values of H. Results are presented in Figure 4.4. We observe that the recovered targets are correctly placed in range but spread in azimuth direction, with a quadratic evolution for small values of H. This is consistent with the expression of the neglected term, in 4.37. However, as the intensity of the spread targets decreases as the distance from the real target increases, we can still approximate the target positions with an appropriate high-pass filter for intensity. Figure 4.5 presents recovered targets with a filter. We observe that for a radar distance around $H = 20\,[m]$ results are acceptable.

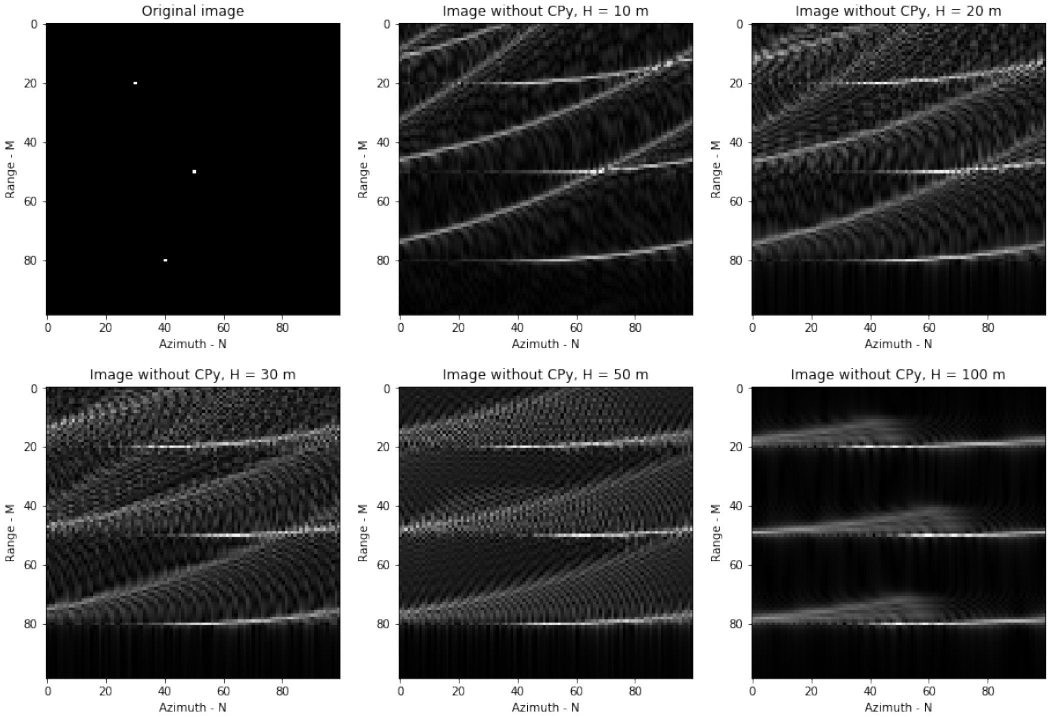

Figure 4.4: Simulation of the impact of the "Constant Phase term depending on y" (CPy) on the recovered image for H varying from $10\,[m]$ to $100\,[m]$.

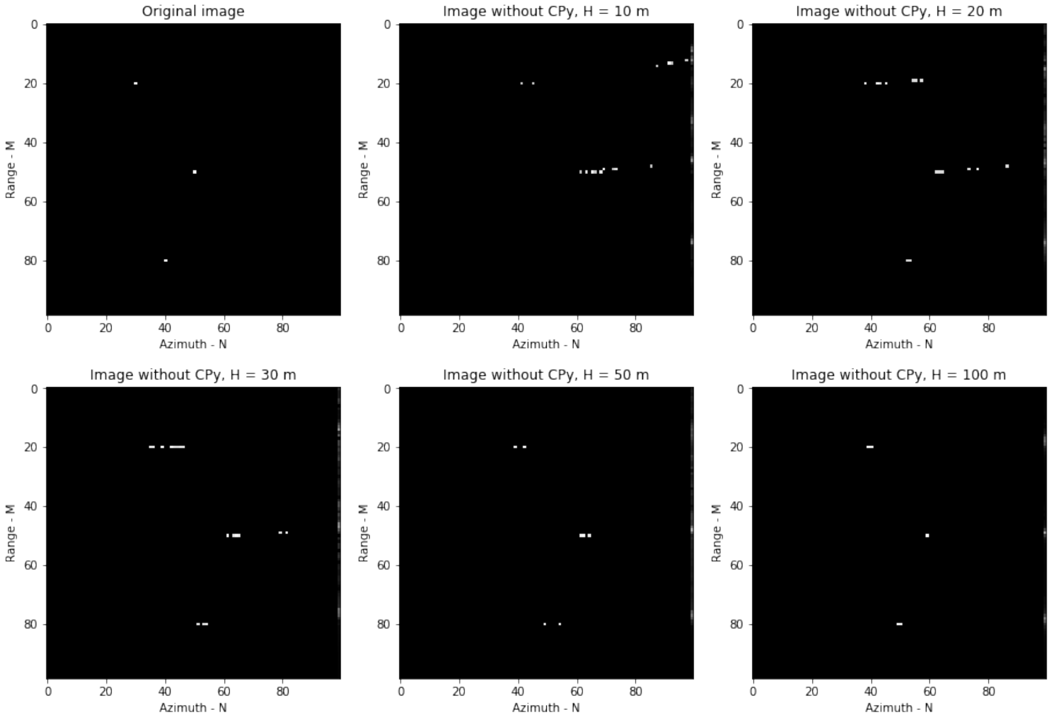

Figure 4.5: Simulation of the impact of the "Constant Phase term depending on y" (CPy) on the recovered image for H varying from $10\,[m]$ to $100\,[m]$, after a high-pass filter to identify targets.

Fast time dependent terms

In order to obtain the simplified model form presented in equation 4.1, we would like to keep only the first term of equation 4.38.

$$S_r^{BB}\Big|_{\text{Fast time dependent}}[m,n] = \exp\underbrace{\left[4\pi j\frac{B}{cM}R_x m\right]}_{\sim R_x} \cdot \exp\underbrace{\left[4\pi j\frac{B}{cM}\frac{y^2}{2R_x}m\right]}_{\sim \frac{y^2}{R_x}} \tag{4.38}$$

The magnitude order analysis presented in equation 4.38 does not allow us to neglect it without any additional condition. We observe that the validity of the simplification will strongly depend on the values of R_x and y. In fact, condition 4.39 has to be valid in order to neglect properly the R_x dependent term.

$$4\pi j\frac{B}{cM}R_x \gg 4\pi j\frac{B}{cM}\frac{y^2}{2R_x} \qquad \Leftrightarrow \qquad \sqrt{2}R_x \gg y \tag{4.39}$$

with $R_x = \sqrt{H^2 + x^2}$. We will discuss the validity of this hypothesis in section 6, about sizing. Again, we have performed simulations to observe the impact of the considered approximation.

Simulation results are presented in Figure 4.6. As we could imagine by analysing equation 4.38, we observe that recovered targets are spread in azimuth direction and become more precise as H increases. Again, we observe that once H reaches $10\,[m]$, signal amplitude is greater on the exact place of the target as if it was diffusing from the target in directions imposed by the equation. It is thus realistic to enhance recovered target position with a filter or a signal compensation.

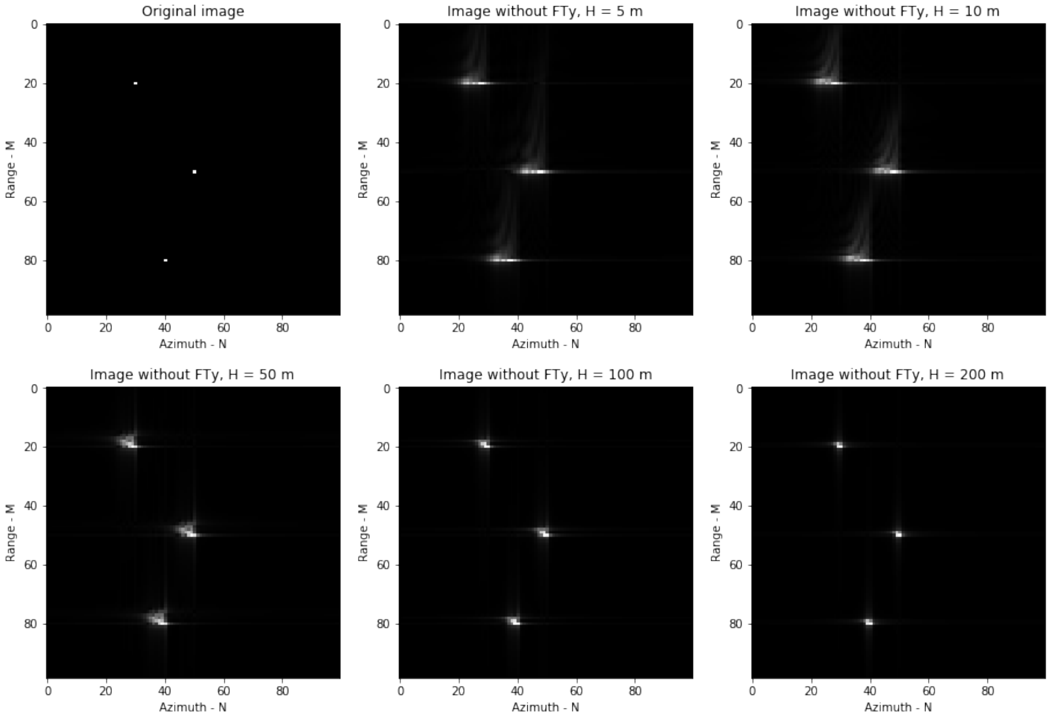

Figure 4.6: Simulation of the impact of the "Fast Time" depending term in y (FTy) on the recovered image for H value varying from $5\,[m]$ to $200\,[m]$.

Slow time dependent terms

To obtain the basic system of equations presented in 4.1, we would like to remove dependency of equation 4.40 in R_x, coloured in red to enhance readability. To achieve this, there are several possible hypotheses to apply.

$$S_r^{BB}\Big|_{\text{Slow time dependent}}[m,n] = \exp\underbrace{\left[4\pi j\frac{f_0}{cR_x}y(n\Delta d)\right]}_{\sim 10}\cdot\exp\underbrace{\left[4\pi j\frac{2B}{T_c}\frac{1}{c^2}y(n\Delta d)\right]}_{\sim 10^{-8}\cdot f_c}$$
$$\cdot\exp\underbrace{\left[-4\pi j\frac{f_0}{cR_x}(n\Delta d)^2\right]}_{\sim 10}\cdot\exp\underbrace{\left[-4\pi j\frac{B}{c^2T_c}(n\Delta d)^2\right]}_{\sim 10^{-10}\cdot f_c} \tag{4.40}$$

First, if we consider the magnitude analysis presented in equation 4.40, we can rewrite the equation as :

$$s_r^{BB}\Big|_{\text{Slow time dependent}}[m,n] \simeq \exp\left[4\pi j\frac{f_0}{cR_x}y(n\Delta d)\right]\cdot\exp\left[-2\pi j\frac{f_0}{cR_x}(n\Delta d)^2\right] \tag{4.41}$$

In a second time we will neglect the term depending on R_x only, in order to obtain a function of y as in the equation 4.1 and to avoid quadratic dependence in time. Again, this will only be valid for a range of values of f_c. Intuitively, we observe that for $f_c \leq 10$ [kHz] the approximation should stay valid, but we will confirm this with several simulations.

1. **We neglect the "small" terms, regarding the order of magnitude analysis.** Slow time dependent terms become

$$S_r^{BB}\Big|_{\text{Slow time dependent}}[m,n] \simeq \exp\left[4\pi j\frac{f_0}{cR_x}y(n\Delta d)\right]\cdot\exp\left[-2\pi j\frac{f_0}{cR_x}(n\Delta d)^2\right] \tag{4.42}$$

In simulation results presented in Figure 4.7, we observe that the impact of "small slow time-dependent" terms is a spread shift, principally in azimuth direction, that increases with f_c. The shift is much larger in azimuth direction due to terms with a y or y^2 dependency at the numerator. R_x, the range, is only at the denominator and squared most of the time, which reduces drastically its impact. Once again, we observe that the maximal acceptable value for f_c is around 100 [kHz].

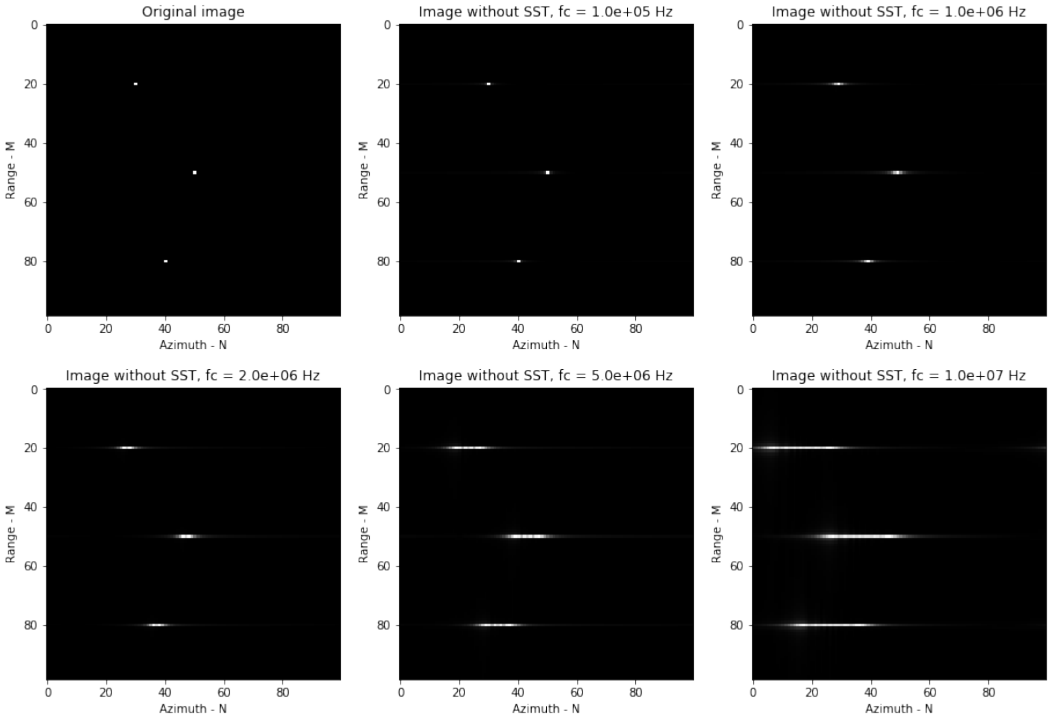

Figure 4.7: Simulation of the impact of the "Small Slow Time" depending terms (SST) on the recovered image for a slow time sampling period varying from $10^{-6}\,[s]$ to $10^{-8}\,[s]$.

2. **We neglect the term with a quadratic dependence in time.** Slow time dependent terms become

$$S_r^{BB}\Big|_{\text{Slow time dependent}}[m,n] \simeq \exp\left[4\pi j\frac{f_0}{cR_x}y(n\Delta d)\right]. \tag{4.43}$$

   Figure 4.8 presents simulation results. We observe the same form of deviation as in Figure 4.4. We can thus consider that the same kind of post-processing can be performed to recover properly the image.

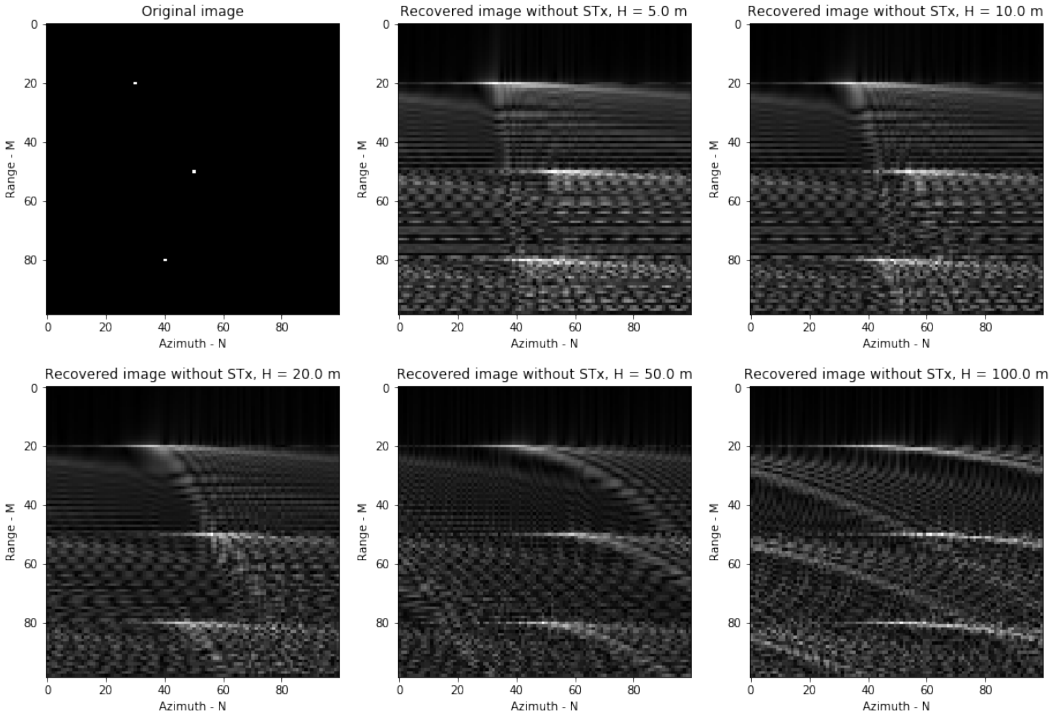

Figure 4.8: Simulation of the impact of the "Slow Time" depending term in R_x (STx) on the recovered image for H value varying from $5\,[m]$ to $200\,[m]$.

Slow and fast time dependent terms

Ideally, we would like to neglect all term in equation 4.44 in order to obtain our simplified system and to avoid non-linearity. To simplify the text, we will use the denomination *mixed terms* for *slow and fast time dependent terms.*

$$S_r^{BB}\Big|_{\text{Slow and fast time dependent}}[m,n]=\exp\underbrace{\left[-4\pi j\frac{B}{cM}\frac{y}{R_x}m(n\Delta d)\right]}_{\sim 10} \cdot \exp\underbrace{\left[2\pi j\frac{B}{cM}\frac{1}{R_x}m(n\Delta d)^2\right]}_{\sim 10^{-3}} \tag{4.44}$$

We have performed several simulations : first neglecting only one term at a time (Figures 4.10 and 4.9), then with both terms neglected (Figure 4.11). The main observation from those results is that both mixed terms are compensating each other, which means that we will obtain better results by neglecting either both or none of them, not only one at a time.

1. **We neglect the smallest mixed term.** We observe on Figure 4.9 that for small values of H, the azimuth influence on the result is much more important than the range influence. With x increasing, the impact of y becomes relatively less important and we observe a 'diagonal' spread of the recovered targets.

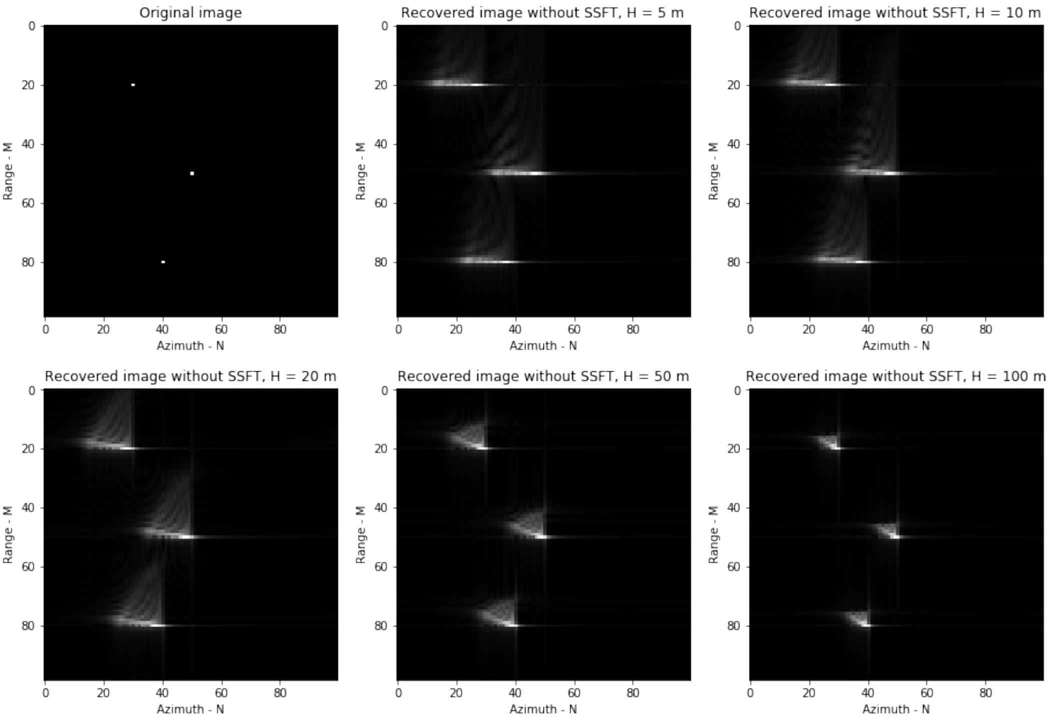

Figure 4.9: Simulation of the impact of the "Small Slow and Fast Time" dependent term (SSFT) on the recovered image for a height H varying from $5\,[m]$ to $100\,[m]$.

2. **We neglect the largest mixed term.** By neglecting the largest mixed term, we observe the same phenomena as for the smallest one, but in the other direction. This is consistent with the equations as both terms are opposed in sign.

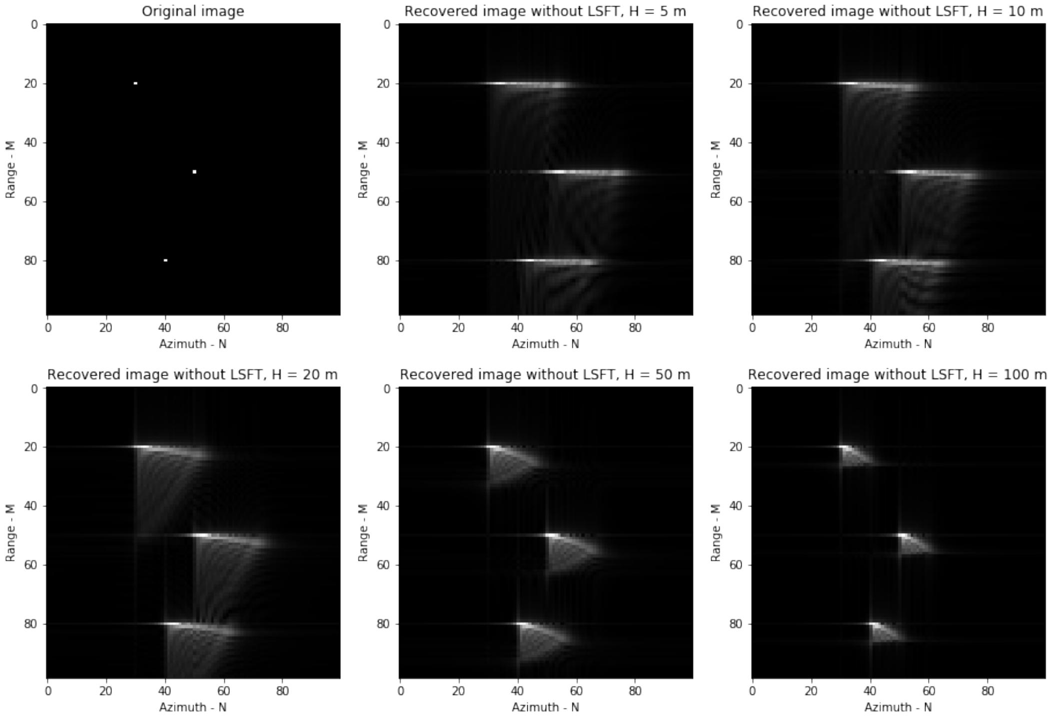

Figure 4.10: Simulation of the impact of the "Large Slow and Fast Time" dependent term (LSFT) on the recovered image for H value varying from $5\,[m]$ to $100\,[m]$.

3. **We neglect both mixed terms.** Figure 4.11 presents the obtained results when both mixed terms are neglected. As explained above, we observe a more precise recovery of the targets because of the sign of each term. In fact, they are partially compensating each other. Hence we can neglect both of them without loss of precision.

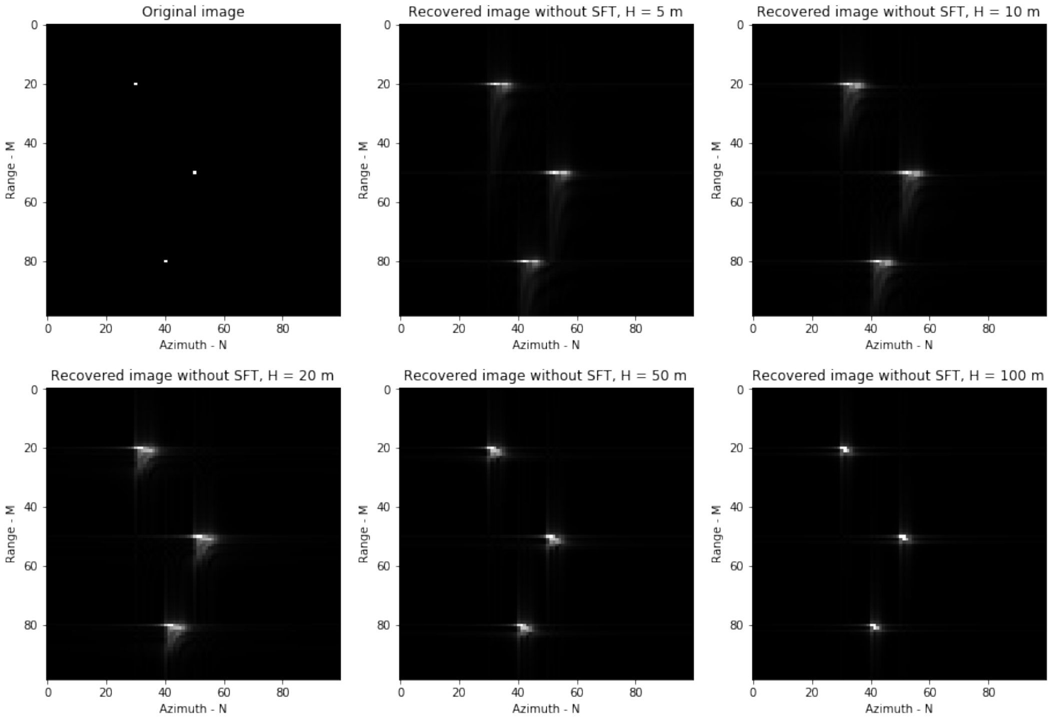

Figure 4.11: Simulation of the impact of both "Slow and Fast Time" dependent terms (SFT) on the recovered image for a H value varying from $5\,[m]$ to $100\,[m]$.

4.7 Model summary

Based on the order of magnitude analysis and on the simulations performed above, we can neglect most of terms in equation 4.33 and obtain a first simplified version of the model.

$$S_r^{BB}\left[m,n\right] = \underbrace{\exp\left[-4\pi j\left(\frac{R_x}{c}f_0\right)\right]}_{\text{Constant phase}} \cdot \underbrace{\exp\left[4\pi j\frac{B}{cM}R_x m\right]}_{\text{Fast time dependent}} \cdot \underbrace{\exp\left[4\pi j\frac{f_0}{c}\frac{y}{R_x}(n\Delta d)\right]}_{\text{Slow time dependent}} \tag{4.45}$$

In equation 4.45, we have neglected very small order terms, constant phase term depending on y, fast time dependent term depending on y and slow time dependent terms depending on R_x only. Furthermore, we have neglected “mixed terms” after having observed that they were compensating each other. The range of validity of those assumptions in described in table 4.2.

Parameter	**Condition**
Slow time sampling frequency	$f_c \leq 10$ [kHz]
Distance between the radar and the target R_x	$R_x \gg \frac{y}{\sqrt{2}}$
Distance between the radar and the target in $\hat{x}$ direction	$x \gg 20$ $[m]$

Table 4.2: Overview of the range validity of the simplified model expressed in equation 4.45. It is important to note that R_x can be influenced either by H or x. Simulations have been performed and commented for H, but this can also be applied to x.

Furthermore, we can express the received signal without considering the constant phase term and compensate it after processing. We will thus write

$$S_r^{BB}[m,n] \overset{\psi}{\simeq} \underbrace{\exp\left[4\pi j \frac{B}{cM} R_x m\right]}_{\text{Fast time dependent}} \cdot \underbrace{\exp\left[4\pi j \frac{f_0}{c} \frac{y}{R_x} (n\Delta d)\right]}_{\text{Slow time dependent}}, \tag{4.46}$$

with the $\overset{\psi}{\simeq}$ symbol meaning "equals up to a constant phase shift". Finally, to obtain the simplified model, we decorrelate expression 4.46 in space. To do so, we consider the fact that the radar waves are spread in the environment along the angle of aperture θ of the radar. Based on Figure 4.12 that represents this phenomena, we perform the following change of variable.

$$\sin\theta = \frac{y}{R_x}, \tag{4.47}$$

with θ the aperture angle of the radar in azimuth direction.

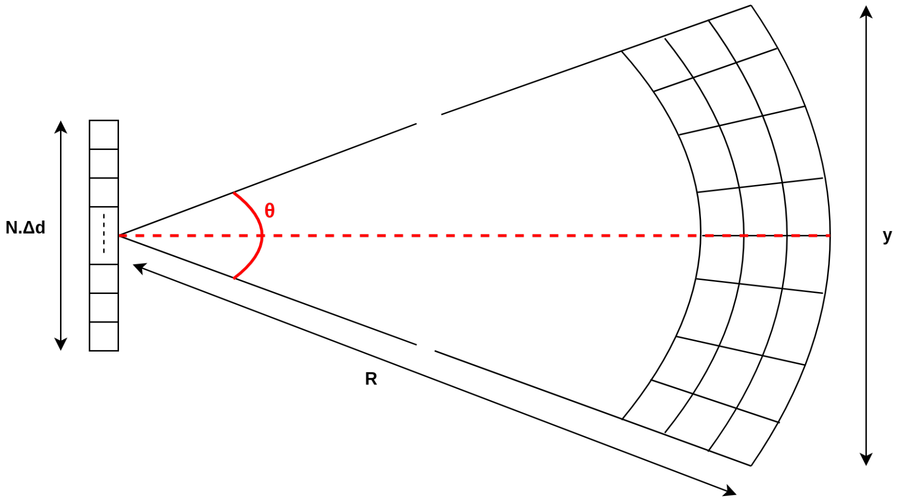

Figure 4.12: Representation of the aperture of the radar and its "polar vision" with the adequate parameters.

Equation 4.46 can thus be transformed as follows, in order to obtain the final simplified model that we will use for the rest of the developments.

$$S_r^{BB}\left[m,n\right] \overset{\psi}{\simeq} \underbrace{\exp\left[4\pi j\frac{B}{cM}R_x m\right]}_{\text{Fast time dependent}} \cdot \underbrace{\exp\left[4\pi j\frac{f_0}{c}\sin(\theta)(n\Delta d)\right]}_{\text{Slow time dependent}} \tag{4.48}$$

Thanks to the change of variable and the hypothesis expressed in Table 4.2, we have derived a simplified model of the form expressed in 4.1.

Chapter 5

Image processing algorithms

In this chapter, the two algorithms that we have used to recover our images from the received signals are presented : the *Fast Fourier Transform* algorithm and the *Matching Pursuit* algorithm. Advantages and drawbacks will be presented and illustrated using simulation of for both algorithms.

5.1 Notations

Fast Fourier Transform	FFT
Number of samples in range direction (fast time sampling)	M
Number of samples in azimuth direction (slow time sampling)	N
Duration of a chirp	T_c
Received signal after coherent demodulation (in base band)	S_r^{BB}
Range position of a target	R
Angle position of a target	θ
Range resolution	ΔR
Angular resolution	$\Delta\theta$
Fast time zero padding coefficient	P_m
Slow time zero padding coefficient	P_n
Bandwidth	B
Wavelength	λ
Distance between each sweep	Δd
Matching pursuit threshold	ρ
Macthing pursuit maximum number of iteration	s

5.2 Fourier Transform Algorithm

In this section, the algorithm based on the Fourier Transform is presented and simulated. The main steps of this algorithm are :

1. **IN :** The input signal is the 2D-matrix of size $M \times N$ that contains the signal received after coherent demodulation and sampling, S_r^{BB}.
2. **2D-FFT :** We apply the $2D - FFT$ algorithm provided by the function *fft2* from *numpy* (python) to the received signal.
3. **OUT :** The output signal is a 2D-matrix of size $(P_m \cdot M \times P_n \cdot N)$, where P_m and P_n are the zero padding coefficient in the m and n sampling axis respectively (they will be explained later).

After having applied this algorithm, we have to map the result to the real dimensions using the spatial resolutions of the signal. In fact, each sample in range dimension corresponds to $\Delta R\ [m]$ and each sample in azimuth dimension corresponds to $\Delta\theta$ °.
Additional steps can be performed on the data in order to enhance the result quality, such as *padding* or *Hamming window.* This will be discussed in this section.

5.2.1 Principle of the Fourier Transform

To recover an image from the received data, we use the simplified model developed in section 4. This model presents the demodulated received signal as the product of two exponential functions, the first depending on (R, M) and the second depending on (θ, N). In the Fourier domain, we can thus assume that the frequency of the signal in the fast temporal domain (M) gives information about the range, while the frequency of the signal in the slow temporal domain (N) gives information about the angle at which the target is located.
This simplified model of the received signal for a single point target at position (R_x, θ) with an amplitude $A = 1$ can be rewritten from Equation 4.48:

$$S_r^{BB}[m,n] \overset{\psi}{\simeq} \exp\left[4\pi j\left(\frac{B}{cM}R_x m\right)\right] \cdot \exp\left[4\pi j\left(\frac{\sin(\theta)n\Delta d}{\lambda}\right)\right]. \tag{5.1}$$

The numbers of samples taken for this signal are M and N in range and angle direction respectively. This means that the signal is defined only in a window of size M and N in their respective direction :

$$S_r^{BB}[:,n] \Rightarrow \mathrm{rect}\left[\frac{m}{M}\right] S_r^{BB}[:,n] \tag{5.2}$$

and

$$S_r^{BB}[m,:] \Rightarrow \mathrm{rect}\left[\frac{n}{M}\right] S_r^{BB}[m,:], \tag{5.3}$$

with rect a rectangular windows define by :

$$\operatorname{rect}\left(\frac{t}{T}\right) = \begin{cases} 1 & \text{if } t < T. \\ 0 & \text{elsewhere.} \end{cases} \tag{5.4}$$

The algorithm consists in applying a 2D-FFT on the matrix of received signals S_r^{BB} to extract the range and angle profile of the target. The 2D-FFT is defined as follows [25] :

$$F(u,v) = \sum_{m=\infty}^{\infty} \sum_{n=-\infty}^{\infty} f(m,n) \exp^{-j2\pi(um+vn)}, \tag{5.5}$$

where u and v are the spatial frequencies in x and y direction respectively. The Fourier transform gives a complex signal :

$$F(u,v) = F_R(u,v) + jF_I(u,v). \tag{5.6}$$

However, in our application we only look at the amplitude of the Fourier Transform. In fact, we only want to recover the position of the target which corresponds to a peak in the amplitude of the module of the FFT :

$$A(FT) = \|F(u,v)\| = \sqrt{F_R^2(u,v) + F_I^2(u,v)}. \tag{5.7}$$

Then we will now consider that the result of the Fourier Transform is the module of this one. Applying the 2D-FFT from Equation 5.5 to 5.1 gives us :

$$\begin{aligned} F\left[f_R, f_\theta\right] = &\sum_{m=\infty}^{\infty} \sum_{n=-\infty}^{\infty} \underbrace{\operatorname{rect}\left[\frac{n}{N}\right] \operatorname{rect}\left[\frac{m}{M}\right] \exp\left[4\pi j \left(\frac{mB}{cM} R_x\right)\right] \exp\left[4\pi j \left(\frac{n\Delta d}{\lambda} \sin\theta\right)\right]}_{\text{signal}} \\ &\cdot \exp\left[-j2\pi\left(\frac{f_R m}{M} + \frac{f_\theta n}{N}\right)\right]. \end{aligned} \tag{5.8}$$

The terms f_R and f_θ are the spatial frequencies of the FFT and they can be chosen such that the frequency found by the Fourier Transform corresponds to R_x and $\sin\theta$. Due to the rectangular windows, we can modify the expression by changing the boundaries of the two sums from 0 to $M-1$ and 0 to $N-1$ respectively. However, we will keep the two rectangular windows in the equations in order to facilitate the understanding of the following development.

$$\begin{aligned} F\left[f_R, f_\theta\right] = &\sum_{m=0}^{M-1} \sum_{n=0}^{N-1} \operatorname{rect}\left[\frac{m}{M}\right] \operatorname{rect}\left[\frac{n}{N}\right] \exp\left[4\pi j \left(\frac{mB}{cM} R_x\right)\right] \exp\left[4\pi j \left(\frac{n\Delta d}{\lambda} \sin\theta\right)\right] \\ &\cdot \exp\left[-j2\pi\left(\frac{f_R m}{M} + \frac{f_\theta n}{N}\right)\right]. \end{aligned} \tag{5.9}$$

Because one exponential term of the signal S_r^{BB} depends of m and the other of n, we can separate the two sums and obtain :

$$\begin{aligned} F(f_R, f_\theta) =& \sum_{m=0}^{M} \operatorname{rect}\left[\frac{m}{M}\right] \exp\left[4\pi j \frac{B}{c} m R_x\right] \exp\left[-j2\pi \frac{f_R m}{M}\right] \\ & \cdot \sum_{n=0}^{N} \operatorname{rect}\left[\frac{n}{N}\right] \exp\left[4\pi j \frac{n\Delta d \sin(\theta)}{\lambda}\right] \exp\left[-j2\pi \frac{f_\theta n}{N}\right]. \end{aligned} \tag{5.10}$$

Before going further we have to remember that the Fourier Transform of a rectangular window gives a sinc function :

$$FT\left[\operatorname{rect}\left(\frac{t}{T}\right)\right] = T\operatorname{sinc}\left(Tf\right). \tag{5.11}$$

where f is the frequency and $\operatorname{sinc}(f) = \frac{\sin(f)}{f}$.
Then we use the *convolution theorem.* It says that the Fourier Transform of a product is equivalent to the convolution of the two Fourier Transforms [26] :

$$FT\left(x(t) \cdot y(t)\right) = X(\omega) * Y(\omega). \tag{5.12}$$

Applying the FFT on Equation 5.10 corresponds to the FFT of a product. It is thus equivalent to the convolution of the FFTs of each function : the one in the m dimension and the other in the n dimension. Because each of those FFTs are the product between a rectangular window and the exponential term in the corresponding dimension, we can use once again the properties of Equation 5.12 and write :

$$F\left[f_r, f_\theta\right] = \left[M\operatorname{sinc}(Mm) * F(f_R)\right] * \left[N\operatorname{sinc}(Nn) * F(f_\theta)\right]. \tag{5.13}$$

with $F(f_R)$ and $F(f_\theta)$ the FFT in the range (m) and angle (n) dimension respectively. This means that the Fourier transform $F(f_R)$ and $F(f_\theta)$ result in deltas located at frequencies f_R and f_θ. Those frequencies correspond to the range and angular position of the target, respectively. The Fourier Transform algorithm results thus in a collection of deltas convoluted by a cardinal sine function such that a target at position (R_i, θ_j) corresponds to the intersection of two cardinal sine functions in range and angular dimension (see the simulations below). The amplitude of the main peak determines the amount of power reflected by this target.

5.2.2 Simulation of the Algorithm

In this section, we analyse the consequences of the temporal limitation of the received signal by performing simulations of the Fourier Transform algorithm.

The Figure 5.1 shows the expected result of the Fourier Transform for a target situated at position $(R = 18\,[m]\,, \theta = 0°)$. We observe that the target is recovered as the intersection of two cardinal sine functions.

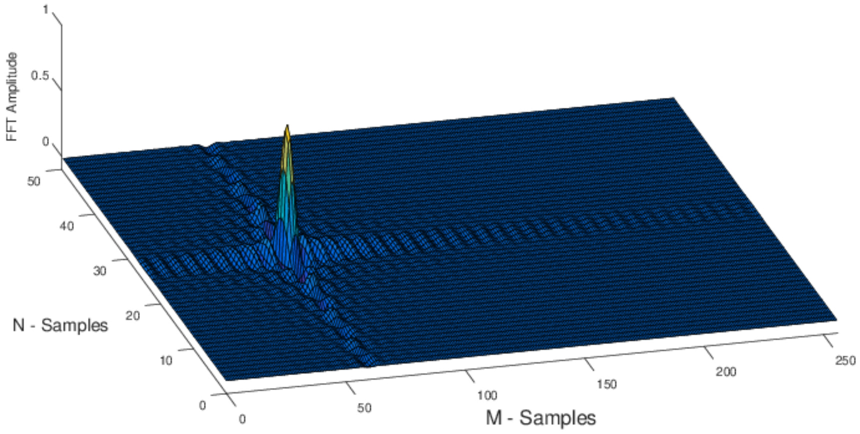

Figure 5.1: Example of the result of the FFT algorithm : we see that the intersection of the two sinc leads to a main peak in the position of the simulated target (here m = 60 $\Rightarrow R = 60\Delta R = 18$ m and n = 25 $\Rightarrow \theta = 0°$

When the number of targets is really low (remember that a potential target can take place every $(\Delta R, \Delta\theta)$), this convolution effect is not really annoying but when we have a larger number of reflected waves coming from multiple targets, each of them leads to two cardinal sine functions in the image (in range and angle direction) that can reduce their visibility. The Figure 5.2 simulates the expected result of the Fourier Transform Algorithm for 15 targets with random positions. We see how the modulation by the cardinal sine functions degrades the quality of the image.

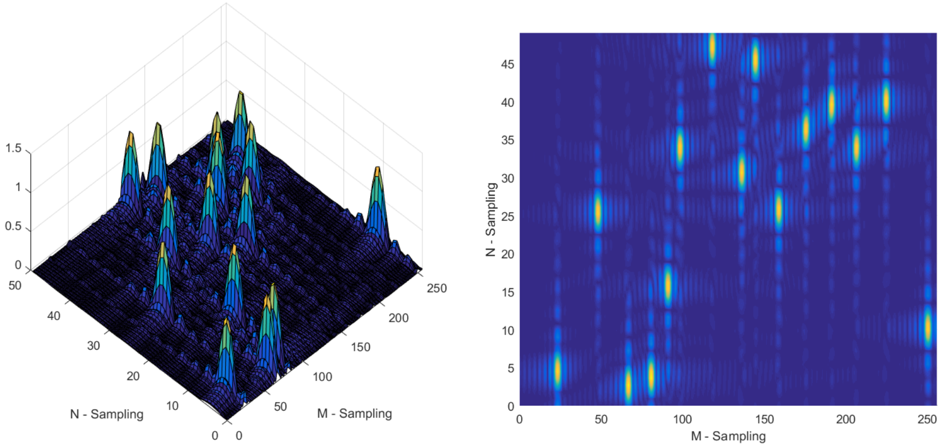

Figure 5.2: FFT-Algorithm applied to a collections of 15 random targets with the same amplitude. On the left, a 3D view of the multiple sinc peaks that occur at the position of each target. On the right, a top view of the image recovered : we see that the secondary lobes of the sinc can add constructively, leading to a kind of parasitic effect in the image and then decreasing is quality

There are multiple ways to increase the resolution and then the quality of the FFT in order to obtain a better image at the end. Three methods are investigated here : *Hamming windowing*, increasing the number of acquisitions and *zero-padding*.

Hamming windowing : It is possible to reduce the amplitude of the secondary lobes by performing a convolution of the image with an Hamming window (the convolution of the image is equivalent to a multiplication of the signal before applying the FFT due to the convolution theorem of the Fourier Transform so it's a simple operation in the algorithm). As a reminder, the Hamming window is defined as follows [27] :

$$h(t) = \begin{cases} 0.42 - 0.5\cos\left(2\pi\frac{t}{T}\right) + 0.08\cos\left(4\pi\frac{t}{T}\right) & \text{if } t \in [0, T]. \\ 0 & \text{elsewhere.} \end{cases} \tag{5.14}$$

Figure 5.3 shows the result of the convolution by a Hamming window. We see that the secondary lobes have decreased but the main lobe is now wider. This effect is a consequence of the Hamming windowing and thus applying it must be done carefully if the targets are close to each others. In fact, the windowing risks to produce an overlapping of the lobes, reducing the quality of the recovered image.

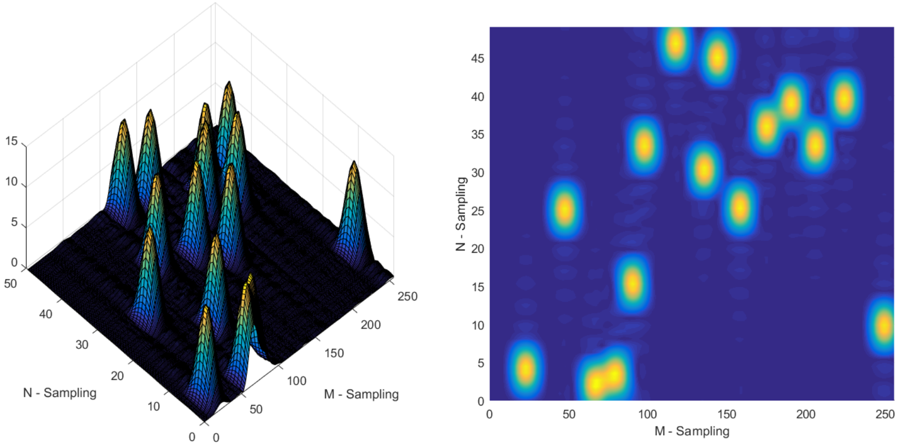

Figure 5.3: Image of the FFT-Algorithm for 15 randomly generated targets after 2D-convolution with a Hamming window. The size of the windows are 10 in the N-direction and 30 in the M-direction.

Increasing the number of acquisitions : Another way to increase the resolution of the FFT algorithm (making the main lobe thinner) is to increase the numbers of samples M and N. Indeed we saw in Equation 5.11 that the FFT applied to a rectangular window (defining the 'time restrictive' aspect of our signal) leads to cardinal sine functions with higher frequency if the acquisition time T is larger. This increase in the sinc frequency means that the main lobe will be thinner and thus increases the resolution of the recovered image. Figure 5.4 shows this effect for a simple signal : when the number of acquisition is larger (for the same sampling frequency), the peak resulting from the FFT performed on the signal is way thinner.

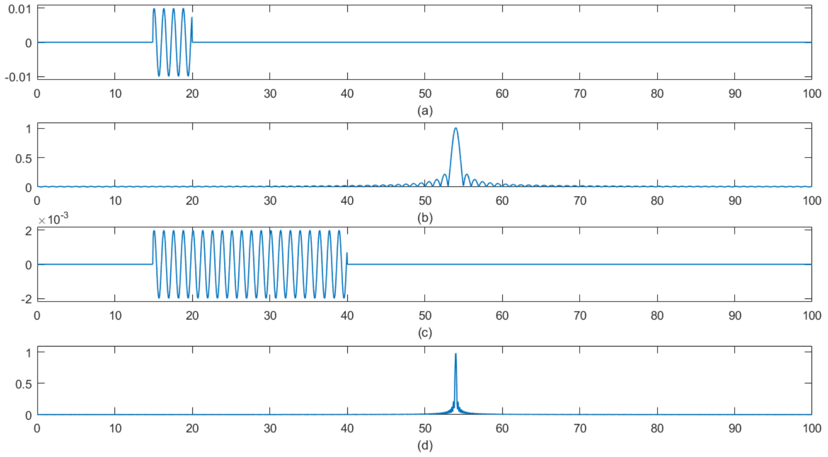

Figure 5.4: Impact of the number of samples on the resolution of the recovered signal. The simulated signal is a single frequency signal of type $\sin(wn)$. In (a) the signal is acquired with a small number of samples and the resulting FFT is in (b). In (c) the number of acquired samples is 4 times bigger and the FFT peak is then thinner (d).

Zero-padding : If we look at Equation 5.5 we observe that the Fourier Transform is a scalar product between the signal (S_r^{BB}) and a collection of mono frequency signals $\exp^{-j2\pi\left(\frac{f_R m}{M}+\frac{f_\theta n}{N}\right)}$. However the discrete aspect of the Fourier Transform means that we only perform this scalar product with a limited number of frequencies and this implies a resolution in the frequency domain, such that two frequencies too close to each other cannot be differentiated.

By definition, the DFT (Discrete Fourier Transform) looks for frequencies between $\frac{-f_s}{2}$ and $\frac{f_s}{2}$ with f_s the sampling frequency. The frequency resolution for a given f_s and a number of sample M is :

$$\delta f = \frac{f_s}{M}. \tag{5.15}$$

This condition can be problematic when the number of samples is low but it is possible to simulate a larger number of samples using the technique of *zero-padding*. The *zero-padding* consists in adding P_m zeros at the end of the signal in order to enhance the DFT resolution. We have

$$\delta_f = \frac{f_s}{P_m \cdot M}. \tag{5.16}$$

This technique will be often used in our applications of the *Fourier Transform* algorithm in order to ensure a sufficient resolution of the FFT. However, because the number of samples is increased, the computational cost will be increased too.

5.2.3 Discussion

We have seen that the FFT-algorithm can lead to multiple drawbacks. First we make the assumption that the signal is of the form 4.1, which is not completely true. Then we process a finite number of samples which involves several effects such as the modulation of deltas by cardinal sine functions and the limited frequency resolution.
However those effects can be limited by increasing the number of acquired samples, applying zero-padding or using a Hamming window. Those techniques are performed in the measurements presented is chapter 7.

5.3 Matching Pursuit algorithm (for Sparse Signals)

The Fourier Transform algorithm allows us to reconstruct the image with a sufficient quality and in a reasonable time, but it often leads to stained images due to the presence of ripples or when the simplified signal is not valid. In this section, we will see that in some specific cases, we can reconstruct the image without using the Fourier Transform and with a better quality at the end. To do so, we use an algorithm called the *Matching Pursuit*, which allows us to reconstruct the image as a combination of multiple " sub-images" from a data base called the *dictionary*. However to ensure that this algorithm works correctly we must work with sparse signals. Sparsity principle will be explained in section 5.3.1.

The most important steps of the Matching Pursuit algorithm are:

1. **IN**: The input data is the received signal which is a matrix of size $M \times N$.
2. **Creating the dictionaries**: We first create two dictionaries : one for the signal (INPUT) and the other to map each element of the signal dictionary to an element of the image dictionary (OUTPUT). The two dictionary have size $M \cdot N \times M \times N$.
3. **Applying the Matching Pursuit**: We perform the scalar product between our signal dictionary and the received signal. We keep the result in a vector r_{cov}. Then we enter the loop of the algorithm and we keep the K biggest coefficients into a list $coeff$ (K depends on the threshold and the maximum number of iteration used in the algorithm).
4. **Creating the image**: We take the K elements in the image dictionary corresponding to the biggest coefficients.

5. **OUT**: The output is a matrix of size $M \times N$ corresponding to the recovered image. We plot itusing *imshow* and *pcolor* functions from python.

5.3.1 The Sparsity Principle

The sparsity principle supposes that a signal can be expressed using another signal from a known basis. In the case of a 2D signal such the one we use in our application , this principle can be defined as follows [28].
We denote X a 2D-signal ($X \in \mathbb{R}^{M \times N}$) and we suppose that this signal can be decomposed in a *sparsity basis* $\mathbf{\Psi}$ using some non-zero elements α :

$$X(\xi) = \sum_{k=1}^{D} \alpha_k \Psi_k(\xi), \quad \text{with } \xi = (m,n) \quad \mathbf{\Psi} = \{\Psi_j : 1 \leq j \leq D\}.$$

The basis $\mathbf{\Psi}$ is usually an orthonormal basis (e.g. the Fourier basis) from which we take a combination of elements Ψ_k to reconstruct X. The coefficient α_k comes from a vector $\alpha \in \mathbb{R}^D$ such that if the signal X is not similar to the signal Ψ_k from the basis $\mathbf{\Psi}$, then the corresponding coefficient α_k is 0.
The Matching Pursuit is an algorithm based on this sparsity assumption that finds which are the element Ψ_k from $\mathbf{\Psi}$ with the biggest coefficient α_k to reconstruct an estimation of the signal : $\hat{X}$.

5.3.2 The Matching Pursuit Algorithm

The Matching Pursuit aims at finding the s biggest coefficient α_k linked to a element of the signal dictionary Ψ_k that corresponds to an equivalent image I_k in the dictionary of images $\boldsymbol{I}$.
The algorithm is based on the following condition [29] :

$$\alpha = \underbrace{\text{argmin}}_{\alpha'} \frac{1}{2} \|X - \mathbf{\Psi}\alpha'\|^2 \text{ s.t. } \|\alpha'\|_0 \leq s. \tag{5.17}$$

Equation 5.17 shows that the Matching Pursuit try to minimize the distance between X and $\mathbf{\Psi}\alpha = \hat{X}$ such that the number of elements from $\mathbf{\Psi}$ used to approximate X is less than a certain number s (which mean than the number of non-zero element in the vector α i.e. $\|\alpha\|_0 \leq s$).

Based on this criterion, the algorithm performs a greedy solution as follow :

Initialization:

$$r^{(0)} = X, \alpha^{(0)} = 0 \in \mathbb{R}^D, k = 0. \tag{5.18}$$

Loop:

$$i^* = \underbrace{\text{argmax}}_{1\leq i\leq D}\left|\langle \Psi_i, r^{(k)}\rangle\right|. \tag{5.19}$$

$$\alpha^{(k+1)} = \alpha^{(k)} + \underbrace{\langle \Psi_{i^*}, r^{(k)}\rangle e_{i^*}}_{\alpha^{(i^*)}}. \tag{5.20}$$

$$r^{(k+1)} = X - \boldsymbol{\Psi\alpha^{(k+1)}}. \tag{5.21}$$

$$k \leftarrow k+1. \tag{5.22}$$

When k = s, the loop stops and we have $\hat{X} = \boldsymbol{\Psi}\alpha^{(s)}$. The condition on $\|\alpha\|_0$ supposes that we know how many elements of $\boldsymbol{\Psi}$ are in X, which means that we know how many targets there are in the image. Usually, we don't have this information. In order to not be limited by only this constraint we add another constraint that stops the loop when the value of the coefficient α(k) (we suppose that we have normalized the signal) is below a certain threshold ρ. Then the image will only be composed of the targets that reflect to most power.

5.3.3 A small example

In order to illustrate the algorithm, we present here a simple example on 1-D signals : We suppose that the signal X is sparse in a basis $\boldsymbol{\Psi}$ (the dictionary) which is made of cosine with different frequencies. A possible dictionary is $\boldsymbol{\Psi} = \{\Psi_1 = cos(wt), \Psi_2 = cos(2wt), \Psi_3 = cos(3wt)\}$ for example. We assume that the signal is made of a linear combination of element from this dictionary :

$$X = \alpha_1\Psi_1 + \alpha_2\Psi_2 + \alpha_3\Psi_3. \tag{5.23}$$

with here : $\alpha_1 = 1, \alpha_2 = 0.25$ and $\alpha_3 = 0.5$. The Figure 5.5 shows the dictionary and the signal defined previously.

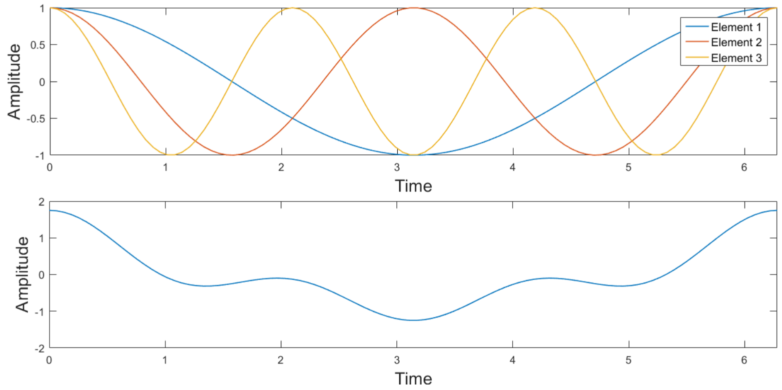

Figure 5.5: Representation of the dictionary $\mathbf{\Psi}$ (top) and the signal X made of a combination of elements from $\mathbf{\Psi}$ (bottom).

The idea is to recover the signal X from elements of $\mathbf{\Psi}$ by performing the Matching pursuit algorithm : we compute the inner product between X and Ψ_1, Ψ_2 and Ψ_3 successively and we keep the one who gives the highest result (the highest inner product). This result becomes the first coefficient α to keep. We then subtract the corresponding element of the dictionary with an amplitude proportional to the coefficient from the *residual* and we loop again. The results are shown in Figure 5.6. We see that at each steps, we get closer to the original signal.

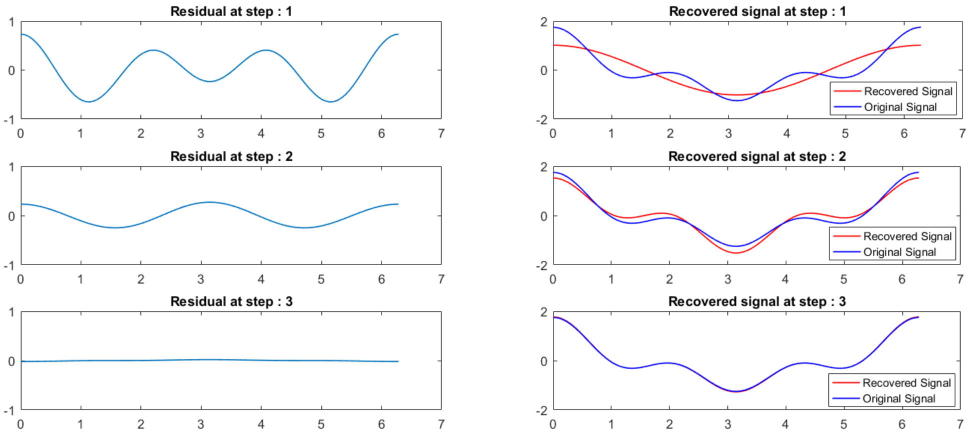

Figure 5.6: Results of the Matched Pursuit algorithm for the simple example : we see that the residual becomes smaller and smaller at each step (left) and that the recovered signal becomes closer to the original signal at each step (right).

5.3.4 Dictionary of our SAR application

In our SAR application, the signal X from the definition of the sparsity principle is the received signal after coherent demodulation and calibration, thus : $X \Rightarrow S_r^{BB}$.

We know that a potential target can be detected if it is in the range $[0, R_{max}; -\theta_{max}/2, \theta_{max}/2]$ where R_{max} and θ_{max} are the maximum possible range and angle at which a target can be detected, respectively. So the basis that we will use contains all the signals that we may receive for a punctual target at each position $(R_i, \theta_j) \in [0, R_{max}; -\theta_{max}/2, \theta_{max}/2]$. For each potential target, we then define $S^{ij} \in \mathbb{R}^{M \times N}$, creating a dictionary containing $M \cdot N$ elements of size $M \times N$.

Each signal in the dictionary $\boldsymbol{\Psi}$ have an equivalent image in an other dictionary $\boldsymbol{I}$ such that $\Psi^{ij} \Rightarrow I^{ij}$ where I^{ij} is the image of a scatter point at position (R_i, θ_j). We see that the size of the dictionaries is important and the computational cost becomes huge if the numbers of samples M and N increase. This is one of the limitation of the Matching Pursuit. However, once the dictionary is created it does not need to be computed again, whatever the observed scene as long as we do not modify any intrinsic parameter of the system $(BW, M, N, ...)$.
When the dictionaries are created, we can perform the Matching Pursuit algorithm to recover our image.

5.3.5 Simulation of the Algorithm

We first create our signal from Equation 4.25 : we know that at time m the frequency of the radar will be $f_m = f_c - \frac{BW}{2} + \frac{BW}{M} m$ and the delay τ for a target at position (R_i, θ_j) when the radar position is n is $\tau_{ijn} = \frac{2R'_{ijn}}{c}$ with :

$$R'_{ijn} = \sqrt{R_i \cos(\theta_j) + (R_i \sin(\theta_j) - n\Delta d)^2}. \tag{5.24}$$

with Δd the distance between each sweep of the radar on the rail. Then the value of the signal simulated for a targets $\{ij\}$ for the sample m and n will be :

$$S_{ijmn} = A_{ij} \exp\left[(j2\pi f_m \tau_{ijn})\right] \tag{5.25}$$

with A_{ij} the amplitude reflected by the target $\{ij\}$. The elements of the dictionary corresponding to the image must be chosen such that the recovered image fits the expected image. A possible dictionary is composed of the punctual points at the positions described below :

$$I_{ijmn} = \begin{cases} 1 & \text{if } mn = ij \\ 0 & \text{elsewhere} \end{cases} = \delta_{im} \cdot \delta_{jn}. \tag{5.26}$$

with δ_{kl} the Kronecker delta which is 1 if $k = l$ and 0 elsewhere..
The Figure 5.7 shows the original image that we would like to recover. If we apply the Fourier Transform algorithm with the signal corresponding to this image, we get the result shown in Figure 5.8. We see that the image is quite degraded even if we can still read the word from the original image.

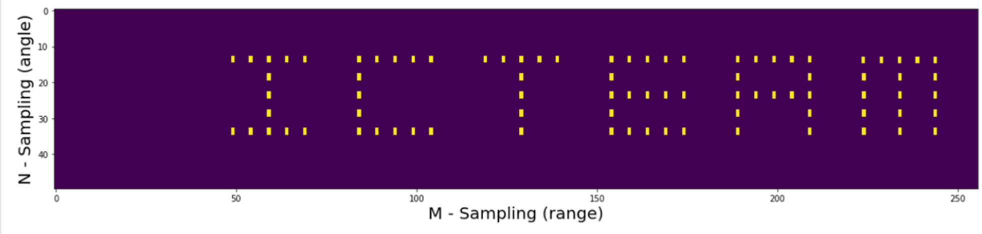

Figure 5.7: Original image made of simple point targets placed to form the word "*ICTEAM*".

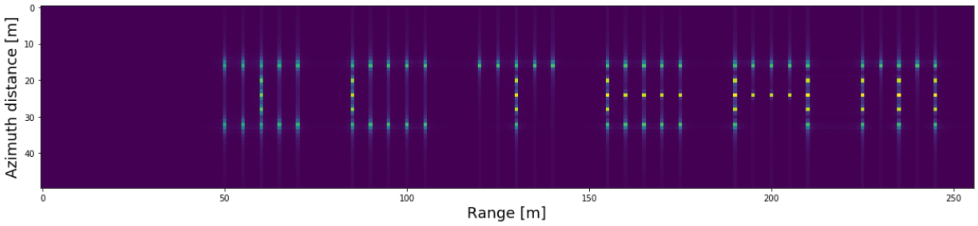

Figure 5.8: Recovered Image using the Fourier Transform Algorithm.

The Figure 5.9 shows the result obtained with the Matched Pursuit algorithm. We see that the recovered image is more faithful to the original. It can be interesting to see the profile of the coefficient values on Figure 5.3.5 : the dictionary is made such that the element indices are defined by : $k = N \cdot i + j$ with i the indices of the range (going from 0 to 255) and j the indices of the angle (going from $-15°$ to $15°$). Then we can see that the peak corresponding to a coefficient of the same letter are close to each other. If we zoom on this "peak region", we observe that for each peak corresponding to a match (when an signal from the dictionary match the signal we processed), there are two secondary peaks that correspond to the target at the same angle but with a range of $\pm\delta R$. This comes from the fact that the inner product of two signals with close range can lead to a non-zero coefficient.

5.3.6 Discussion

The matching Pursuit algorithm seems to perform well when the number of targets reflecting a high quantity of power is low and when the signal is perfectly calibrated.

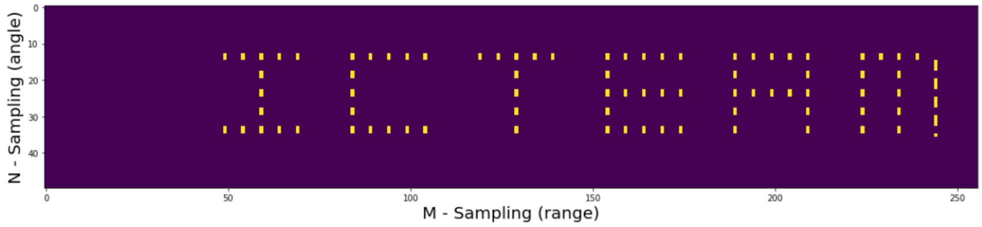

Figure 5.9: Polar plot of the simulated image resulting from the Matching Pursuit Algorithm for $s = 150$ and $\rho = 0.1$. We see that the image is recovered without artifact such as ripples that we got when we used the Fourier Transform.

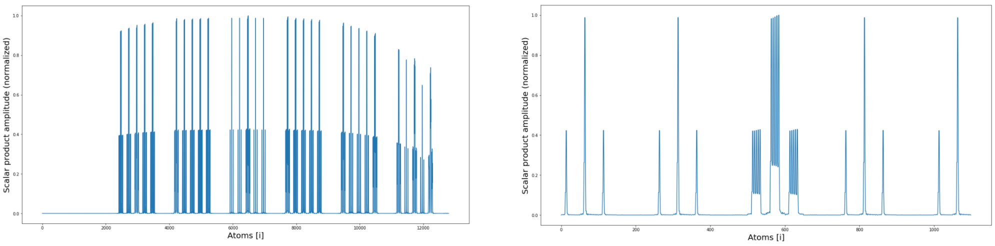

Figure 5.10: Values of the coefficient resulting from the inner product between the signal and the dictionary of signals (coefficients are normalized). On the left, a full view plot of the coefficient and on the right, a zoom around the coefficient corresponding to the letter "T". We see that the peaks at the center are more dense because they correspond to the vertical bar of the T which are point at the same range, the other peak are those of the horizontal bar.

The computational time of this algorithm is most important than for the Fourier Transform algorithm due to the creation of the dictionaries. In fact, they have a large size that increases really fast with M and N : the complexity of the dictionary generation is $\mathcal{O}(M^2N^2)$.
Using the Matching Pursuit algorithm is then restricted a simple target detection.

Chapter 6

Practical Design

In this chapter, we will link the model developed in section 4 to a practical context. More precisely, this chapter presents the transition from the theory to the applications presented in chapter 7.

6.1 Constraints and limits

This section aims at defining the constraints imposed by the model developed above on the parameters of the problem. We will thus start from the model derived in section 4 and apply it to practical context. The objective is to develop all the tools required to design properly the measurement setups that we will realise and present in section 7. As a reminder, the simplified version of the model can be written as

$$s_r^{BB}(t,t') \overset{\psi}{\simeq} \underbrace{\exp\left[4\pi j \frac{B}{cT_c} R_x t'\right]}_{\text{Fast time dependent}} \cdot \underbrace{\exp\left[4\pi j \frac{f_0}{c} \sin(\theta)(vt)\right]}_{\text{Slow time dependent}} \tag{6.1}$$

And after discretisations :

$$S_r^{BB}[m,n] \overset{\psi}{\simeq} \underbrace{\exp\left[4\pi j \frac{B}{cM} R_x m\right]}_{\text{Fast time dependent}} \cdot \underbrace{\exp\left[4\pi j \frac{f_0}{c} \sin(\theta)(n\Delta d)\right]}_{\text{Slow time dependent}} \tag{6.2}$$

The 2D-discretization that we have applied to develop the model in section 4 has an impact both on the parameters of the considered problem and on the quality of the results that we will obtain. Furthermore, the hypotheses that have been made to simplify it implies some constraints on the problem geometry, as presented in sections 4.6 and 3.

6.1.1 Spatial domain

When we discretised equation 6.1, we have indirectly imposed spatial resolutions to our radar system. Those are represented in green in Figure 4.12. In polar coordinates, this gives

$$R_{max} = M \cdot \Delta R \qquad \text{and} \qquad \theta_{max} = N \cdot \Delta\theta. \tag{6.3}$$

with ΔR and $\Delta\theta$ the spatial resolutions, M and N the number of sample in both direction and R_{max} and θ_{max} the range of vision of the radar under our sampling configuration. The signal being expressed in function of $\sin\theta$, we also have

$$\Delta\theta = \arcsin\left(\Delta\left(\sin\left(\theta\right)\right)\right) = \arcsin\left(\Delta\alpha\right) \tag{6.4}$$

where we have posed $\alpha = \sin\theta$. To derive expressions for those resolutions, we consider the maximal value in the frequency domain as it will correspond to the lowest in the temporal domain. In fact, the largest frequency will correspond to the inverse of the smallest time (as, for example, the Fourier transform of a $\delta(t)$ function). By equalising the maximal frequencies of both exponential to 2π and considering equations 6.3 we find

- **Range resolution**

$$4\pi\frac{B}{cM}M\Delta R_x = 2\pi \quad \Leftrightarrow \quad \Delta R_x = \frac{c}{2B}. \tag{6.5}$$

- **Angular resolution**

$$4\pi\frac{N\Delta d\Delta\left(\sin\theta\right)}{\lambda} = 2\pi \quad \Leftrightarrow \quad \Delta\alpha = \Delta(\sin\theta) = \frac{\lambda}{2N\Delta d} = \frac{\lambda}{2L_{rail}}. \tag{6.6}$$

with $\lambda = \frac{c}{f_c}$ the wavelength in $[m]$ and L_{rail} the length of the radar path in $[m]$.

6.1.2 Temporal domain

The most important constraint for the sampling in temporal domain is defined by the Nyquist theorem to avoid aliasing. We have to ensure that sampling frequencies are at least two times greater than the maximal signal frequencies in slow and fast time domain, respectively. This gives us the following constraints for M and N.

- **Fast time sampling** :

$$f_s^{samp} = \frac{1}{T_s^{samp}} \;\geq\; 2 \cdot f_{s,max} = 4\frac{B}{cT_c}R_{x,max}\;\left[\frac{1}{s}\right]. \tag{6.7}$$

  By using the fact that $T_c = M \cdot T_s$ derived in section 4, we find

$$M \leq \frac{4B}{c}R_{x,max}\quad [\backslash]\,. \tag{6.8}$$

- **Slow time sampling**

$$f_c^{samp} = \frac{1}{T_c^{samp}} \;\geq\; 2 \cdot f_{c,max} = 4\frac{f_0}{c} v \sin\left(\theta\right)_{max} \;\left[\frac{1}{s}\right]. \qquad (6.9)$$

By using the facts that $\Delta d = v \cdot T_c$ and that $\left(\sin\theta\right)_{max} = N \cdot \Delta\left(\sin\theta\right) = N \cdot \Delta\alpha$, we find

$$N \leq \frac{c}{4 f_0 \Delta\alpha \Delta d} \quad [\backslash]. \qquad (6.10)$$

6.1.3 Model hypotheses implications

Far field The first hypothesis that was made to construct a model from the problem presented is the Fraunhofer assumption, that allows us to work in a "far field" configuration it the condition 6.11 is respected.

$$L_{target} \;\gg\; \frac{L_{rail}^2}{\lambda} = \frac{(N \cdot \Delta d)^2}{\lambda} \qquad (6.11)$$

with $L_{\text{target}} = R_{\text{target}}$ the distance between the radar and the target that we want to recover.

Magnitude order analysis and simulations As discussed above, we have neglected several terms to obtain the simplified version of the model presented in equation 6.1. We have performed simulations and results have been discussed in section 4.6. Table 4.2 overviews resulting conditions on f_c, R_x, y and x. We observe that those concerning the geometry of the problem (distances R_x, x and y) are consistent with the far field assumption.

6.2 Technology

The purpose of this section is to briefly explain the technology used to perform measurements presented in section 7. We are using a specific radar that is moved on a rail and each of them presents characteristics and limits that we will discuss in section 6.3.

6.2.1 Radar

The radar that will be used for our measurement is a K-MD2 24GHz FMCW (Frequency Modulated Continuous wave). Its principal characteristics are presented in Table 6.1.

Carrier frequency	24	$[GHz]$
Bandwidth	$\in$ [50 500]	$[MHz]$
Wavelength	1.25	$[cm]$
Azimuth aperture	±16.4	[°]
Elevation aperture	±9.1	[°]

Table 6.1: Overview of the parameters of the radar *K-MD2* from *RFbeam Microwave GmbH.* [30]

The carrier frequency of the radar is around 24 [GHz]. More precisely, it varies in the range [23.8 24.8] [GHz] but for a sake of simplicity we will consider this frequency f_0 as equal to 24 [GHz]. The radar can work with a bandwidth up to 500 [MHz].

Fo each acquisition, the radar sends a frame composed of 257 chirps. As presented in Figure 6.1, the first chirp is discarded so only 256 chirps are use. Every chirp is discretised with 260 samples but the first 4 samples are discarded. As we need only one measurement by position, we will perform an arithmetic mean over the 256 chirps sent by the radar. It gives a total number of samples $M = 256$ for each position.

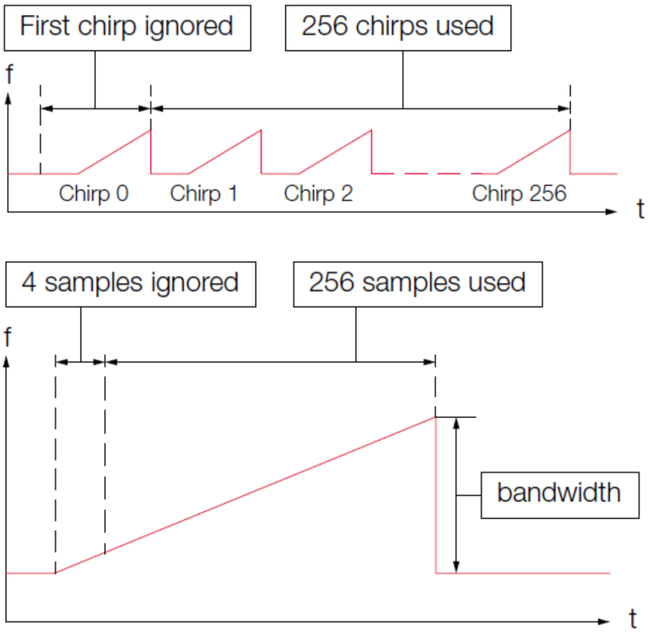

Figure 6.1: Representation of the signal send by the radar to perform an acquisition, from [30].

Our radar has one emitting antenna T_X and three receiving antennas that can be used : R_{X1}, R_{X2} and R_{X3} but only the antenna R_{X1} is used in our application. This antenna is a small antenna array made of nine array elements placed as shown in Figure 6.2. As detailed in section 2.4, we can create a beam with thinner width using multiple antenna elements and the radar presented here uses this technique to get the radiation pattern shown in Figure 6.2.
The aperture angles of this radar are presented in Table 6.1.

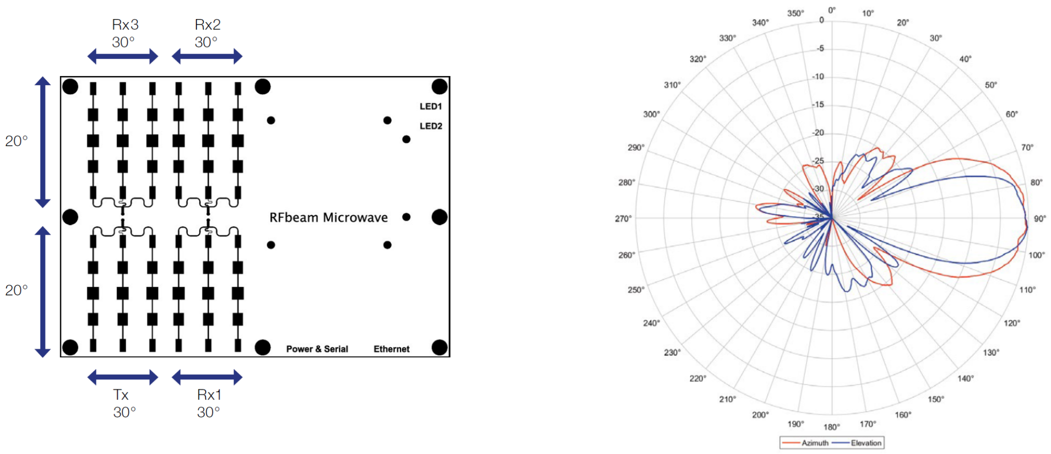

Figure 6.2: Radar antennas disposition of the radar : on the left, the disposition of each emitting and receiving antennas and, on the right : the radiation pattern of the antennas in azimuth and elevation angles.

6.2.2 Rail

The rail used for the experimental part of the master thesis is displayed in Figure 6.3. It is a non-motorised rail on which the radar support (red circle in the Figure) can be moved manually.
The rail course is around 60 $[cm]$ with a graduation in $[cm]$ or in [inches]. We dispose of a second part of that rail with a course of 30 $[cm]$ allowing us to increase the radar path length. However, as we do not have all the pieces required to properly join both pieces, increasing the rail length leads to a rough assembly that induces loss of precision in the measurement.
The piece circled in red in Figure 6.3 allows us to tilt the radar with regards to the vertical. Nevertheless, the precision of the provided tilt angle measure is quite poor.

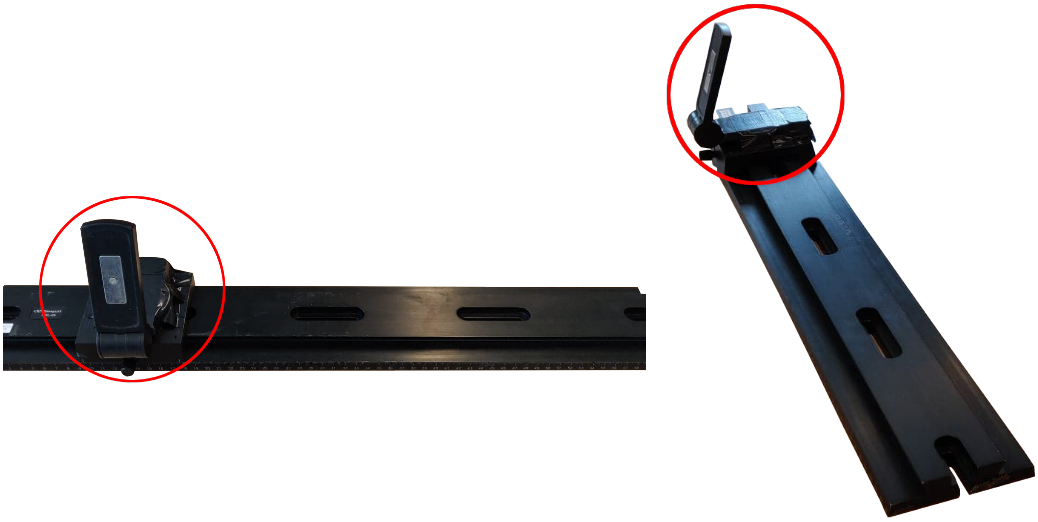

Figure 6.3: Rail used for the measurements presented in section 7 with the part aimed at supporting the radar identified in red. The rail course is around 60 $[cm]$ with graduation either in $[cm]$ or in [inches].

6.3 Contextualisation

Constraints presented above depends on parameters that are fixed by the radar, the environment or the problem geometry. Our measurement setups will thus be constrained by the available technology.

6.3.1 Spatial domain

First the range resolution is limited as the bandwidth cannot exceed 500 [MHz]. We have

$$\Delta R = \frac{c}{2B} \quad \in [15 \quad 0.3]\,[m] \tag{6.12}$$

and we are thus forced to work with targets that exceed 30 $[cm]$.
Second the angular resolution is constrained by the rail imprecision. In fact, we do not have a motorised rail and thus have to move the radar manually. We are thus limited to rail step distances that are not too small and easy to achieve manually without error. For example, we will prefer to work with $\Delta d = 1\,[cm]$ or $\Delta d = 0.5\,[cm]$ than with a Δd equal to $0.3\,[cm]$. For precision reasons, Δd is thus limited to $0.5\,[cm]$. In addition to this, we cannot perform the acquisition while moving continuously the radar as it is not motorised. Thus we will not be able to use the Doppler algorithm in order to enhance the angular resolution of the system.

Furthermore, L_{rail} is also limited to $60\,[cm]$ on a simple rail. It is always possible to work with a larger length but this would imply to join several rail part and will thus induce a lack of precision and difficulties to ensure a certain consistency between the samples. The impact of a limited rail length is twofold :

1. It limits the angular resolution through

$$\Delta\alpha = \Delta(\sin\theta) = \frac{\lambda}{N \cdot \Delta d} \tag{6.13}$$

2. It increases the minimal distance required between the radar and the targets to stay in the Far Field consideration, through the Fraunhofer condition developed in section 3.

$$L_{\text{target}} \gg \frac{L_{\text{rail}^2}}{\lambda} \tag{6.14}$$

Finally, the azimuth and elevation aperture angles of the radar will limit the dimensions of the setup used for the measurements. In fact, a total elevation angle of $|\pm 9.1°| = 18.2°$ offers a limited visible height at small range. We will thus have to adapt carefully the tilt angle of the radar. This is also valid for azimuth direction, where we will have to measure setups that are not too *wide*.

6.3.2 Temporal domain

The number of samples in the fast temporal domain is imposed by the radar, as explained above. We have $M = 256$.

For the slow time sampling, we are limited by the available rail. In fact, as its precision and its length is limited, N could not exceed a value of 100 without loss of precision.

Chapter 7

Measurement results

This chapter presents the relevant results we have obtained with several systems designed from the simplified model developed in section 4. We have worked at several places in Louvain-la-Neuve in order to exploit different kinds of environments. The main idea was to observe limits of our model, of our radar and of the algorithms we used.

Material Each measurement has been performed with the radar presented in Table 6.1 that we moved step by step the rail presented in section 6.2.2. This way, all the configurations follow the **Start and Go** configuration.
For each measurement, we were using either *targets* or *barrels* (see Figure 7.1) as reference to map the recovered image to a satellite view from *Google Earth* or simply to recover shapes or particular effects. Thus, we could verify the quality of our measurements and algorithms.

Figure 7.1: Target (left) and barrel (right) used as reference for the measurements. The target measures 45.72 $[cm]$ at is diagonal. The dimensions of the barrel are $(\text{Height}, \text{Diameter}) = (53.2, 40.8)\ [cm]$.

7.1 FFT SAR algorithm

In this section we present results obtained using the FFT SAR algorithm as post-processing. We thus recover an image of the targeted scene by performing a 2D-FFT of the received signal, that we approximate as in equation 4.48. As explained in Section 5, this algorithm leads to multiple artifacts that will be discussed in this section.

7.1.1 Calibration

By performing measurements with the radar presented in Table 6.1, we have realised that a parasitic frequency generated by the radar was much more important in intensity than the frequencies recovered from the targets. Thus, after the 2D-FFT process, we were not able to see anything other than this parasitic peak. To cancel this parasitic peak, we have performed several measurements of the radar response in an anechoic room in order to register its intrinsic impulse response. Then, we have computed the arithmetic mean over all the measurement to obtain an $M \times 1$ calibration vector, presented in Figure 7.2.

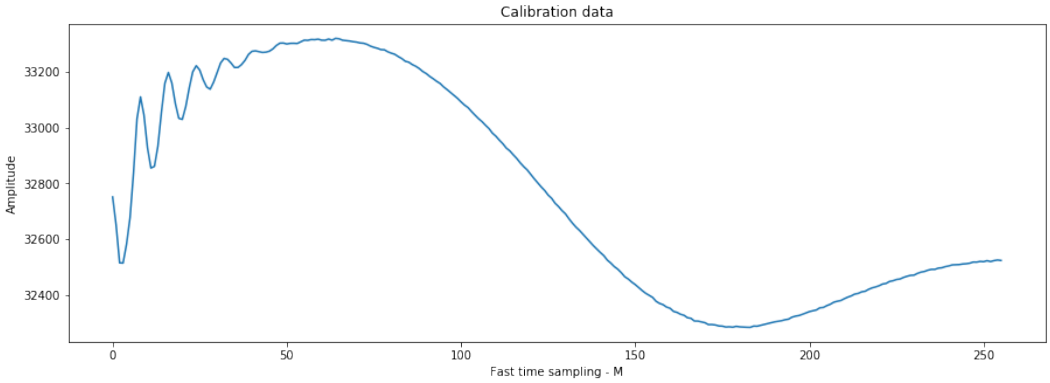

Figure 7.2: Calibration data in temporal domain, obtained by computing the mean of 20 measurements performed in an anechoic room.

This signal was subtracted to the raw data obtained from our measurements, just before applying the 2D-FFT. We will show later that the parasitic peak is strongly attenuated and we are thus able to observe a much more complete signal. This calibration step has been applied in most of the measurement data that will be presented in this section. However, we have sometimes applied a *background subtraction* processing step instead. This consists in subtracting a measurement of the background without any target to the data obtained in the same background with the targets. This way, the impulse response of the radar and the parasitic effects due to the environment are partially cancelled.

7.1.2 Maxwell antenna

The first measurement that we have performed was from the second floor of the Maxwell building.

Objectives The purpose of this measurement was to recover the position of the "Maxwell Parabola", forming a triangle with two targets we had placed. This would ensure us that our model was working properly.

Setup The radar was placed on the second floor of the Maxwell building, in the direction of the parabola. We had placed 2 targets as references, their position with regards to the parabola are presented in Figure 7.3.

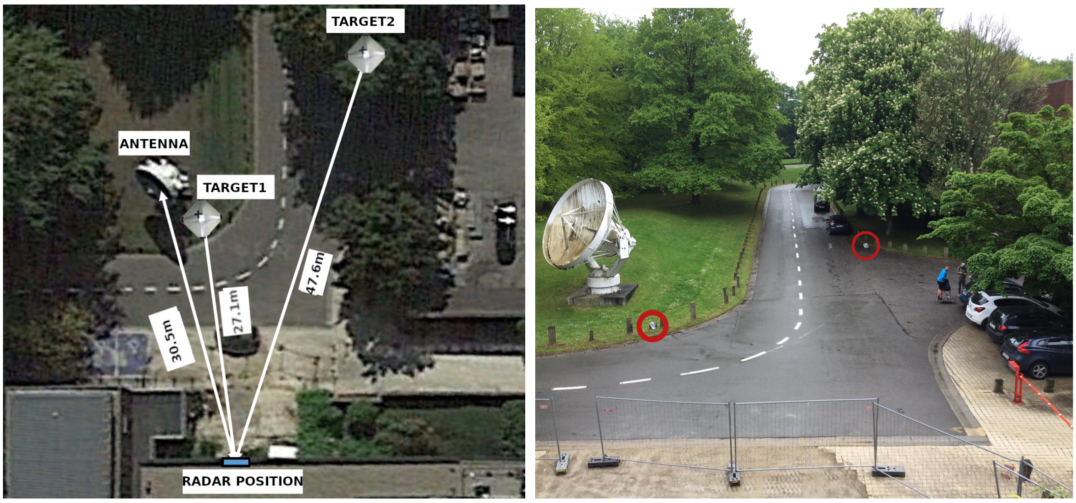

Figure 7.3: Satellite view (left) and radar view (right) of the set-up for the measurement from Maxwell building : two metallic targets were placed at a range distance of 27.1 $[m]$ and 47.6 $[m]$ from the radar, while the parabola is at a range distance of 30.5 $[m]$ from the radar. The tilt angle of the radar compared to the horizontal was 15° and the height of the radar compared to the ground was 8 $[m]$.

An overview of the parameters used for this measurement is proposed in Table 7.1.2. We were working with a rail of length $L_{rail} = 50\,[cm]$ and steps $\Delta d = 0.5\,[cm]$. We performed $N = 100$ measurements. We used a bandwidth of 500 [MHz]. Finally, equations 6.5 and 6.6 allowed us to compute range and angular resolutions. Fraunhofer distance is computed with equation 6.11

Parameter	**Value**
Radar bandwidth	500 [MHz]
Rail length	$L_{\text{rail}} = 50\,[cm]$
Fraunhoher distance	$L_{\text{target}} \gg 20\,[m]$
Radar step distance	$\Delta d = 0.5\,[cm]$
Number of azimuth samples	$N = 100$
Number of range samples	$M = 256$
Range resolution	$\Delta R = 30\,[cm]$
Angular resolution	$\Delta\theta = \arcsin(\Delta\alpha) = 0.71°$
Maximal range	$R_{max} = 76.8\,[m]$

Table 7.1: Overview of the parameters used for the measurement of the Maxwell parabola.

Post-processing steps

1. Mean over the 256 chirps send by the radar for each position.
2. Calibration, following procedure detailed in section 7.1.1.
3. 2D-FFT using a padding coefficient of 3 (meaning that we add 2 zeros per sample in the initial signal) for both range and azimuth directions.
4. Polar coordinates plot, in $\log_{10}$ scale, using the function *pcolor* from Python to display a polar view of the image data.
5. Adaptation of the dynamic color range of the recovered image in order to reduce the background reflection and noise impact and to highlight to target positions.

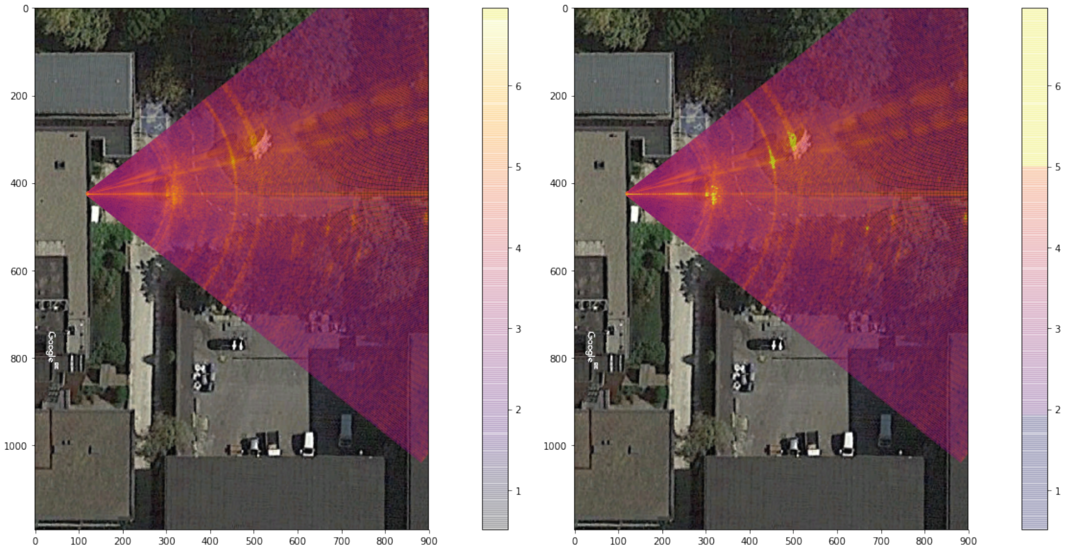

Figure 7.4: Result of the Maxwell antenna measurement without dynamic color range modification (left) and with the modification (right). Measurement conditions are exposed in Table 7.1.2.

Discussion Results are displayed in Figure 7.4. We observe that the first target and the antenna are well recovered and so are the grids that were in front of them. Points of lower intensity may correspond to the second target and to the cars that were parked on the bottom of the picture. As those points are much further away than the antenna, it could be interesting to amplify their intensity as a "post-processing" treatment.
In addition to the recovered targets, we observe some undesirable artifacts due to the FFT algorithm. The most important are the ripples due to the finite duration of the pulse sent by the radar, as discussed in section 5. Those can be observed in range and angular directions. Figure 7.5 presents a sample of this ripple in azimuth direction at the position of the first target. We observe a shape quite close to a *sinc* function, which confirms our analysis.

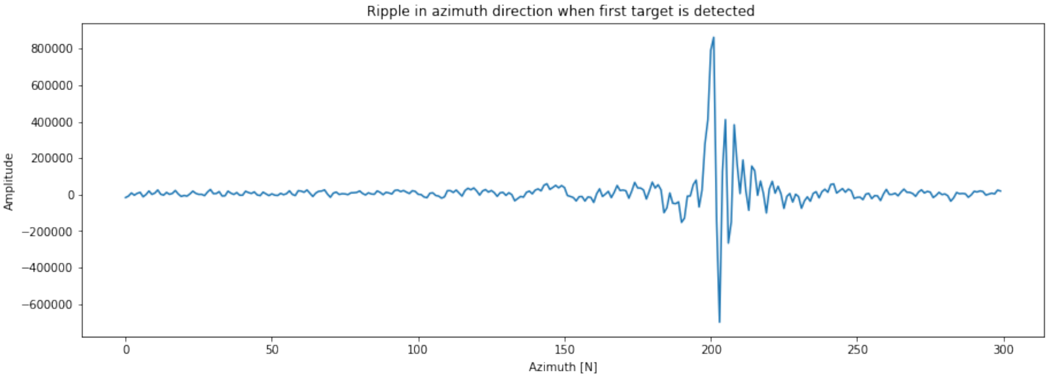

Figure 7.5: Sample of the ripple in azimuth direction at the position of the first target ($R = 27.1\,[m]$) after the calibration and the 2D-FFT, with a padding coefficient of 3.

Furthermore, the Fraunhofer condition to work in a far field configuration is not perfectly respected. L_{targets} are greater than $20\,[m]$ (see Table 7.1.2) but the sign $\gg$ could be discussed. In fact, the targets are disposed further away than Fraunhofer distance but not *much further* away. This may also induce ripples. This will be discussed later.
Finally, the effects of the calibration process are presented in Figure 7.1.2, which displays the results of this measurement with and without the calibration step. As explained above, we obtain a much more complete signal once the parasitic peak is cancelled.

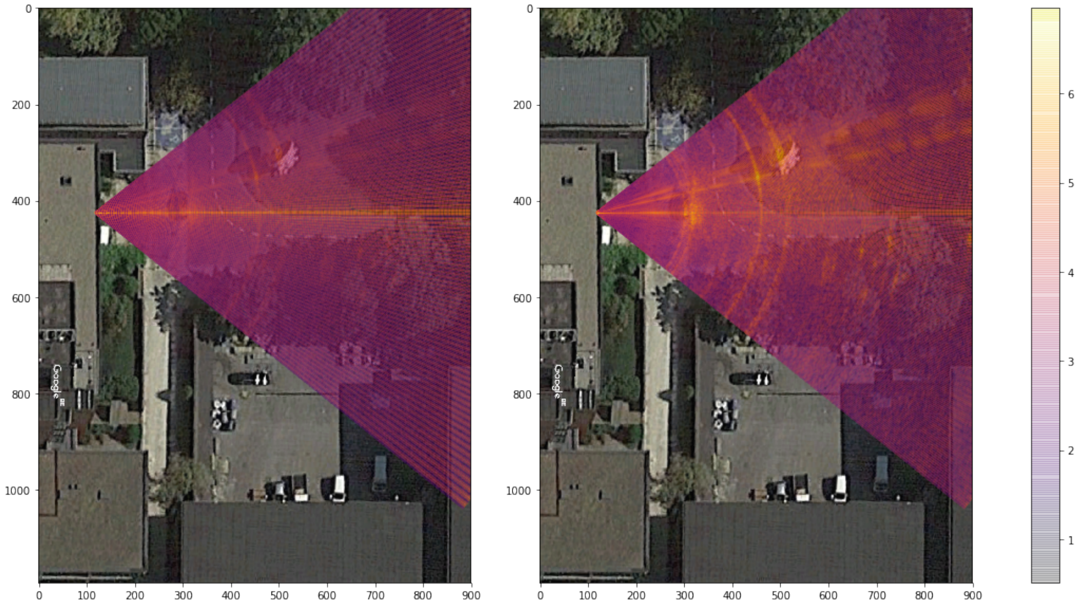

Figure 7.6: Maxwell antenna measurement results obtained with the setup presented in Table 7.1.2 and Figure 7.3, without calibration (left) and with calibration (right).

7.1.3 Interaction between targets

The set of measurements presented in this section aims at analysing how waves can interact when several targets are close to each other.

Saint Barbe entrance

Objectives As the main entrance of the Saint Barbe building is composed of a row of metallic poles, it is an ideal environment to perform radar measurements. Initially, the objective was twofold:

1. Recovering the row and thus verify the ability of our model to properly recover a straight line.
2. Analysing the evolution of the azimuth resolution with the range distance. As we are working in polar coordinates, this resolution will increase as range increases following relation 7.1.

   $$\Delta y = R \cdot \sin \Delta\theta \tag{7.1}$$

   This way, we should recover properly the poles that are the closest. However, the size of the further poles should rapidly become too small with regards to the azimuth resolution.

Setup The radar was placed on a table in diagonal with regards to the straight line formed by the poles of the entrance. The exact position is described in Figure 7.7.

Figure 7.7: Satellite view (left) and radar view (right) of the setup of the Barbe entrance measurement. The radar is placed at 7.9 $[m]$, 10.1 $[m]$ and 12.4 $[m]$ of the first three poles. The tilt angle of the radar with regards to the horizontal was 0° and the height of the radar compared to the ground was 90 $[cm]$. A pole measures $20 \times 12 \ [cm]$.

An overview of the parameters used for this measurement is proposed in Table 7.1.3. We were working with a rail of length $L_{rail} = 50\,[cm]$ and steps $\Delta d = 1\,[cm]$. We performed $N = 50$ measurements. We used a bandwidth of 500 [MHz]. Finally, equations 6.5 and 6.6 allowed us to compute range and angular resolutions. Fraunhofer distance has been computed with equation 6.11.

Parameter	**Value**
Radar bandwidth	500 [MHz]
Rail length	$L_{rail} = 50\,[cm]$
Fraunhoher distance	$L_{\text{target}} \gg 20\,[m]$
Radar step distance	$\Delta d = 1\,[cm]$
Number of azimuth samples	$N = 50$
Number of range samples	$M = 256$
Range resolution	$\Delta R = 30\,[cm]$
Angular resolution	$\Delta\theta = \text{arcsin}\,(\Delta\alpha) = 0.71°$
Maximal range	$R_{max} = 76.8\,[m]$

Table 7.2: Overview of the parameters used for the measurement of the entrance of Saint Barbe building.

Post-processing steps

1. Mean over the 256 chirps send by the radar for each position.
2. Calibration, following procedure exposed in section 7.1.1.
3. 2D-FFT using a padding coefficient of 4 (meaning that we add 3 zeros per sample in the initial signal) for both range and azimuth directions.
4. Polar coordinates plot, in $\log_{10}$ scale, using the function *pcolor* from Python to display a polar view of the image data.

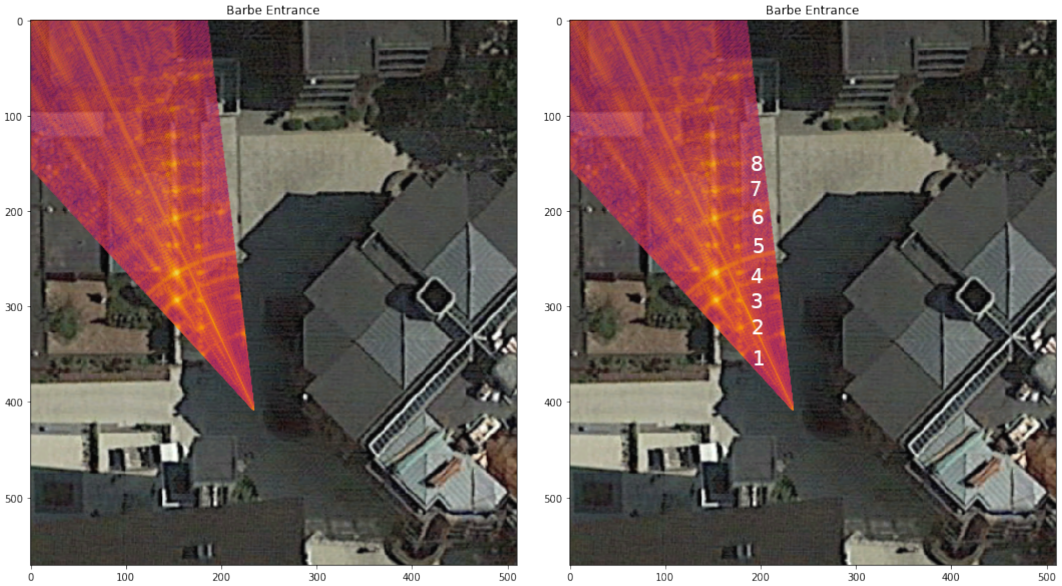

Figure 7.8: Result of the Barbe entrance measurement realised with the setup presented in Table 7.1.3 and in Figure 7.7. On the left the recovered pole numbers are mentioned.

Discussion Measurement results are displayed in Figure 7.8. We first observe that the row of poles is properly recovered, which confirms the validity of the developed model. In a second time we realise that closer poles are quite precisely recovered while the other poles seem to be erased as their distance from the radar increases. This is consistent with our predictions. In fact, we can compute the azimuth resolution for all the poles using equation 7.1 and compare it to the pole dimensions. By observing results displayed in Table 7.3, we understand clearly that poles after the fifth one are nearly invisible for the radar with such azimuth resolutions, as a pole dimension is only 20×12 $[cm]$.

Pole number	**Distance from the radar**	**Azimuth resolution**
1	7.9 $[m]$	10.0 $[cm]$
2	10.1 $[m]$	12.5 $[cm]$
3	12.4 $[m]$	15.3 $[cm]$
4	14.8 $[m]$	18.3 $[cm]$
5	17.9 $[m]$	22.2 $[cm]$
6	20.2 $[m]$	25.0 $[cm]$
7	22.3 $[m]$	27.6 $[cm]$
8	25.4 $[m]$	31.5 $[cm]$

Table 7.3: Evolution of the azimuth resolution with the range distance, for every pole recovered by the radar. Every pole measures $20 \times 12\ \ [cm]$. The numerotation follows Figure 7.8 as a reference.

In addition to this, it is important to note that the ripple due to the 2D-FFT imprecisions is still present. This can also be caused by the far field assumption that is not valid for the closest poles. Finally, Figure 7.8 presents an unexpected feature : a second row of poles is displayed, parallel to the first and "real" one. To explain this second *ghost* row we had one proposition of explanation.
We thought that it could be due to the interactions between all the poles : some waves rebounded from one pole to the next one and then, came back to the radar with a delay corresponding to a greater range. The intensity of the *ghost* row of poles could be stronger than the intensity of the real row thanks to the proximity between poles, their small dimensions and their plane surface not oriented in the direction of the radar (see Figure 7.7). This way, a lot of reflections happened while a very low number of waves came directly back to the radar after reaching a pole, giving a very intense *ghost* row. To validate this explanation, we have performed additional measurements in a very basic environment.

Analysis with barrels

Objectives After the analysis of the results obtained with the Barbe entrance, we have decided to perform additional measurements to confirm our explanation for the *ghost* row. To do so, we will work with two barrels and take measurements for different distances between them. First we measure only one barrel and then we bring another barrel nearer step by step to observe the potential interaction between them. In addition to that, we have performed the same measurement with *wave absorbers* disposed around the barrels in such a way that waves can only reflect in direction to the radar. This second measurement should confirm our hypothesis by erasing the *ghost* targets that we should observe with the first setup. Illustrations of setups are displayed in Figure 7.9.

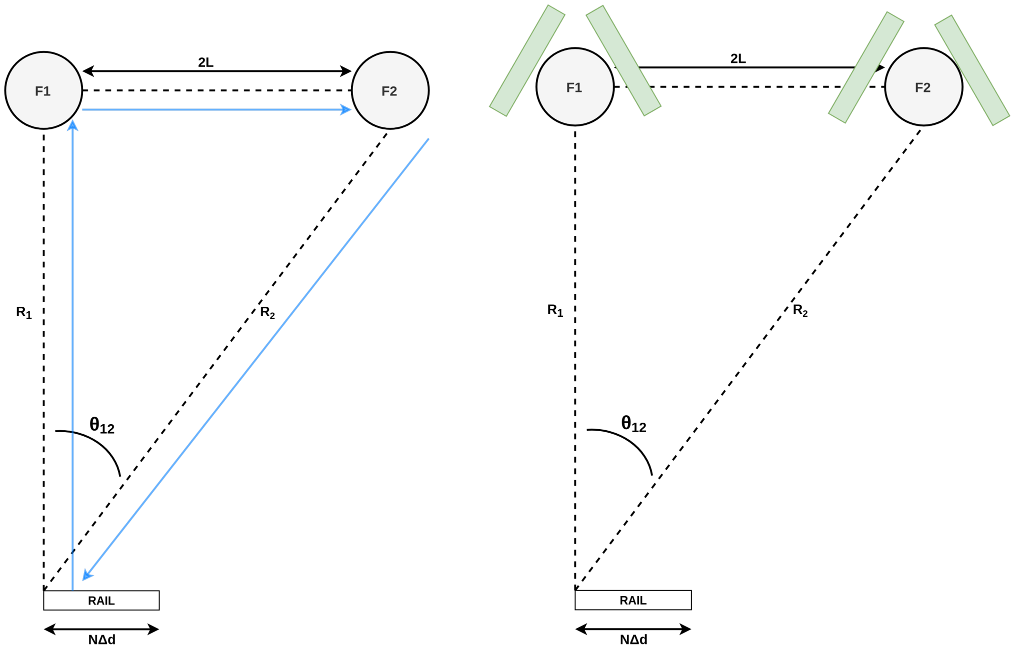

Figure 7.9: Observation of interaction between two barrels - schemes of the setup supposed to generate interaction effects (left) and of the setup with absorbers, supposed to cancel interaction effects (right).

In order to explain the expected interaction phenomena, we start from the simplified model exposed in equation 4.48. The signal reflected by both barrels, $F1$ and $F2$, can be written as :

$$S^{BB}_{r,F1}[m,n] \overset{\phi}{\simeq} \exp\left[2\pi j \frac{B}{cM} 2R_1 m\right] \cdot \exp\left[2\pi j \frac{2\Delta d}{\lambda} n \sin\theta_1\right] \tag{7.2}$$

$$S^{BB}_{r,F2}[m,n] \overset{\phi}{\simeq} \exp\left[2\pi j \frac{B}{cM} 2R_2 m\right] \cdot \exp\left[2\pi j \frac{2\Delta d}{\lambda} n \sin\theta_{12}\right] \tag{7.3}$$

with θ_1, θ_2, R_1 and R_2 the polar coordinates of both barrels. In our setup $\theta_1 = 0$. To recover those coordinates from the received signals, we have to consider the delay required for the *one-way* distance between the barrels and the radar, as the wave travels twice the distance.

$$\tau^F_{\text{one way}} = \frac{2R + 2n\Delta d \sin\theta}{2c} \tag{7.4}$$

By multiplying equation 7.4 by c and applying it to each barrel, we can recover their positions in polar coordinates : $(R_{F1}, \theta_{F1}) = (R_1, 0)$ and $(R_{F2}, \theta_{F2}) = \left(R_2, \arcsin\left(\frac{2L}{R_2} N\Delta d\right)\right)$, using $\sin\theta_{12} = \frac{2L}{R_2}$. Our hypothesis concerning the *ghost* targets generated in Figure 7.8 is that several waves rebounded from one pole to another before coming back to the radar. If we apply this hypothesis to the first setup displayed in Figure 7.9, the reflected wave should travel the distance drawn in blue before reaching the radar back. This gives equation 7.5 for the received signal.

$$S_{r,\text{ghost}}^{BB}\left[m,n\right] \overset{\phi}{\simeq} \exp\left[2\pi j\frac{B}{cM}\left(R_1+R_2+2L\right)m\right]\cdot\exp\left[2\pi j\frac{\Delta d}{\lambda}n\sin\theta_{12}\right] \tag{7.5}$$

Recovered delay is thus

$$\tau_{\text{one way}}^{\text{ghost}} = \frac{R_1+R_2+2L+n\Delta d\sin\theta_{12}}{2c} \tag{7.6}$$

and the recovered distance :

$$D_{\text{ghost}} = \frac{\left(R_1+R_2+2L\right)}{2}+\frac{n\Delta d\sin\theta_{12}}{2}. \tag{7.7}$$

The main objective of those measurements is thus to confirm the validity of our model to explain the interaction effects detailed above. We will compare our predictions for the *ghost* target with measurement results by plotting a circle at polar position

$$\left(R_{\text{ghost}},\theta_{\text{ghost}}\right) = \left(\frac{\left(R_1+R_2+2L\right)}{2},\arcsin\left(\frac{L}{R_2}\cdot N\cdot\Delta d\right)\right) \tag{7.8}$$

and observing if it matches with the recovered interaction effects.

Setups Measurements have been performed on the *Place des Paniers* in Louvain-la-Neuve. The radar was posed on a table, right in front of the first barrel. Figure 7.10 displays a satellite view of the setup.

Figure 7.10: Satellite view (left) and radar view (right) of the setup of the measurement performed with two barrels. The radar is placed at 19.7 $[m]$ from the first barrel. The distance between barrels will vary between $2L = [10\ 4\ 3\ 2\ 1\ 0.5\ 0.2]\ [m]$. R_2 can be computed for each value of $2L$. The tilt angle of the radar with regards to the horizontal was 0° and the height of the radar compared to the ground was 90 $[cm]$.

An overview of the parameters used for this measurement is proposed in Table 7.1.3. We were working with a rail of length $L_{rail} = 50\,[cm]$ and steps $\Delta d = 1\,[cm]$. We performed $N = 50$ measurements. We used a bandwidth of 500 [MHz]. Finally, equations 6.5 and 6.6 allowed us to compute range and angular resolutions.

Parameter	**Value**
Radar bandwidth	500 [MHz]
Rail length	$L_{rail} = 50\,[cm]$
Fraunhoher distance	$L_{\text{target}} \gg 20\,[m]$
Radar step distance	$\Delta d = 1\,[cm]$
Number of azimuth samples	$N = 50$
Number of range samples	$M = 256$
Range resolution	$\Delta R = 30\,[cm]$
Angular resolution	$\Delta\theta = \arcsin(\Delta\alpha) = 0.71°$
Maximal range	$R_{max} = 76.8\,[m]$

Table 7.4: Overview of the parameters used for the measurement performed with barrels at *Place des Paniers*.

Post-processing steps

1. Mean over the 256 chirps send by the radar for each position.

2. Background subtraction, following procedure exposed in section 7.1.1 with a *blank* measurement of the environment performed in the conditions exposed in Table 7.1.3 and Figure 7.9 without barrels.
3. 2D-FFT using a padding coefficient of 4 (meaning that we add 3 zeros per sample in the initial signal) for both range and azimuth directions.
4. Polar coordinates plot, in $\log_{10}$ scale, using the function *pcolor* from Python to display a polar view of the image data.

Discussion Measurement results for the setup without absorbers are presented in Figure 7.11, where the predicted position of the *ghost* target described in equation 7.8 is plotted. We observe that the prediction matches properly with the reality, which confirms our hypothesis. We can thus also conclude that our model describes quite precisely the problem. Furthermore, Figure 7.12 provides a comparison between both setup presented in Figure 7.7, with and without absorbers. We observe that without absorbers, a *ghost* target appears and seems to be at the predicted position. With absorbers, no *ghost* target appears. This means that we have cancelled interactions and prevented waves to reflect from one barrel to the other by positioning correctly the absorbers. This confirms the hypothesis of interaction between targets as only cause for the apparition of a *ghost* target in Figures 7.8 and 7.11. It is important to note that we have moved the radar in opposite direction with regards to the first measurements 7.11, this explain why the scene is inverted.

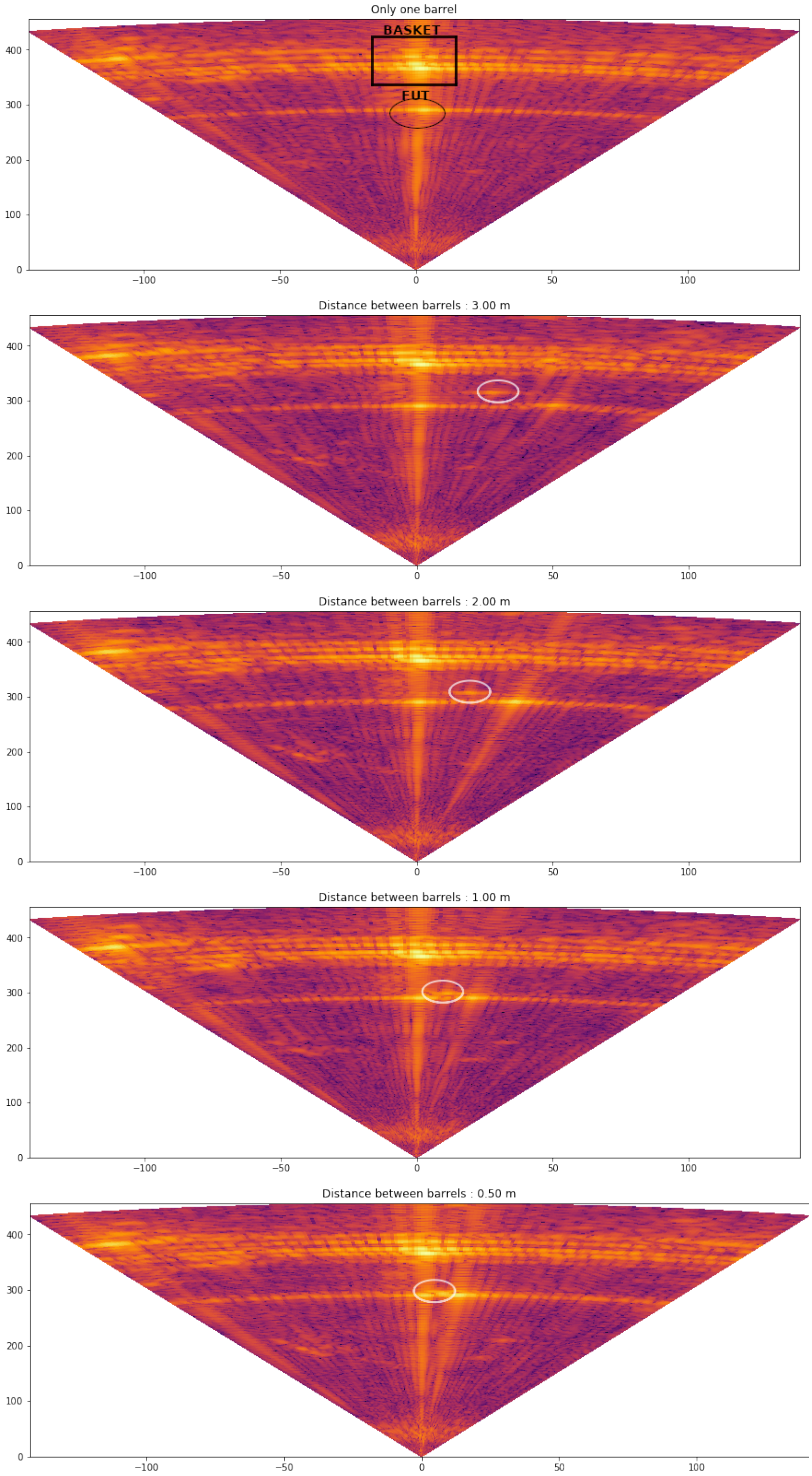

Figure 7.11: Measurement results of the setup presented in Figure 7.10 **without absorbers**. The distance $L_{barrels}$ between the two barrels is varying from 4 $[m]$ to 1 $[m]$ and $\Delta d = 1$ $[cm]$, obtained with the FFT algorithm. A padding has been applied to increase resolution by a factor four. A prediction of the position of the *ghost* target due to interactions between barrels is provided in white.

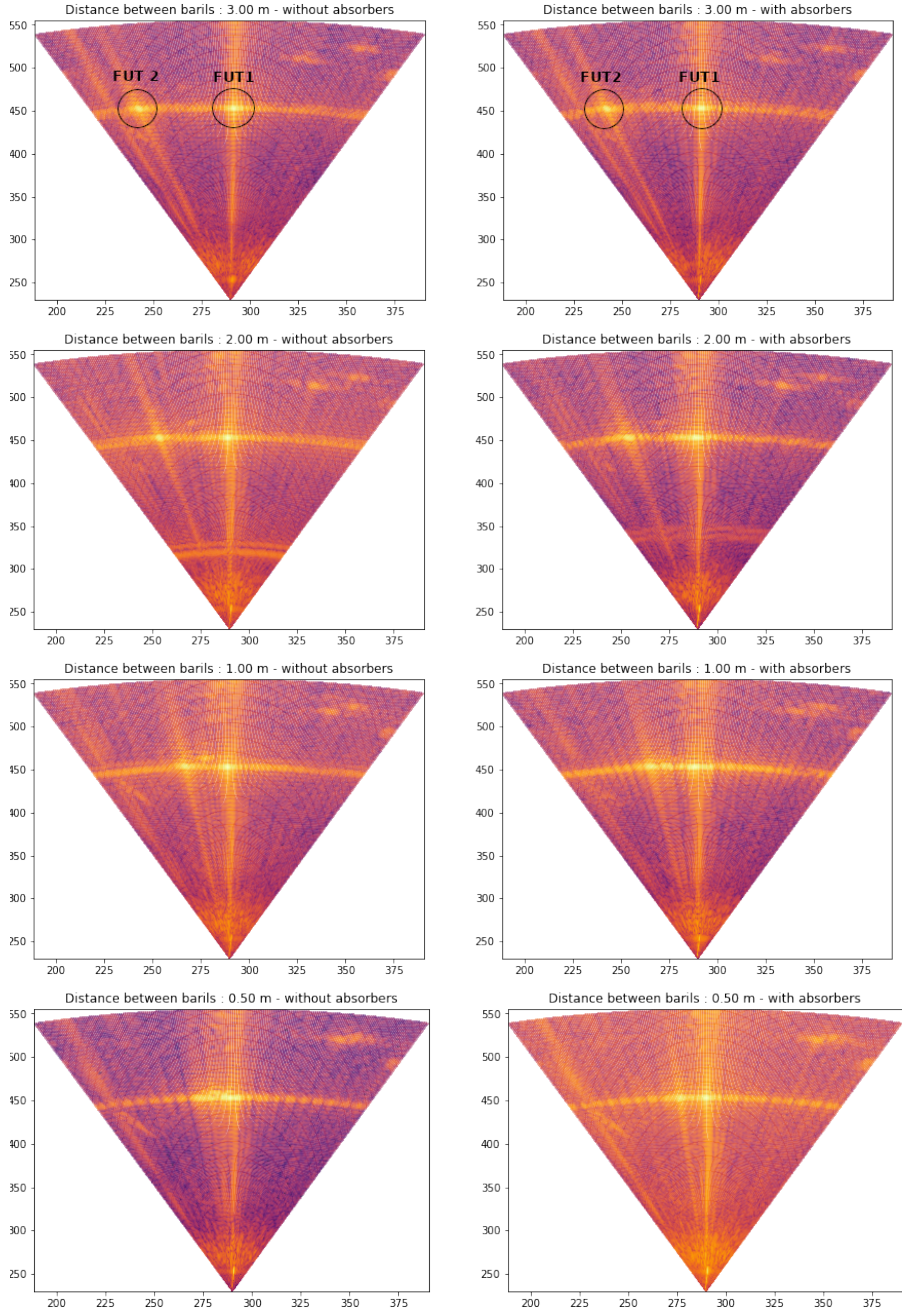

Figure 7.12: Measurement results of the setup presented in Figure 7.10 with (left) and without (right) absorbers. The distance $L_{barrels}$ between the two barrels is varying from 4 $[m]$ to 1 $[m]$ and $\Delta d = 1$ $[cm]$, obtained with the FFT algorithm. A padding has been applied to increase resolution by a factor four.

7.1.4 Fraunhofer assumption

This section presents measurements realised in order to analyse the effect of Fraunhofer assumption when Far Field condition (6.11) is not respected.

Objectives As a reminder, angular resolution and Fraunhofer condition expression are presented in equation 7.9.

$$\Delta\left(\sin\theta\right) = \frac{\lambda}{2L_{\text{rail}}} = \frac{\lambda}{2N\Delta d} \qquad\qquad L_{\text{target}} \gg \frac{L_{\text{rail}}^2}{\lambda} = \frac{\left(N\Delta d\right)^2}{\lambda} \tag{7.9}$$

We observe that increasing the length of the radar path (L_{rail}) offers a finer angular resolution but increases the minimal required L_{target} to stay in the Far Field configuration. We can thus intuitively deduce that there is a tradeoff to be found between an acceptable angular resolution and a Fraunhofer distance adapted to our setup. The purpose of this set of measurement is to compare results obtained with different rail lengths L_{rail} and three targets placed at different range distances L_{target}. Ideally, we should observe that precision of recovered targets increases with the length of the rail until a specific point. Then, the Fraunhofer condition won't be respected anymore and targets should spread in the angular direction. As they are placed at different range distance, the closest target should suffer far field assumption consequences more than the farthest target.

Setup We have performed measurement with three targets of the form presented in Figure 7.1 on the *Place des Paniers* in Louvain-la-Neuve. Targets were disposed as presented in Figure 7.13 and the radar was posed on a table at 90 $[cm]$ to the ground.

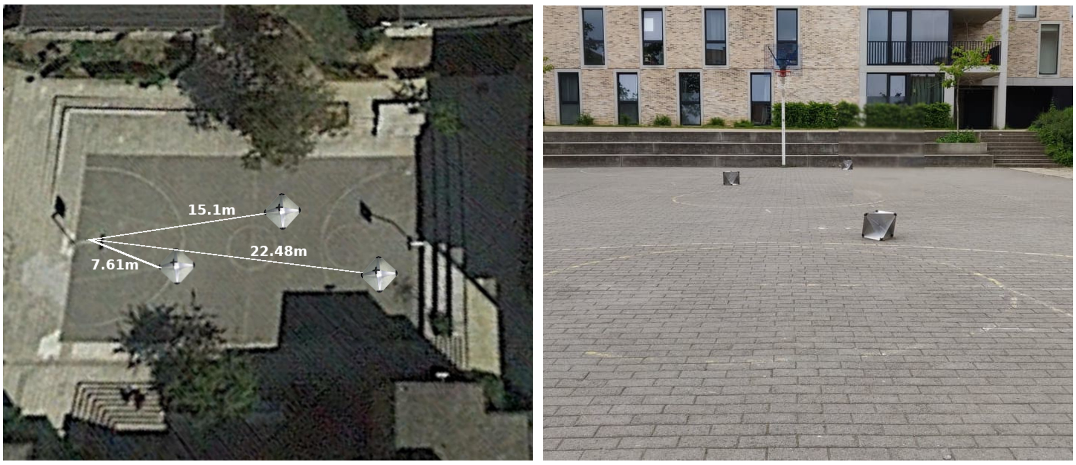

Figure 7.13: Satellite view (left) and radar view (right) of the setup of the measurement performed to quantify Fraunhofer assumption hypothesis. Three targets had been placed at distance $L_{target} = [7.61\ 15.1\ 22.48]\ [m]$. The tilt angle of the radar was $0°$ and its height $90\,[cm]$.

An overview of the parameters used for this set of measurements is presented in Table 7.1.4. We were working with a rail length varying from $10\,[cm]$ to $200\,[cm]$ and steps $\Delta d = 1\,[cm]$. We used a bandwidth of $500\,[\mathrm{MHz}]$. Finally, equations 6.5 and 6.6 allowed us to compute range and angular resolutions.

Parameter	**Value**
Radar bandwidth	$500\,[\mathrm{MHz}]$
Rail length	$L_{rail} \in [10\ \ 200]\ \ [cm]$
Fraunhoher distance	$L_{\mathrm{target}} \gg [3.2\ \ 320]\,[m]$
Radar step distance	$\Delta d = 1\,[cm]$
Number of azimuth samples	$N \in [10\ \ 200]$
Number of range samples	$M = 256$
Range resolution	$\Delta R = 30\,[cm]$
Angular resolution	$\Delta\theta = \arcsin(\Delta\alpha) \in [3.6\ \ 0.18]\ \ °$
Maximal range	$R_{max} = 76.8\,[m]$

Table 7.5: Overview of the parameters used for the measurement performed with three targets at *Place des Paniers.*

We have computed the angular resolution $\Delta\theta$ and the corresponding Fraunhofer condition on L_{target} for each L_{rail}. Results are displayed in Table 7.6. We observe that first target does not respect Fraunhofer condition anymore when the radar path reaches $30\ \ [cm]$. For second target the precision should decrease once the radar path reaches 50 [*cm*] and for third targets once the radar path reaches 60 [*cm*]. Also, it is important to note that we are working with a bandwidth of 500 [MHz] and thus a maximal range of 76.8 [*m*], limiting our reachable Fraunhofer condition.

$\mathbf{L_{rail}}$ **in [cm]**	$\mathbf{L_{target}}$ **in [m]**	$\mathbf{\Delta} \sin\theta$ **in °**
20	3.2	1.79
30	7.2	1.19
40	12.8	0.89
50	20.0	0.71
60	28.8	0.60
80	51.2	0.44
100	80.0	0.36
140	156.8	0.25
160	204.8	0.22
200	320.0	0.18

Table 7.6: Overview of the Fraunhofer condition and angular resolution corresponding to each length of rail used for this measurement.

Post-processing steps

1. Mean over the 256 chirps send by the radar for each position.
2. Background subtraction, following procedure exposed in section 7.1.1 with a *blank* measurement of the environment performed in the conditions exposed in Table 7.1.4 and Figure 7.13 without targets.
3. 2D-FFT using a padding coefficient of 4 (meaning that we add 3 zeros per sample in the initial signal) for both range and azimuth directions.
4. Polar coordinates plot, in $\log_{10}$ scale, using the function *pcolor* from Python to display a polar view of the image data.

Discussion Results for $L_{\text{rail}} \in [10 \;\; 60]$ [*cm*] are displayed in Figure 7.14. As expected, target precision seems to increases when radar path length increases from 20 [*cm*] to 30 [*cm*]. Once that length is reached, the closest target will spread in azimuth direction as L_{rail} keeps increasing. The other target precision will increase until L_{rail} reaches 40 [*cm*] and then decrease. This result is consistent with our predictions and confirms the idea of *critical point*. Results for $L_{\text{rail}} \in [60 \;\; 200]$ [*cm*] are displayed in Figure 7.15. This shows the increasing spread effect for the three targets as L_{rail} exceeds 60 [*cm*]. We observe that the spread is more important for the closest target than for the farthest target, as expected. Finally, results express a certain flexibility with regards to the Fraunhofer condition. In fact, after having analysed Figures 7.14 and 7.15 we could rewrite equation 6.11 as

$$L_{\text{target}} \geq \frac{(L_{\text{rail}})^2}{\lambda} = \frac{(N \cdot \Delta d)^2}{\lambda} \tag{7.10}$$

instead of

$$L_{\text{target}} \gg \frac{(L_{\text{rail}})^2}{\lambda} = \frac{(N \cdot \Delta d)^2}{\lambda} \tag{7.11}$$

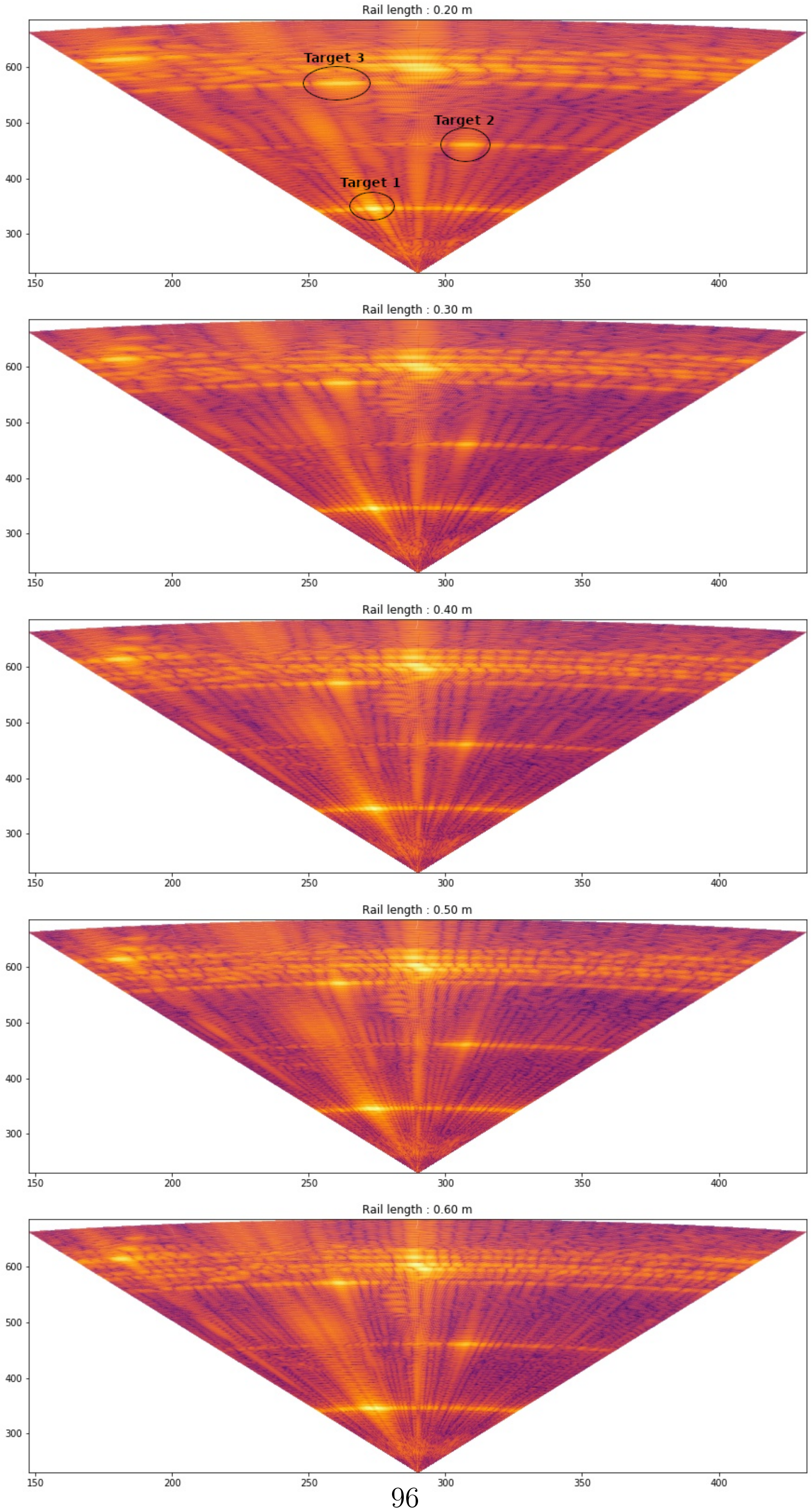

Figure 7.14: Measurement results of the setup presented in Figure 7.13 with L_{rail} varying from 20 $[cm]$ to 60 $[m]$ and $\Delta d = 1$ $[cm]$, obtained with the FFT algorithm. A padding has been applied to increase resolution by a factor four. We observe that **target precision is increasing** and we do not suffer far field assumption consequences.

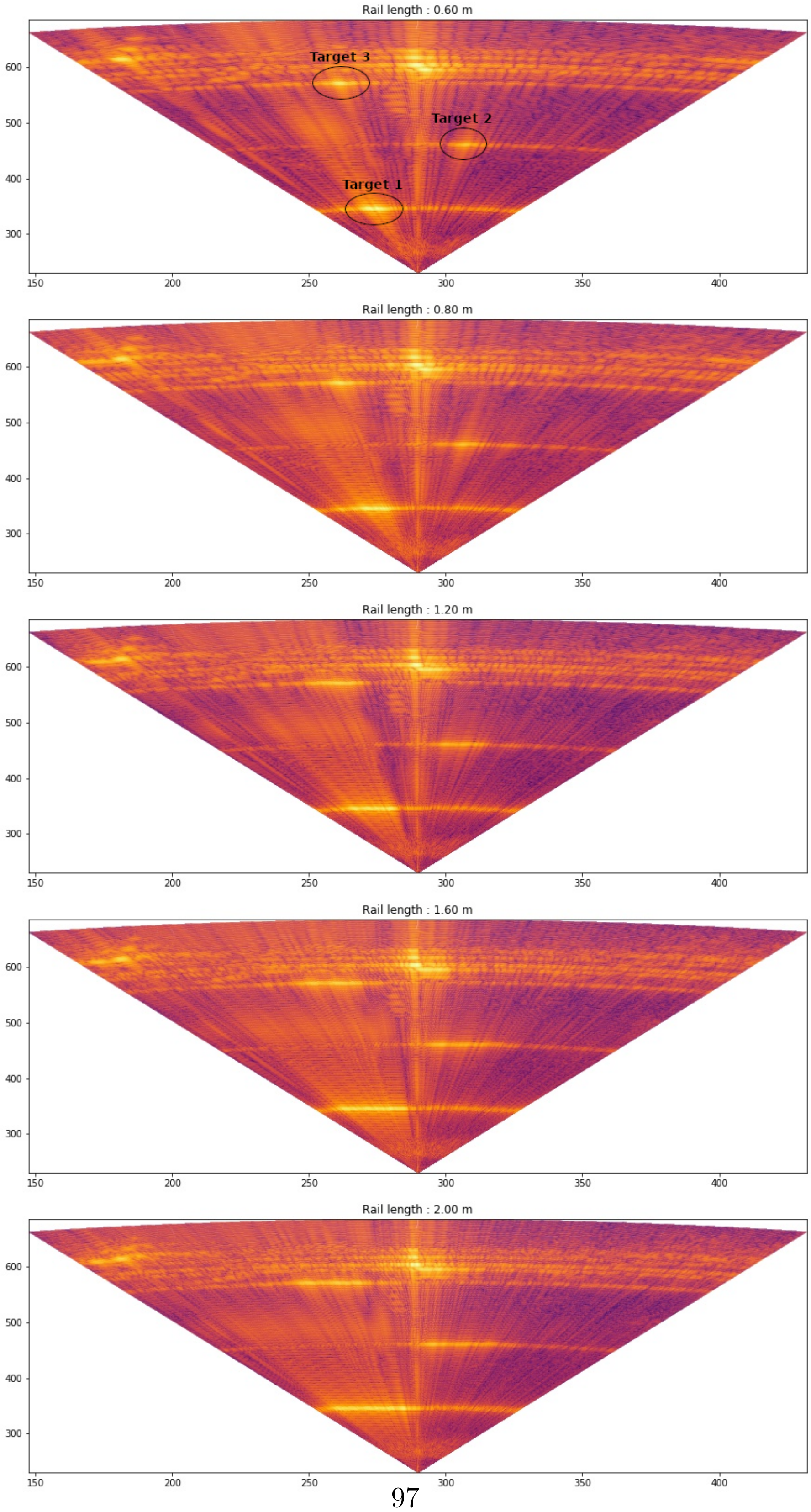

Figure 7.15: Measurement results of the setup presented in Figure 7.13 with L_{rail} varying from 60 $[cm]$ to 2 $[m]$ and $\Delta d = 1$ $[cm]$, obtained with the FFT algorithm. A padding have been applied to increase resolution by a factor four. We observe that **target precision is decreasing** as we suffer far field assumption consequences.

7.1.5 Sensitivity to setup parameters

In this section, we present measurements realised in order to observe our model sensitivity to parameters imprecision.

Objectives The purpose of the measurement presented below is to measure the consequences of a wrong setup and more precisely, an error on the rail step distance Δd. We will thus compare results obtained with a measurement performed with an $\Delta d = 1\,[cm]$ assumed to be perfectly realised and with results from a measurement performed with a $\Delta d = 1\,[cm] \pm 30\%$. This second measurement will thus be obtained by alternating between $\Delta d = 0.7\,[cm]$ and $\Delta d = 1.3\,[cm]$. This way, we will test the robustness of our model with regards to rail step distance error.
Theoretically, we may observe imprecision on the recovered angular coordinate. In fact, from the model we have

$$\begin{aligned}(R_{\text{rec}}, \theta_{\text{rec}}) &= \left(R_t, \arcsin\left(\frac{y_t}{R_t} \cdot N \cdot \Delta\alpha\right)\right) && (7.12)\\ &= \left(\frac{2R_t}{2}, \arcsin\left(\frac{y_t}{R_t} \cdot N \cdot \frac{\lambda}{2N \cdot \Delta d}\right)\right) && (7.13)\\ &= (R_t, \theta_t) && (7.14)\end{aligned}$$

for any target t placed at position (R_t, θ_t) in the radar polar plane of coordinates. However, the azimuth precision should stay acceptable as even if there is an error on Δd measurement, we have performed measurement such as L_{rail} stays constant. This way, the error should not have an irretrievable consequence on the result and may even not be observable at all.

Setup We have worked with ten barrels that we have placed as presented in Figure 7.16. A distance of $90\,[cm]$ separated them and each barrel has a diameter of $40.8\,[cm]$.

Figure 7.16: Satellite view (left) and radar view (right) of the setup of the measurements performed to quantify the impact of setup imprecision. Ten barrels had been placed in a triangle shape at a distance $L_{\text{target},0} = 12.1\,[m]$. Distance between barrels is $90\,[cm]$. The tilt angle of the radar was 0° and its height $90\,[cm]$.

Table 7.1.5 overviews the most relevant parameters of the measurements. Azimuth and angular resolutions have been computed with equation 6.5 and 6.6. It is important to note that most of the barrels are below the Fraunhofer distance, which means that we may observe imperfection in recovered image.

Parameter	**Value**
Radar bandwidth	500 [MHz]
Rail length	$L_{rail} = 50\,[cm]$
Fraunhoher distance	$L_{\text{target}} \gg 20\,[m]$
Radar step distance	$\Delta d = 1\,[cm]\ \pm 30\%$
Number of azimuth samples	$N = 50$
Number of range samples	$M = 256$
Range resolution	$\Delta R = 30\,[cm]$
Angular resolution	$\Delta\theta = \arcsin(\Delta\alpha) = 0.71^\circ$
Maximal range	$R_{max} = 76.8\,[m]$

Table 7.7: Overview of the parameters used for the measurement performed with barrels at *Place des Paniers*.

Post-processing steps

1. Mean over the 256 chirps send by the radar for each position.
2. Calibration, following procedure exposed in section 7.1.1.

3. 2D-FFT using a padding coefficient of 4 (meaning that we add 3 zeros per sample in the initial signal) for both range and azimuth directions.

4. Polar coordinates plot, in $\log_{10}$ scale, using the function *pcolor* from Python to display a polar view of the image data.

Discussion Results obtained with and without rail step error are presented in Figure 7.17. As predicted, the Δd error has nearly no impact on the result. Both images present the same level of precision. This allows us to conclude that only L_{rail} has a great impact on our model precision. More precisely, a wrong L_{rail} measurement will result in a wrong mapping with reality as angular resolution will be wrongly computed. This effect is displayed in Figure 7.18.
However, we observe that recovered barrels are spread in angular direction and that this spread seems to decrease as L_{target} increases. As the spread is present in both results, we can conclude that it is due to the Fraunhofer approximation and not to the introduced rail step error.

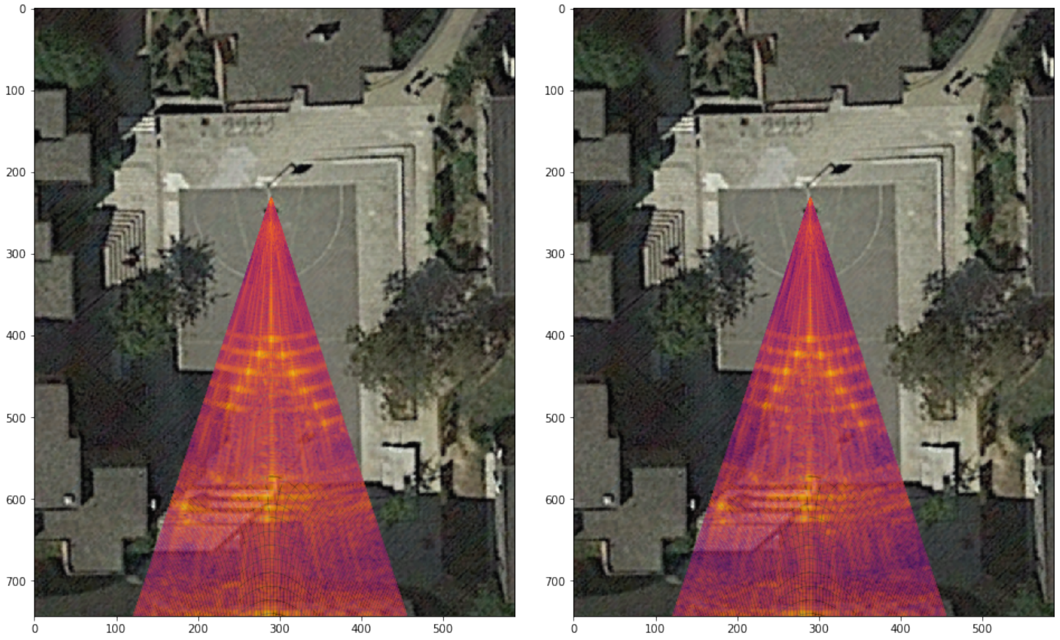

Figure 7.17: Results of the measurement realised with the setup presented in Table 7.1.5 and in Figure 7.16, without the Δd error (left) and with the Δd error (right). No Hamming window has been applied to obtain those results.

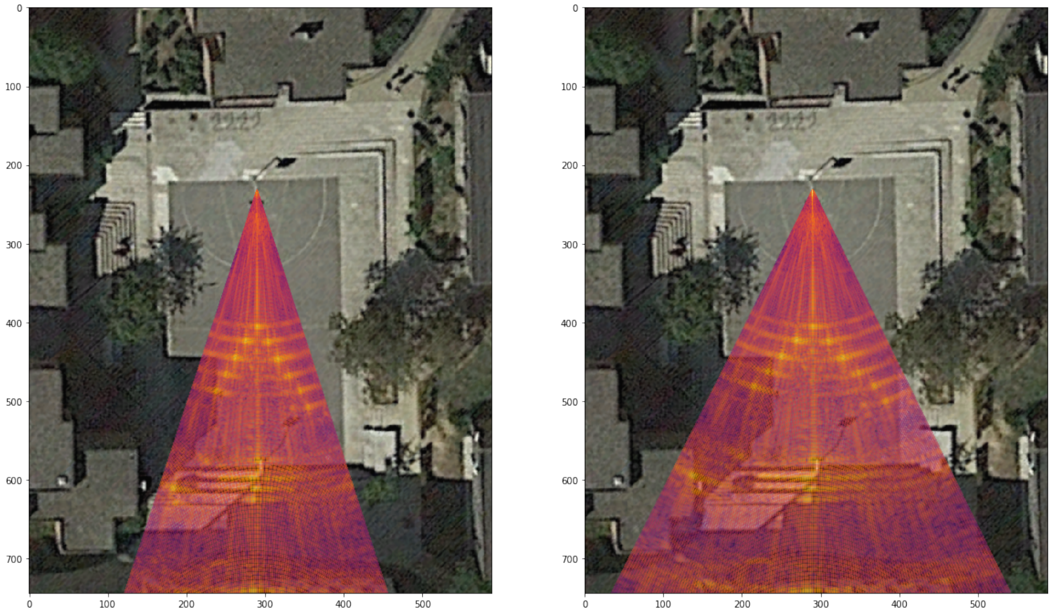

Figure 7.18: Results of the measurement realised with the setup presented in Table 7.1.5 and in Figure 7.16, without the Δd error but with an error on the estimation of L_{rail}. On the left the image is recovered with a *perfect* $L_{\text{rail}} = 50\,[cm]$ and on the right L_{rail} is wrongly estimated as being equal to $35\,[cm]$. No Hamming window has been applied to obtain those results.

7.1.6 Hamming window effect

The purpose of this section is to present and display properly the effect of applying a *Hamming window* during the post-processing step of the data.

Objectives Based on the setup presented in Figure 7.16 and in Table 7.1.5, we will show the impact of the Hamming window and discuss its convenience it our application.

Setup The setup used for this measurement is presented in Figure 7.16 and in Table 7.1.5, without any error on the rail step. We are working with a bandwidth $B = 500\,[\text{MHz}]$ and a step distance $\Delta d = 1\,[cm]$.

Post-processing steps

1. Mean over the 256 chirps send by the radar for each position.

2. Calibration, following procedure exposed in section 7.1.1.

3. 2D-Hamming window.
4. 2D-FFT using a padding coefficient of 4 (meaning that we add 3 zeros per sample in the initial signal) for both range and azimuth directions.
5. Polar coordinates plot, in $\log_{10}$ scale, using the function *pcolor* from Python to display a polar view of the image data.

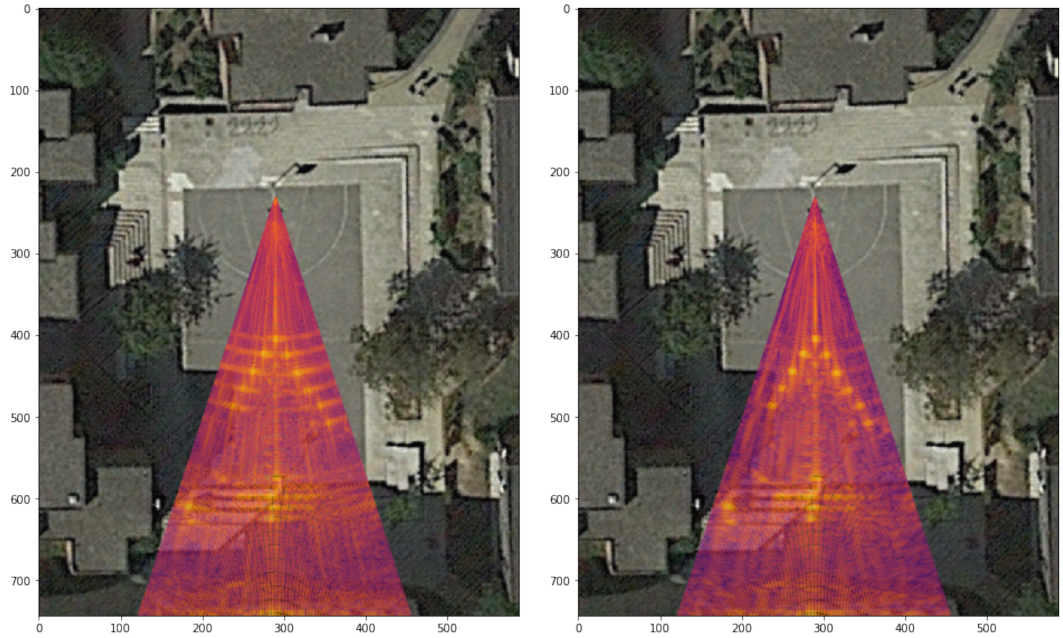

Figure 7.19: Results of the measurement realised with the setup presented in Table 7.1.5 and in Figure 7.16 without Δd error. On the left we have not applied a Hamming window and on the right, a 2-D Hamming window has been applied right before the 2D-FFT.

Discussion Results with and without Hamming window are presented in Figure 7.1.6. We observe that the angular spread of the recovered barrels is strongly attenuated with the Hamming window. As it had been explained in section 5, the principal effect of this post-processing step is to amplify the principal peaks of the 2D-FFT and to attenuate the auxiliary peaks. If its efficiency in other contexts could be discussed, we can conclude that in applications where the Fraunhofer assumption is not properly respected, a Hamming window post-processing step strongly attenuates the impact of the Far Field assumption.

7.1.7 High-pass filtering on the signal

The purpose of this section is to present and display properly the effect of applying a *high pass filter* on the received signal in the post-processing step. The high pass filter used is an IIT digital Butterworth filter with the following definition :

$$H(z) = \frac{\sum_{k=0}^{K} b(k) z^{-k}}{1 + \sum_{l=0}^{L} b(n) z^{-l}}, \tag{7.15}$$

with z the z-transform corresponding to $e^{j\omega}$, a and b the coefficient of the filter (giving by the function *butter* in *Python* fro our application.

Objectives The set-up is the same as the one use for the previous example and can be found in Figure 7.16 and in Table 7.1.5, we will show the impact of using a high pass filtering and it's impact on the image recovered.

Setup The setup used for this measurement is presented in Figure 7.16 and in Table 7.1.5, without any error on the rail step. We are working with a bandwidth $B = 500\,[\text{MHz}]$ and a step distance $\Delta d = 1\,[cm]$.

Post-processing steps

1. Mean over the 256 chirps send by the radar for each position.
2. Calibration, following procedure exposed in section 7.1.1.
3. Applying a high pass filter of frequency equal to $0.1\frac{f_s}{2}$ where f_s is the sampling frequency.
4. 2D-FFT using a padding coefficient of 4 (meaning that we add 3 zeros per sample in the initial signal) for both range and azimuth directions.
5. Polar coordinates plot, in $\log_{10}$ scale, using the function *pcolor* from Python to display a polar view of the image data.

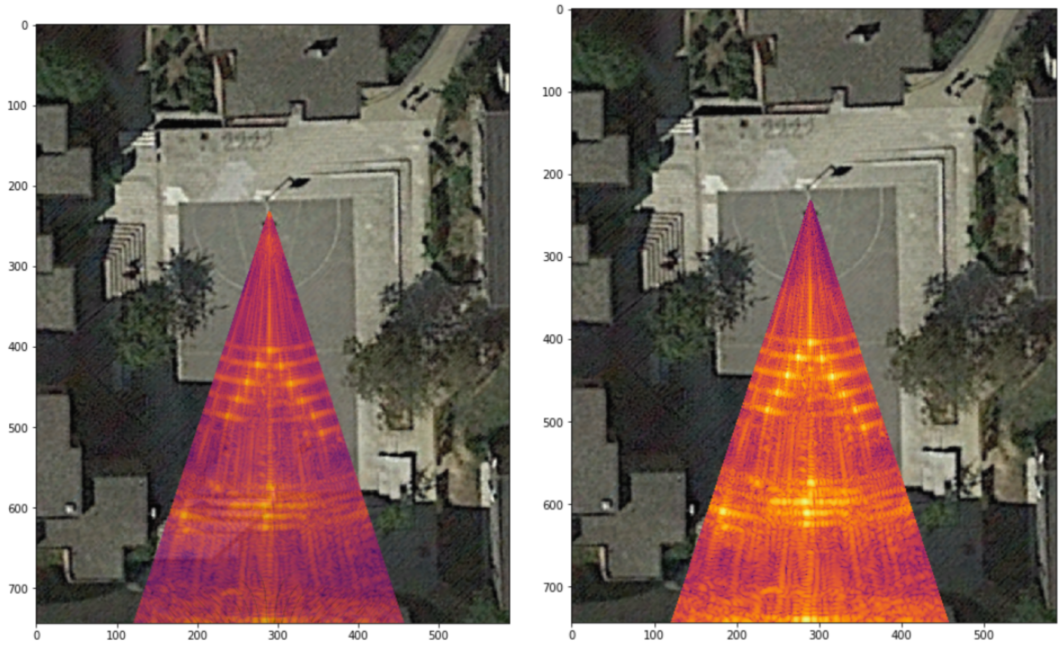

Figure 7.20: Results of the measurement realised with the setup presented in Table 7.1.5 and in Figure 7.16 without Δd error. On the left we have not applied the high pass filtering and on the right, high pass filtering has been applied before performing the FFT.

Discussion Results obtained with and without the high pass filtering are displayed in Figure 7.1.7. The main idea behind the use of high pass filtering is to suppress the parasitic component that occurs for a frequency corresponding to the position ($R = 0, \theta = 0$). Indeed our application does not need the recover really close target (a frequency of $\frac{f_s}{2}$ correspond to a range $R_{max} = 76.8$ [m] so by applying this high pass filter we discard the low range targets.
We see that the image recovered when the high pass filter has been applied is brighter (don't forget we are in log10 scale) because the brightest point previously was at the origin of the image(at low frequency then). A potential application of the high pass could be discarding all the targets that are too close from the radar to focus on the targets that are farther.

7.2 Matching Pursuit algorithm

In this section, the results obtained with the Matching Pursuit algorithm are presented and discussed with regards to the results of the FFT algorithm. The purpose of this set of measurements is to highlight differences between both algorithms on a basic setup.

Objectives We have performed measurements at *Place des Paniers* with one barrel (see Figure 7.1). The main objective is to present the results obtained using the Matching Pursuit algorithm and compare them with those obtained from the Fourier Transform algorithm. In addition to the standard processing, we have also performed *noisy measurement*, where we have added noise to the data as a first post processing step. This allows us to observe the behaviour of both algorithms with noisy signals.
Using the Matching Pursuit algorithm, we should recover a cleaner image without the ripples that we usually observe with the Fourier Transform algorithm. Also, the Matching Pursuit algorithm provides a threshold that gives us a degree of freedom to keep only the main targets.

Set-up The setup used for this measurement is presented in Figure 7.21 and Table 7.2. The barrel is placed at 19.2 $[m]$ of the radar. We are working with a bandwidth $B = 500\,[\text{MHz}]$ and a step distance $\Delta d = 1\,[cm]$. The tilt angle of the radar is 0° and its height 90 $[cm]$.

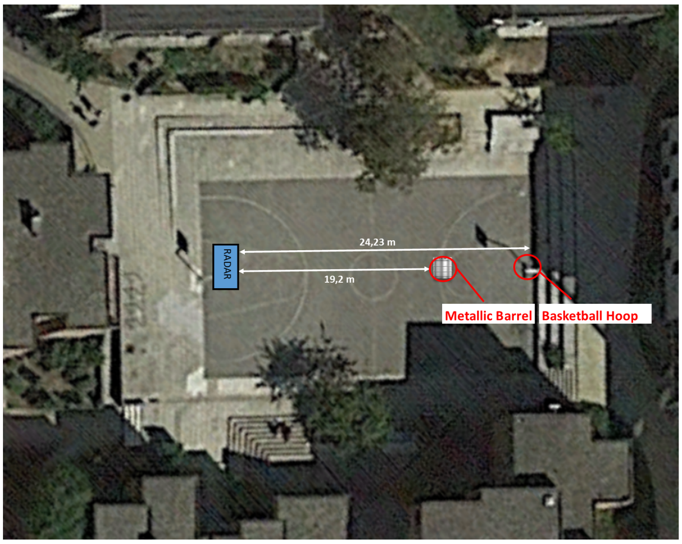

Figure 7.21: Satellite view of the setup of the measurement performed for testing the Matching Pursuit algorithm. A single target (here a barrel of beer) has been placed at a distance $L_{baril} = 19.2[m]$ in front of the radar. The tilt angle of the radar was 0° and its height 90 $[cm]$.

Parameter	**Value**
Radar bandwidth	$500\,[\text{MHz}]$
Rail length	$L_{\text{rail}} = 50\,[cm]$
Fraunhoher distance	$L_{\text{target}} \gg 20\,[m]$
Radar step distance	$\Delta d = 1\,[cm]$
Number of azimuth samples	$N = 50$
Number of range samples	$M = 256$
Range resolution	$\Delta R = 30\,[cm]$
Angular resolution	$\Delta\theta = \arcsin(\Delta\alpha) = 0.71°$
Maximal range	$R_{max} = 76.8\,[m]$

Table 7.8: Overview of the parameters used for the measurement of the 1-barrel measurement.

Post-processing steps For the Matching Pursuit algorithm :

1. Mean over the 256 chirps send by the radar for each position.
2. Calibration, following procedure exposed in section 7.1.1.
3. Matching Pursuit with a threshold $\rho = 0.1, 0.05, 0$ and with of 200,500 and 5000 maximum of iteration.
4. Cartesian coordinate plot using *imshow*.
5. When testing several threshold values the number of iterations is fixed at his maximum $(M \cdot N)$ and when testing several number of iterations, the threshold is fixed at 0.
6. Noise has been added to the signal for the last measurements. The noise is Gaussian and centred with a standard deviation $\sigma = 500$.

For the Fourier Transform algorithm :

1. Mean over the 256 chirps send by the radar for each position.
2. Background subtraction, following procedure exposed in section 7.1.1 with a *blank* measurement of the environment performed in the conditions exposed in Table 7.1.4 and Figure 7.13 without targets.
3. 2D-FFT using a padding coefficient of 1 (no zero padding) for both range and azimuth directions.
4. Polar coordinates plot, in $\log_{10}$ scale, using the function *pcolor* from Python to display a polar view of the image data.

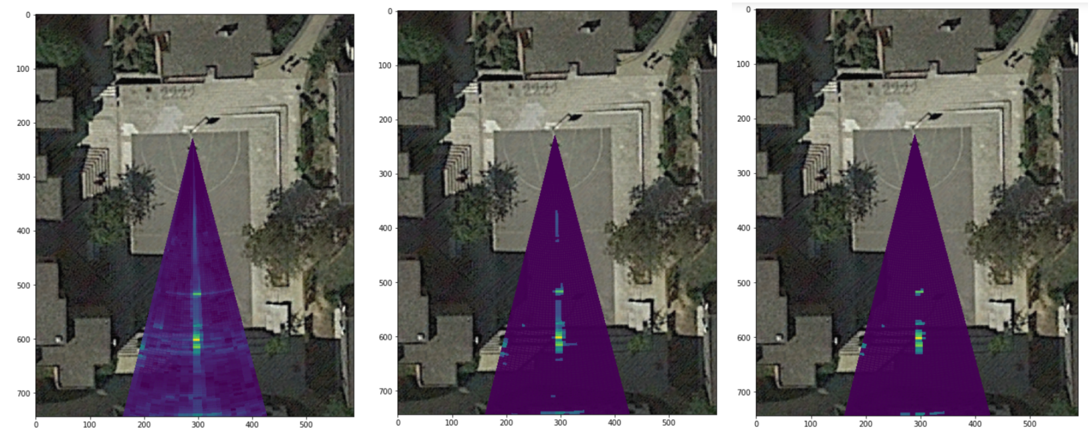

Figure 7.22: Result of the Matching Pursuit algorithm for the set-up presented in Figure 7.21 and Table 7.2 for various thresholds. From up to down : Matching Pursuit algorithm for $\rho = 0, 0.05$ and 0.1 with the maximum number of iterations being $M \cdot N$.

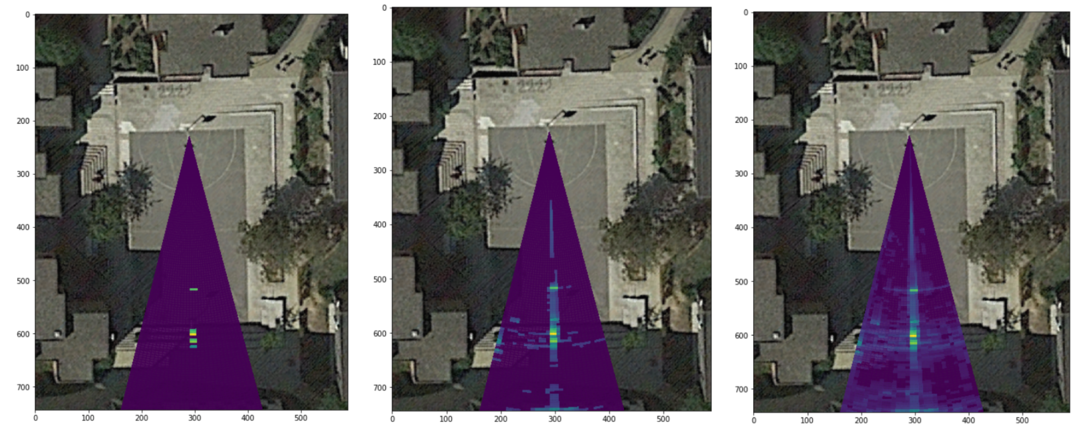

Figure 7.23: Result of the Matching Pursuit algorithm for the set-up realised in Figure 7.21 and Table 7.2 for various number of *max iteration*. From left to right : Matching Pursuit algorithm for a maximum iteration of 20,500 and 5000 with the threshold being $\rho = 0$.

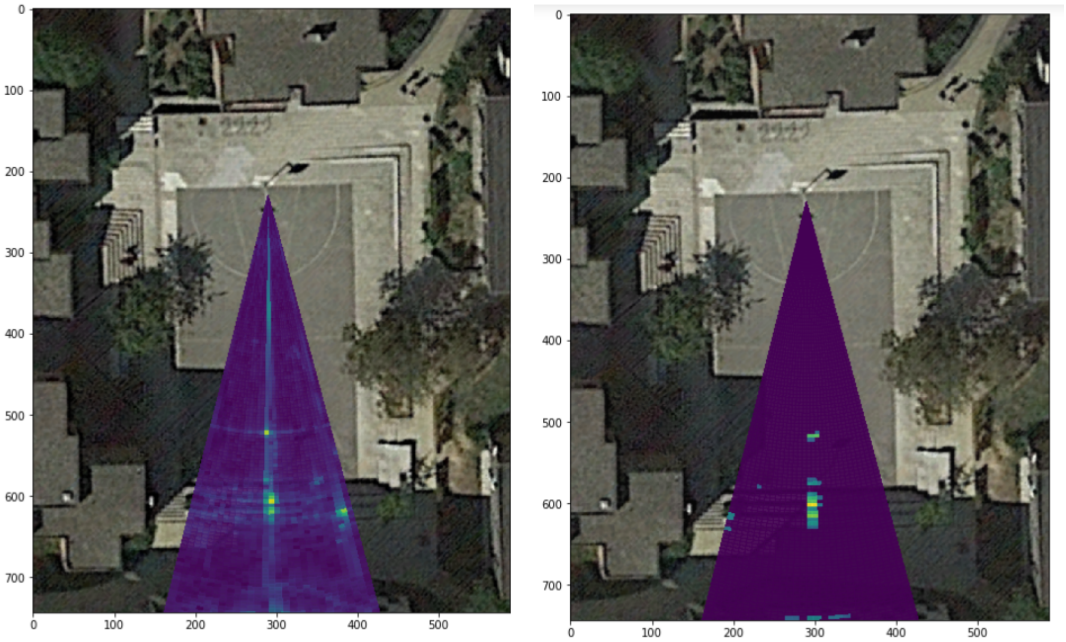

Figure 7.24: On the left, image recovered from the Fourier Transform algorithm and on the right, image recovered from the Matched pursuit algorithm ($\rho = 0.1$).

Discussion First the results of the measurement without noise are shown in Figures 7.22, 7.23 and 7.24. We see on Figure 7.22 that when the threshold is above 0.1, only a small number of points are displayed corresponding to the main targets. The Matching Pursuit algorithm recovers the targets without the ripples that were occurring in the Fourier Transform algorithm. That is, the image is generated from a dictionary of deltas that do not induce ripple. When the number of reflected waves (linked to the number of targets) becomes larger, the recovered image starts to decrease in visibility if the threshold is not large enough. This shows that the Matching Pursuit fits better for signal with a small number of targets. The main drawback of this algorithm is the size of the dictionary. It is very large and we run rapidly out of memory when trying to use more samples M and N. To avoid this limitation we should use dictionaries with less elements but this means that the resolution of the image could be decreased. Finally, when we add noise to the measurement, we see that both algorithm success to recover the main targets but the Matching Pursuit gives a cleaner image. This is due to the fact that the coefficient corresponding to the noisy part of the signal is lower than the threshold. It can be interesting to use the Matched Pursuit algorithm when we deal with measurement with low Signal to Noise Ratio or parasitic targets.

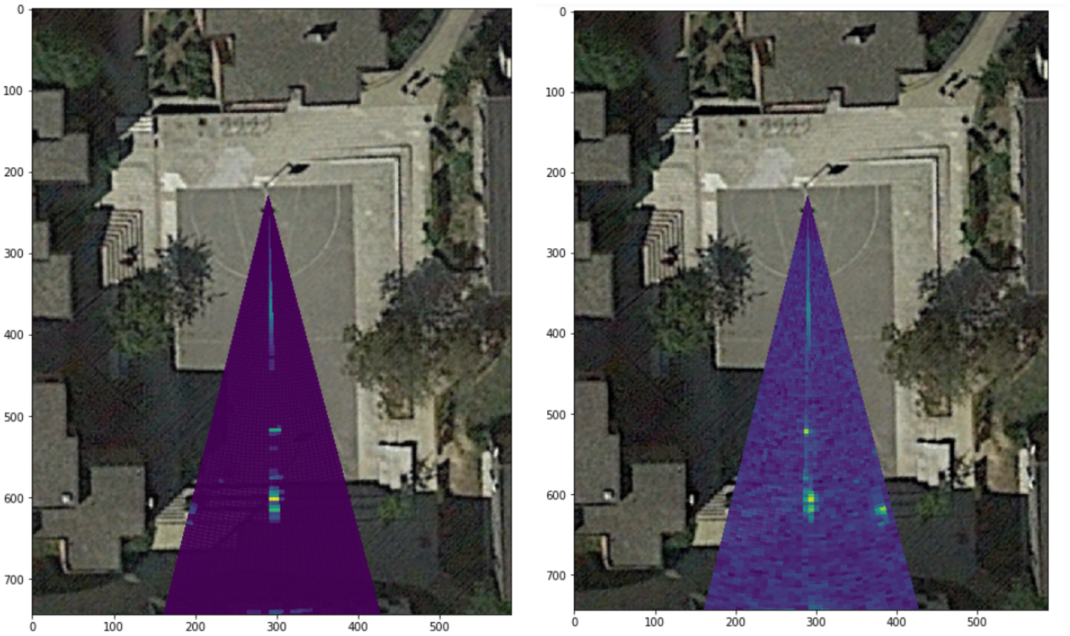

Figure 7.25: Result for the set-up realised in Figure 7.21 and Table 7.2 with noisy measurement of Gaussian distribution : $N(0, \sigma)$ with $\sigma = 500$ for the Matching Pursuit algorithm (left) and the Fourier Transform algorithm (right).

Chapter 8

Conclusion

During this master thesis, we have developed, characterised and validated a mathematical model in order to perform Synthetic Aperture Radar (SAR) at small scale. This model allowed us to recover pictures of targets and specific environments at a range distance from $10\,[m]$ to $70\,[m]$ with a radar providing a maximal bandwidth of $500\,[\text{MHz}]$.
First of all, we started from a general geometric description of SAR imaging problems and the transmitted Frequency Modulated Continous Wave (FMCW) expression to achieve a complete description of the received signal. We have considered two main spatial and temporal dimensions : the range direction that is associated with the *fast* temporal domain of the signal and the azimuth direction that corresponds to the *slow* temporal domain of the radar displacement. Only three hypotheses have been applied : the Far Field assumption, a first order Taylor expansion for the range distance between the radar and the target and, the radar speed that is much slower than the light speed.
We have discretised our domain in both spatial and temporal dimensions and simplified the complete model to remove higher order and constant phase terms. The final expression of the received signal has been expressed in polar coordinates and is a product of two exponential functions of the form

$$S_r^{BB}[m,n] \overset{\psi}{\simeq} \underbrace{\exp\left[4\pi j \frac{B}{cM} R_x m\right]}_{\text{Fast time dependent}} \cdot \underbrace{\exp\left[4\pi j \frac{f_0}{c} \sin(\theta)(n\Delta d)\right]}_{\text{Slow time dependent}}, \tag{8.1}$$

where m and n correspond to the *fast* and *slow* temporal discretizations and (R,θ) are the polar coordinates of the recovered SAR picture. Simulations have been performed in order to validate this simplified model.
Then, we have detailed both post-processing algorithms that we have used in our experiments : the *Fourier Transform* algorithm and the *Matching Pursuit*

algorithm. They have been mathematically described and simulated in order to identify their pros and cons and to compare them. We found that the former presents ripples due to the finite duration of a pulse while the latter induces a large computational cost.

Based on the simplified version of the model that we have developed, we have established the main equations necessary to perform small scale SAR measurements. More precisely, we have derived azimuth and range resolutions corresponding to our application and linked them to the available technology.

We have performed several measurements in specific environments designed to test the performances and limits of our model. We have described a calibration method to enhance data readability and prove its utility with a measurement of the *Maxwell antenna*. This result also allowed us to discuss the imperfections of the Fourier Transform algorithm such as the ripple due to the cardinal sine functions induced by the finite pulse duration.

After that, we were interested in the interaction between close metallic targets. We first analysed a measurement of the *Saint Barbe building entrance* that presented *ghost* targets due to the interactions. Then we predicted correctly the position of those *ghost* targets in a basic environment composed of two metallic barrels that we progressively brought closer to each other. This allowed to validate the applicability of our model.

We have then worked with metallic conic *targets* that we have disposed at different range distances from the radar in order to quantify the impact of the Fraunhofer assumption while increasing the rail length. By analysing results, we found a *critical point* from which the angular resolution stopped increasing and the targets started to spread in angular direction. Furthermore, we could experimentally rewrite the Fraunhofer condition as

$$L_{\text{target}} \geq \frac{L_{\text{rail}}^2}{\lambda} \qquad \text{instead of} \qquad L_{\text{target}} \gg \frac{L_{\text{rail}}^2}{\lambda}. \tag{8.2}$$

Building a setup with ten metallic barrels, we have analysed the effect of an error on the measurement of the radar step distance Δd, without inducing an error on the rail length. We observed that our model was robust to such variations. We also observed the impact of a Hamming window and a high pass filter on the quality of the recovered image, working with the same setup. We observed that both post-processing steps offer an efficient compensation to imperfections due to the Fraunhofer assumption and the Fourier transform.

Finally, we have compared results obtained with the Fourier Transform algorithm and the Matching Pursuit algorithm. This allowed us to highlight the imperfections of the former. In fact, the ripple due to the Fourier Transform is not present in results obtained with the Matching Pursuit algorithm. However, the latter is very heavy to process for large sets of data and is constrained to specific situations.

To bring the model developed in this master thesis further, it could be interesting to quantify the effects that we have observed with the presented measurements. We have proven the validity of the model and provided a first approximation of its performances, but it requires more experiments to associate the results with figures for its accuracy, its sensitivity to the target distance variations (Fraunhofer assumption), the impact of post-processing steps or the differences between the Fourier Transform algorithm and the Matching Pursuit algorithm.

Furthermore, the azimuth resolution of the model could be enhanced by working with a motorised rail and thus using the Doppler effect. In fact, the manual rail we used constrained our post-processing methods. In addition to this, we worked with a radar limited to a 500 [MHz] bandwidth and we were thus forced to work with a maximal range resolution of 30 [cm]. To explore the model further, it could be worthwhile to increase the bandwidth with another radar. This could also offer the possibility to increase the sampling in the *fast* temporal dimension, as we were limited by the intrinsic processing of the available radar.

In conclusion, this master thesis offers a solid model and relevant associated experiments that should be further explored in order to provide a complete toolbox to perform SAR at small scale.

Bibliography

[1] M.Cheney and B. Borden, *Fundamentals of Radar Imaging*, December 10, 2018.

[2] S.-J. Wei, X.-L. Zhang, J. Shi, and G. Xiang, “Sparse Reconstruction for SAR Imaging Based on Compressed Sensing,” *Progress in Electromagnetics Research*, no. Vol. 109, pp. 63–81, 2010.

[3] Y. K. Chan and V. C. Koo, “An introduction to synthetic aperture radar (sar).”

[4] “The doppler shift,” https://imagine.gsfc.nasa.gov/features/yba/M31-velocity/spectrum/doppler-more.html, accessed: 2019-05-30.

[5] V. Issakov, *Microwave Circuits for 24 GHz Automotive Radar in Silicon-based Technologies*, 2010.

[6] Y. K. Chan and V. C. Koo, “An introduction to synthetic aperture radar (SAR),” *Progress In Electromagnetics Research B*, no. Vol.2, pp. 27–60, 2008.

[7] A. W. Doerry, “Performance Limits for Synthetic Aperture Radar - second edition,” 2006.

[8] I. U. of Bahawalpur, “Principles of Radars,” 2010.

[9] G. Borg, “Embedded Wireless, Lecture 10,” 2018.

[10] M. Harter, T. Mahler, T. Schipper, A. Ziroff, and T. Zwick, “2-D Antenna Array Geometries for MIMO Radar Imaging by Digital Beamforming,” *2013 European Radar Conference*, pp. 383–386, 2013.

[11] E. E. Online, “Radar Course,” "https://earth.esa.int/web/guest/missions/esa-operational-eo-missions/ers/instruments/sar/applications/radar-courses/content-3/-/asset_publisher/mQ9R7ZVkKg5P/content/radar-course-3-real-aperture-radar", 2000-2019.

[12] J. Curlander and R. McDonough, “Synthetic aperture radar : System and signal processing,” p. 14.

[13] M. Cohen, “Principle of pulse compression in sar system.”

[14] Y. K. Chan and V. C. Koo, “An introduction to synthetic aperture radar (sar).”

[15] P. Lathiya and M. V. Shah, *Digital Matched Filtering based On-board Radar Signal Processing*, 2012.

[16] M. Hughes, “Antenna basics: Radiation patterns, permittivity, directivity, and gain.”

[17] “Antenna patern,” https://its-wiki.no/images/2/2b/RadiationPattern.pdf, accessed: 2019-03-21.

[18] “Antenna array theory,” http://www.waves.utoronto.ca/prof/svhum/ece422/notes/15-arrays2.pdf, accessed: 2019-04-25.

[19] “Linear array theory,” http://www.ece.mcmaster.ca/faculty/nikolova/antennad-load/currentlectures/L13.Arrays1.pdf, accessed: 2019-03-8.

[20] S. Mezouari and A. R. Harvey, “Validity of fresnel and fraunhofer approximations in scalar diffraction.”

[21] O. K. and Ersoy, “Diffraction, fourier optics and imaging.”

[22] “The binomial expension theorem,” https://medium.com/i-math/the-binomial-theorem-explained-6464f41e5268, accessed: 2019-05-18.

[23] C. Sheppard and M. Hrynevych, “Diffraction by a circular aperture: a generalization of fresnel diffraction theory.”

[24] R. YangHaiying, L. LiPing, Z. TanXiangwu, and G. Kang, “Spotlight sar technology.”

[25] E. Varenius, “2d discrete fourier transform.”

[26] “The convolution theorem, wikipedia,” https://en.wikipedia.org/wiki/Convolution-theorem, accessed: 2019-05-28.

[27] “Hamming window,” https://ccrma.stanford.edu/~jos/sasp/Hamming-Window.html, accessed: 2019-05-28.

[28] L. Jacques and C. de Vleeschouwer, “Lelec2885 : Sparsity principles and applications, from orthonormal bases to redundant systems.”

[29] S. G. Mallat and Z. Zhang, “Matching pursuits with time-frequency dictionaries.”

[30] R. M. GmbH, “K-MD2 - Engineering sample,” "https://www.rfbeam.ch/product?id=21", 2018.

UNIVERSITÉ CATHOLIQUE DE LOUVAIN
École polytechnique de Louvain
Rue Archimède, 1 bte L6.11.01, 1348 Louvain-la-Neuve, Belgique | **www.uclouvain.be/epl**